

Electron-phonon interactions and charge transport
in organic crystals and transition metal oxides
from first-principles calculations

Thesis by
Benjamin K. Chang

In Partial Fulfillment of the Requirements for the
Degree of
Doctor of Philosophy

The logo for the California Institute of Technology, featuring the word "Caltech" in a bold, orange, sans-serif font.

CALIFORNIA INSTITUTE OF TECHNOLOGY
Pasadena, California

2024
Defended February 29, 2024

© 2024

Benjamin K. Chang
ORCID: 0000-0003-1304-9324

All rights reserved

ACKNOWLEDGEMENTS

I would like to express my sincere gratitude towards my advisor, Prof. Marco Bernardi, for his immense support and guidance throughout my doctoral studies.

I would like to thank my thesis committee members, Prof. Austin Minnich, Prof. David Hsieh, and Prof. Joseph Falson, for their invaluable feedback and advice.

I thank my labmates, Dr. Nien-En Lee, Dr. Jin-Jian Zhou, Dr. Hsiao-Yi Chen, Dr. I-Te Lu, and Dr. Ivan Maliyov, and my collaborators, Dr. Iurii Timrov and Dr. Nicola Marzari, for the insightful scientific discussions and technical supports. I also thank everyone in the Bernardi group who have overlapped with me, including Dr. Vatsal Jhalani, Dr. Raffaello Bianco, Xiao Tong, Dr. Shiyuan Gao, Dhruv Desai, Dr. Sergio Pineda Flores, Khoa Le, Yao Luo, Kelly Yao, David Abramovitch, Shaelyn Iyer, and others.

I want to thank my dearest friends, Dr. Shao-Min Hung, Chien-Hui, Dr. Yu-Hung Lai, Dr. Yue Yang, Dr. Shih-Hao Tseng, Dr. Tzu-Ling Chen, Chang-Yi, Po-Chih, Man-Chun, Wendy, and many others for the fun companionship during my Ph.D. life in Pasadena, especially during the uncertain times of the global COVID-19 pandemic.

Lastly, I want to thank my family, especially my mother, Stephanie, my brother, Will, and my beloved wife, Yu-Ting. I would not have accomplished what I have achieved without your unconditional love and support.

ABSTRACT

Electron-phonon (*e-ph*) interactions play a critical role in determining material properties, such as charge and heat transport, optical response, and superconductivity. Recent advances in first-principles calculations based on density functional theory (DFT) enable quantitatively predictive studies of *e-ph* interactions and charge transport in a wide range of simple semiconductors and metals. However, certain technologically important materials, such as organic crystals and transition metal oxides (TMOs), remain less explored. Organic molecular crystals, known for their versatile electronic and mechanical properties, typically require high charge carrier mobility for practical applications. Yet accurately predicting the mobility and engineering approaches to improve it are challenging in organic crystals, because of their complex crystal structures with large unit cells and various charge transport regimes induced by *e-ph* interactions. Similarly, TMOs, both conventional and strongly correlated, are materials with broad applications and unique physics. A notable example are copper oxides (cuprate) superconductors, which are central to the study of high-temperature superconductivity and other exotic physical phenomena. Extensive experimental studies, particularly using photoemission techniques, have been employed to indirectly probe the *e-ph* interactions in TMOs. Nevertheless, many results are not fully understood, and calculations of *e-ph* coupling in TMOs are still scarce. This is mainly due to the strong correlation induced by *d*- and *f*-electrons posing a significant challenge to modeling.

This thesis aims to develop state-of-the-art first-principles calculations to accurately describe *e-ph* interactions and the associated physical properties in organic crystals and TMOs. We focus on three research topics. First, we investigate the high-mobility bandlike transport regime in organic crystals. Using the formalism of the Boltzmann transport equation with electronic collisions computed from first principles, we study the mobility and its temperature dependence in benzene, anthracene, tetracene, pentacene, and biphenyl. Our results are in excellent agreement with experiments in all cases, and our pentacene calculation (72 atoms per unit cell) sets the record for the largest first-principles *e-ph* calculation to date. We find that the mobility is mainly regulated by *e-ph* scattering from low-frequency intermolecular phonons. Our analysis evidences the effectiveness of strain-based engineering to improve the mobility of organic crystals. Second, we propose a computational approach to study the intermediate polaronic transport regime in organic crystals. This

method combines a finite-temperature cumulant-expansion approach for calculating electron spectral functions with the Kubo formula to compute the electronic conductivity and mobility. We show calculations of electron mobility in a naphthalene crystal in excellent agreement with experiments, and find that polaron effects, encoded in the satellites of the spectral functions, are induced by strong e -ph coupling of intramolecular hydrogen-atom vibrations. In the third and final topic, we study quantitatively the e -ph interactions in cuprate superconducting materials. Using the framework of Hubbard-corrected DFT, we focus on the prototypical parent (undoped) cuprate compound La_2CuO_4 , which becomes superconducting upon doping. We show the first quantitative evidence of strong Fröhlich-type e -ph interactions between holes and oxygen atomic vibrations, as well as polaron effects in hole spectral functions. Our findings explain a range of observations in photoemission experiments on both undoped and doped cuprates, suggesting the strong e -ph coupling is an intrinsic feature of the parent compounds rather than being induced by doping. The computational workflow presented in this work can be easily extended to a broad class of strongly-correlated oxides and insulators more generally. In summary, this thesis pushes the boundaries of first-principles calculations of e -ph interactions and transport, paving the way for a microscopic understanding of materials with large and complex unit cells, strong electronic correlations, and strong e -ph interactions.

PUBLISHED CONTENT AND CONTRIBUTIONS

- [1] B. K. Chang and M. Bernardi, “Bandlike charge carrier mobility in organic crystals from first-principles calculations”, *submitted*.
B.K.C participated in the conception of the project, performed calculations, analyzed the data, and participated in the writing of the manuscript.
- [2] B. K. Chang, I. Timrov, J. Park, J.-J. Zhou, N. Marzari, and M. Bernardi, “First-principles electron-phonon interactions and polarons in the parent cuprate La_2CuO_4 ”, [arXiv:2401.11322 \(2024\)](https://arxiv.org/abs/2401.11322). Under review in *Phys. Rev. Lett.* DOI: 10.48550/arXiv.2401.11322.
B.K.C participated in the conception of the project, performed calculations, analyzed the data, and participated in the writing of the manuscript.
- [3] B. K. Chang, J.-J. Zhou, N.-E. Lee, and M. Bernardi, “Intermediate polaronic charge transport in organic crystals from a many-body first-principles approach”, *npj Comput. Mater.* **8**, 63 (2022). DOI: 10.1038/s41524-022-00742-6.
B.K.C participated in the conception of the project, performed calculations, analyzed the data, and participated in the writing of the manuscript.

TABLE OF CONTENTS

Acknowledgements	iii
Abstract	iv
Published Content and Contributions	vi
Table of Contents	vi
List of Illustrations	viii
List of Tables	ix
Chapter I: Introduction	1
1.1 Overview	1
1.2 Physical picture of electron-phonon interactions	4
1.3 First-principles calculations	6
1.4 Thesis outline	9
Chapter II: Bandlike Charge Carrier Mobility in Organic Crystals	15
2.1 Introduction	15
2.2 Methodology	17
2.3 Results	18
2.4 Conclusions	30
2.5 Supplementary materials	31
Chapter III: Intermediate Polaronic Charge Transport in Organic Crystals	41
3.1 Introduction	41
3.2 Results	43
3.3 Discussion	52
3.4 Methods	54
3.5 Supplementary material	56
Chapter IV: Electron-Phonon Interactions and Polarons in the Parent Cuprate La_2CuO_4	60
4.1 Introduction	60
4.2 Results	61
4.3 Discussion	68
4.4 Supplementary material	69
Chapter V: Summary and future directions	76

LIST OF ILLUSTRATIONS

<i>Number</i>	<i>Page</i>
1.1 Illustration of electron-phonon dynamics	4
2.1 Bandlike charge carrier mobility in organic crystals	19
2.2 Scattering rates and their impact on mobility	21
2.3 Low-frequency phonon modes	24
2.4 Electron-phonon coupling distribution function	27
2.5 Strain effects on mobility	29
2.6 Full phonon dispersion	32
2.7 Strained electronic structure and phonon dispersion	33
2.8 Anthracene mobility and scattering rate under tensile strain	34
2.9 Distribution functions of electron-phonon coupling and scattering phase space	35
3.1 Band and crystal structures of naphthalene	45
3.2 In-plane electron mobility	46
3.3 Spectral function and electron-phonon coupling	47
3.4 Full width at half maximum of the quasiparticle peak	50
3.5 Hole carrier mobilities	51
3.6 Electron mobility in the plane-normal direction	53
3.7 Comparison of the electron-phonon coupling strength	56
4.1 Band structure of La_2CuO_4	62
4.2 Phonon and electron-phonon coupling	63
4.3 Electron spectral function	65
4.4 Electron-phonon coupling distribution function	67
4.5 Band gap and Cu magnetic moment as a function of U	70
4.6 Phonon from DFPT+ U	71

LIST OF TABLES

<i>Number</i>		<i>Page</i>
2.1	Computational details	31

Chapter 1

INTRODUCTION

1.1 Overview

Electron-phonon (*e-ph*) interactions play a critical role in determining the properties of conventional metals, semiconductors, and insulators, as well as novel quantum materials. First, *e-ph* interactions act as a major limiting factor for the efficiency of many solid-state applications. For example, phonons, the quanta of atomic vibrations, impede the movement of charge carriers (electrons and holes) in traditional semiconductors and metals, resulting in restricted electrical conductivity [1]. They also cause electron spins to undergo spin-flip scattering and decoherence, posing a challenge to implement spintronic devices and spin-based quantum technologies [2]. In addition, *e-ph* interactions govern key properties linked to material performance, for example by assisting optical absorption in indirect-gap semiconductors widely employed in solar cells [3], as well as reducing heat transport [4] to improve thermoelectric performance. Finally, conventional superconductivity is due to *e-ph* interactions, where electrons are attracted by forces mediated by phonons to form Cooper pairs and condense into a superfluid that is able to carry electric current without dissipation [5]. Unconventional (or high-temperature) superconductivity, on the other hand, is believed to arise from the interplay between *e-ph* interactions and electron correlations [6], although the microscopic details of these interactions remain a major unsolved problem in condensed matter physics. Therefore, understanding *e-ph* coupling in materials is crucial for tasks ranging from optimizing modern electronics to designing renewable energy, low-dissipation wires, and quantum technologies.

Organic crystals are a class of technologically important materials with properties heavily influenced by *e-ph* interactions. These crystals are formed by stacked molecules, which makes them mechanically flexible and environmentally benign compared to their inorganic counterparts. Their electronic properties range from insulating to semiconducting, with versatility such as hosting ferroelectricity [7], magnetism [8] and superconductivity [9]. Organic semiconductors find application in stretchable electronics [10], bioelectronics [11], batteries [12], optoelectronics [13], solar cells [14], spintronics [15], and more. However, the limited

efficiency of these devices has been a bottleneck for real-world applications. The charge carrier mobility, a key figure of merit for semiconductors, is commonly below $10 \text{ cm}^2\text{V}^{-1}\text{s}^{-1}$ [16] in organic crystals. This is significantly lower than the $\sim 10^3 \text{ cm}^2\text{V}^{-1}\text{s}^{-1}$ in traditional semiconductors like silicon and germanium. The low mobility is due to electron motions being hindered by the interactions with intra- and inter-molecular atomic vibrations (phonons). Furthermore, such complex e -ph interactions lead to a wide range of charge transport regimes [17]. Even in the same organic crystal, electron and hole carriers in different crystallographic directions may exhibit mobilities differing by orders of magnitude and with significantly distinct temperature dependence. This makes modeling the mobility notoriously difficult, with simulated results often differ from experimental values by orders of magnitudes. Moreover, the inherent structural complexity and low symmetry of organic crystals result in unit cells comprising a few tens to a few hundred atoms, making simulations prohibitive. These challenges call for accurate predictions of charge carrier mobility as a central effort for organic materials research.

Transition metal oxides (TMOs) are another class of materials critical to condensed matter physics and devices for various applications. The TMOs host a plethora of exotic physical phenomena, including multiferroicity [18], colossal magnetoresistance [19], and unconventional states of matter such as strange metal [20] and charge density wave [21]. Among the TMO family, copper oxides (cuprates) are the most well-known for holding the record for the highest superconducting critical temperature at ambient pressure to date (135 K) [22]. Cuprates exhibit a complex phase diagram in the charge doping versus temperature design space [23]. This behavior is believed to result from the intricate interplay between strong electron correlations (electron-electron interactions) imparted by the localized d - and f -electronic orbitals, and e -ph interactions between the localized charges and the lattice with polar covalent or ionic bonds [24]. Over the past few decades, angle-resolved photoemission spectroscopy (ARPES) [25] experiments have been extensively conducted to study the electronic structures in cuprates. The measured electron spectral functions provided indirect evidence of strong e -ph interactions [26]. However, these results have yet to be fully understood theoretically, mainly due to the correlation effects posing a challenge to modeling even the ground state. Therefore, developing accurate calculations of e -ph interactions and electron spectral functions in strongly-correlated TMOs is essential for advancing our grasp of high-temperature superconductivity and fundamental understanding of materials physics.

Conventional analytical approaches to treat e -ph interactions parametrize various mechanisms for e -ph interactions, including the deformation potential, piezoelectric, and polar couplings [27]. System-targeted models have also been developed to describe specific classes of materials. For example, the Peierls and Holstein models are used to describe the intermolecular and intramolecular phonons in organic crystals, respectively [28, 29]. When combined with appropriate transport formalisms, these models can qualitatively reproduce experimental observations. However, they often incorporate only a few phonon modes, treat phonons on unequal footings, or require fitting parameters to experimental data. Such restrictions introduce ambiguity into calculations and limit the predictive power.

First-principles methods have demonstrated increasing efficiency and accuracy in predicting material properties [30]. By leveraging density functional theory (DFT) [31, 32] and density functional perturbation theory (DFPT) [33], these methods calculate electron and phonon data self-consistently, taking only crystal structures and atomic positions as input, and without the use of any empirical parameter. The e -ph matrix elements are constructed accordingly, where the coupling of all electronic states with all phonons is taken into account on equal footing [34]. In the last decade, transport calculations using *ab initio* e -ph matrix elements have achieved tremendous success in simulating the charge carrier mobility in semiconductors, as well as revealing microscopic details of e -ph dynamics at the phonon mode-resolved level [35–42]. However, the majority of these first-principles e -ph calculations have focused on simple inorganic compounds, particularly elemental or III-V semiconductors [35–37, 40, 41]. Calculations on organic crystals and TMOs are still scarce, primarily due to the computational and theoretical complexity.

This thesis aims to develop and apply first-principles e -ph calculations to study organic crystals and TMOs. We focus on computing the e -ph coupling, charge carrier mobility, and electron spectral function in these materials, carefully comparing computed results to experiments. We study both the bandlike and polaron charge transport mechanisms in organic crystals, and suggest new routes toward achieving higher mobility. Our calculations evidence the polaronic nature of undoped lanthanum cuprate, and draw a connection between the e -ph coupling in doped and undoped compounds. Through these studies, this thesis pushes the boundaries of first-principles calculations and also deepens our understanding of e -ph interactions in structurally and/or electronically complex crystals, thus advancing condensed matter physics, materials engineering, and electronic technology.

1.2 Physical picture of electron-phonon interactions

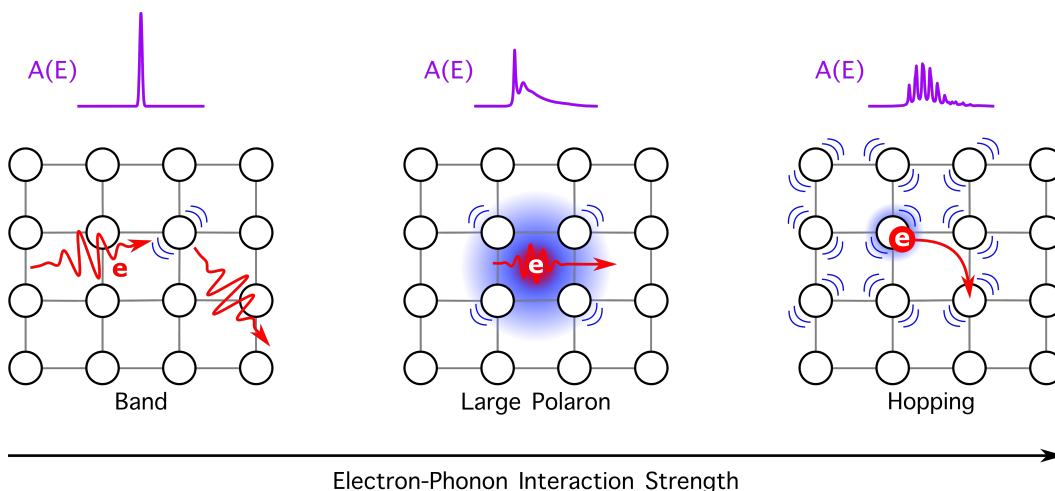


Figure 1.1: Charge transport regimes and their corresponding electron spectral functions [$A(E)$, purple] due to e -ph interactions. Red represents electrons and blue indicates phonon effects. The black circles represent lattice sites in a crystal.

Depending on the strength of the e -ph coupling, materials exhibit a variety of charge transport regimes [43], each dominated by a unique transport mechanism that needs to be described by a specific level of theory. These different regimes exhibit distinct temperature dependence of the mobility, which is a macroscopic quantity measuring how fast charges can move on average under an applied electric field. For the microscopic behavior of a charge carrier, the electron spectral function $A(E)$ is typically studied. As a distribution function over the energy E , the spectral function indicates how closely a charge carrier behaves like that in a non-interacting ideal electron gas. To illustrate how these quantities are influenced by e -ph interactions, we first consider an ideal electron gas with no interactions, and then gradually turn on e -ph interactions to observe how the system evolves [44].

In the absence of interactions, electrons form Bloch waves that extend periodically throughout crystal lattice, with their spectral functions being Dirac delta functions. Since no mechanism is present for electrons to lose energy, once an electronic state is excited by an external electric field, the state has an ideally long lifetime, resulting in an effectively infinite mobility in the collision picture. When e -ph interactions are weak, the band transport regime emerges (Figure 1.1), where carriers are still delocalized waves but their spectral functions acquire a finite width, deviating from the delta function and indicating the presence of quasiparticles (QPs) with a finite lifetime [44]. In contrast to the long-lived electronic states in the non-

interacting system, QPs have finite lifetimes (or relaxation times) due to phonon-induced scattering, which occasionally kicks a charge carrier out of the current state into another electronic state. The scattering rate is proportional to the QP peak width, and can be calculated from lowest-order perturbation theory using Fermi's golden rule [30]. This semi-classical e -ph scattering mechanism is described by the Boltzmann transport equation (BTE) [1], which describes charge transport in the band picture when interactions are weak and result in isolated collision events. This regime applies to many simple solid-state materials, such as elemental [45] and III-V semiconductors [46] and a wide range of metals like aluminum and copper [47]. The charge carrier mobility in the band transport regime is typically $> 10 \text{ cm}^2\text{V}^{-1}\text{s}^{-1}$ at room temperature, and exhibits a T^{-n} power-law decrease with respect to temperature. Identifying the exponent n in the power-law is important to characterize the mechanism governing charge transport in this regime.

As e -ph interactions get stronger, a charge carrier becomes surrounded by a cloud of phonons while traveling through the crystal, becoming "heavier" and more localized, forming a so-called large (or delocalized) polaron (Fig. 1.1) [48]. The corresponding electron spectral function exhibits significant weight transfer from the QP peak to the phonon-induced satellite peaks (or sidebands), which emerge on the shoulders of the spectral function. To capture such weight transfer, computational methods incorporating higher-order e -ph interactions are needed to calculate the spectral function, such as the cumulant expansion approach [49, 50] and diagrammatic Monte Carlo [51] among others [48]. Since the electronic state resides not only in the QP peak but also in the satellites, an accurate description of charge transport should take into account full spectral function, which can be accomplished for example using the Kubo formalism within linear response theory [27]. Large polarons are commonly found in halide perovskites [52] and oxides [53, 54]. Their mobility is typically $1\text{--}10 \text{ cm}^2\text{V}^{-1}\text{s}^{-1}$ near room temperature and also follows a power-law decrease with temperature, although usually with a weaker temperature dependence than that in the band transport regime.

In the presence of even stronger e -ph interactions, a charge carrier forms a small polaron trapped on and hopping between lattice sites (Fig. 1.1) [48]. Small polarons are commonly present in TMOs [55] and organic crystals [56], with their corresponding self-trapping lattice sites being atoms and molecules, respectively. In this regime, the QP peak in the electron spectral function becomes indistinguishable, and its weight is distributed over a series of phonon-induced excitation peaks [57]. The

small polaron states can be qualitatively understood using the Holstein model [58], and their hopping processes, which are thermally activated, can be described by Marcus theory [59]. The hopping mobility is typically $< 1 \text{ cm}^2\text{V}^{-1}\text{s}^{-1}$ and is constant or increases with temperature.

1.3 First-principles calculations

First-principles calculations based on DFT have been a workhorse for studies of the electronic structure in materials for several decades. The foundation of DFT lies in the Hohenberg-Kohn theorem, which states that the ground-state energy of an interacting many-electron system is a unique functional of its ground-state charge density [31]. Soon after this theorem's formulation, Kohn and Sham introduced an ansatz, proposing that the true ground-state charge density of the interacting system can be reproduced from a fictitious non-interacting electron system, or the Kohn-Sham (KS) system [32]. The theorem and ansatz together lead to a Schrödinger-like equation. By approximating the exchange-correlation energy term, the KS equation can be solved self-consistently, yielding the ground-state energies and single-particle wave functions, also known as the KS electron orbitals. In particular, when calculated with suitable approximations of the exchange-correlation functional, these orbital energies can be viewed as QP wave functions describing the addition or removal of electrons in solids and molecules. Nowadays, first-principles studies are increasingly focused on leveraging KS orbitals to investigate excited states and nonequilibrium phenomena, including optical response and charge transport. This thesis explores the use of first-principles calculations to study the band and large polaron transport regimes in materials.

Electron, phonon, and electron-phonon coupling

Throughout this thesis, we use the ground-state electron Bloch wave functions $|n\mathbf{k}\rangle$ and band energies $\varepsilon_{n\mathbf{k}}$ using DFT, where n and \mathbf{k} are the band index and crystal momentum, respectively. These calculations are carried out using the QUANTUM ESPRESSO code [60, 61]. When dynamical screening effects are considered, the GW approximation [62] as implemented in the YAMBO code [63] is employed to correct the DFT band structure. For Mott insulators, where strong correlation arises from the Coulomb repulsion between localized d or f orbitals, plain DFT is not suitable. In these cases, Hubbard-corrected DFT (DFT+ U) [64], in which an extra U term is added to the energy functional to capture on-site Coulomb repulsion, is employed to obtain the correlated electron ground state. The U parameters for the

Hubbard atoms are determined *ab initio* by iteratively relaxing the crystal structure with DFT+ U and calculating U from linear response [65, 66], until self-consistency is achieved between the crystal structure and U parameters. As such, our calculations remain free of adjustable parameters.

We compute lattice dynamics using density functional perturbation theory (DFPT) [33], a linear response extension of DFT. We obtain phonon energies $\omega_{\nu\mathbf{q}}$, eigenvectors $\mathbf{e}_{\nu\mathbf{q}}^{\kappa\alpha}$, and perturbation potentials $\partial_{\mathbf{q}\kappa\alpha}V$, where ν and \mathbf{q} are the phonon mode index and momentum, while α and κ label the Cartesian directions and the atoms in a unit cell, respectively. For Mott insulators, we employ Hubbard-corrected DFPT (DFPT+ U) [67] calculations, based on the corresponding DFT+ U calculations, to compute lattice dynamics. In these cases, the change in the Hubbard-like potential due to lattice perturbation is included in the e -ph perturbation potential. For systems with anharmonic effects that result in unphysical soft phonon modes in DFPT(+ U), we employ the stochastic self-consistent harmonic approximation (SSCHA) [68] to obtain an effective harmonic representation for the anharmonic phonons at finite temperature; this is achieved by constructing ensembles of random atomic configurations [68].

The e -ph matrix elements are obtained by combining the electron and phonon data, and are given by [30]

$$g_{mn\nu}(\mathbf{k}, \mathbf{q}) = \sqrt{\frac{\hbar}{2\omega_{\nu\mathbf{q}}}} \sum_{\kappa\alpha} \frac{\mathbf{e}_{\nu\mathbf{q}}^{\kappa\alpha}}{\sqrt{M_{\kappa}}} \langle m\mathbf{k} + \mathbf{q} | \partial_{\mathbf{q}\kappa\alpha}V | n\mathbf{k} \rangle, \quad (1.1)$$

where M_{κ} is the mass of atom κ . In practice, due to computational cost, DFT(+ U) and DFPT(+ U) calculations are performed using coarse momentum \mathbf{k} - and \mathbf{q} -grids. Consequently, the e -ph matrix elements are also formed on these coarse grids. However, to converge integrals and summations in transport calculations, one usually needs matrix elements on a finer grid that is 10^3 – 10^4 times denser. These correspond to coarse grids of $10 \times 10 \times 10$ and fine grids of $100 \times 100 \times 100$ in the Brillouin zone (BZ) for typical systems with a few atoms in the unit cells. Since this thesis is focused on complex systems with larger unit cells including more than ten atoms, our calculations require coarse and fine grids of orders $4 \times 4 \times 4$ and $50 \times 50 \times 50$, respectively. Therefore, we employ the Wannier interpolation technique, as implemented in the PERTURBO code [34], to interpolate e -ph matrix elements from coarse grids to arbitrarily fine grids. The maximally localized Wannier functions [69] necessary for this interpolation are obtained using the WANNIER90 code [70].

Electron-phonon dynamics and charge transport

In quantum field theory, the dynamics of an interacting many-body system is encoded in its self-energy. The lowest-order (Fan-Migdal) e -ph self-energy is given by [27]

$$\begin{aligned} \Sigma_{n\mathbf{k}}(E, T) &= \sum_{m\nu\mathbf{q}} |g_{m\nu}(\mathbf{k}, \mathbf{q})|^2 \\ &\times \left[\frac{N_{\nu\mathbf{q}} + f_{m\mathbf{k}+\mathbf{q}}}{E - \varepsilon_{m\mathbf{k}+\mathbf{q}} + \omega_{\nu\mathbf{q}} + i\eta} + \frac{N_{\nu\mathbf{q}} + 1 + f_{m\mathbf{k}+\mathbf{q}}}{E - \varepsilon_{m\mathbf{k}+\mathbf{q}} - \omega_{\nu\mathbf{q}} + i\eta} \right], \end{aligned} \quad (1.2)$$

where E is the electron energy, T is the temperature, and η is a real positive infinitesimal. $f_{n\mathbf{k}}$ and $N_{\nu\mathbf{q}}$ are the electron Fermi-Dirac and phonon Bose-Einstein occupations in thermal equilibrium, respectively, which account for the temperature dependence of the self-energy.

In the weakly-coupled band transport regime, the e -ph scattering mechanism dominates the transport dynamics. The e -ph scattering rate can be obtained using Fermi's golden rule, which corresponds to calculating the imaginary part of the self-energy on-shell, given by [30]

$$\begin{aligned} \Gamma_{n\mathbf{k}}(T) &= \frac{2}{\hbar} \text{Im} \Sigma_{n\mathbf{k}}(\varepsilon_{n\mathbf{k}}, T) \\ &= \frac{2\pi}{\hbar} \sum_{m\nu\mathbf{q}} |g_{m\nu}(\mathbf{k}, \mathbf{q})|^2 \\ &\quad \times [(N_{\nu\mathbf{q}} + 1 - f_{m\mathbf{k}+\mathbf{q}}) \delta(\varepsilon_{n\mathbf{k}} - \varepsilon_{n\mathbf{k}+\mathbf{q}} - \omega_{\nu\mathbf{q}}) \\ &\quad + (N_{\nu\mathbf{q}} + f_{m\mathbf{k}+\mathbf{q}}) \delta(\varepsilon_{n\mathbf{k}} - \varepsilon_{n\mathbf{k}+\mathbf{q}} + \omega_{\nu\mathbf{q}})]. \end{aligned} \quad (1.3)$$

The charge carrier mobility is given by the BTE within the relaxation time approximation [71]:

$$\mu_{\alpha\beta}(T) = \frac{2e}{n_c V_{\text{uc}}} \int dE \left(-\frac{\partial f(E, T)}{\partial E} \right) \sum_{n\mathbf{k}} \tau_{n\mathbf{k}}(T) v_{n\mathbf{k}}^\alpha v_{n\mathbf{k}}^\beta \delta(E - \varepsilon_{n\mathbf{k}}), \quad (1.4)$$

where e is the electronic charge, f the Fermi-Dirac distribution, n_c the carrier concentration, and V_{uc} is the unit cell volume. $\tau_{n\mathbf{k}} = \Gamma_{n\mathbf{k}}^{-1}$ are the e -ph relaxation times, and $\mathbf{v}_{n\mathbf{k}} = \partial \varepsilon_{n\mathbf{k}} / \partial \mathbf{k}$ are the electron band velocities.

To address stronger e -ph interactions, full electron spectral functions including higher-order interactions need to be computed to capture phonon side bands and polaron effects. We employ an finite-temperature cumulant approach, in which the retarded electron Green's function in the time domain is written using the exponential ansatz [39, 72, 73]

$$G_{n\mathbf{k}}^{\text{R}}(t, T) = G_{n\mathbf{k}}^{\text{R},0}(t) e^{C_{n\mathbf{k}}(t, T)}, \quad (1.5)$$

where $G_{n\mathbf{k}}^{\text{R},0}$ is the non-interacting Green's function, and $C_{n\mathbf{k}}(t, T)$ is the cumulant function, defined as

$$C_{n\mathbf{k}}(t, T) = \int dE \frac{|\text{Im}\Sigma_{n\mathbf{k}}(E + \varepsilon_{n\mathbf{k}}, T)|}{\pi E^2} (e^{-iEt} + iEt - 1). \quad (1.6)$$

The exponential ansatz, although computed using the lowest-order self-energy, effectively include contributions from higher-order terms. The electron spectral function is obtained via the usual relationship from the retarded Green's function,

$$A_{n\mathbf{k}}(E, T) = -\text{Im}G_{n\mathbf{k}}^{\text{R}}(E, T)/\pi. \quad (1.7)$$

The charge carrier mobility, in the absence of vertex corrections, can be computed with the electron spectral functions using the linear-response Kubo formula [27, 39, 74]:

$$\mu_{\alpha\beta}(T) = \frac{\pi\hbar e}{n_c V_{\text{uc}}} \int dE \left(-\frac{\partial f(E, T)}{\partial E} \right) \sum_{n\mathbf{k}} v_{n\mathbf{k}}^{\alpha} v_{n\mathbf{k}}^{\beta} |A_{n\mathbf{k}}(E, T)|^2. \quad (1.8)$$

This cumulant-Kubo (CK) approach thus can describe the charge transport in the presence of large polarons due to stronger e -ph interactions.

1.4 Thesis outline

This thesis consists of three separate studies, each leveraging the first-principles approaches described above to investigate e -ph interactions and charge transport dynamics in organic crystals and TMOs.

Chapter 2 presents a comprehensive investigation of bandlike charge transport in organic crystals, which additionally reveals new strategies to achieve higher mobility. We conduct accurate BTE calculations in the bandlike transport regime in several crystals including benzene, anthracene, tetracene, pentacene, and biphenyl. The e -ph calculations on pentacene (72 atoms per unit cell) are the largest first-principles e -ph calculations reported to date, exceeding the previous record on methylammonium lead iodide (48 atoms per unit cell) [75]. Our computed mobilities show a power-law temperature dependence, achieving excellent agreement with experiments between 100–400 K in all five materials. We find that scattering from low-frequency (LF) phonon modes below 150 cm^{-1} predominantly limits these mobilities, even though the LF modes are not modes with strongest coupling, and the phonon spectra includes many modes and extends to $3,100 \text{ cm}^{-1}$. These LF modes primarily consist of intermolecular vibrations, with increasing long-range intramolecular character in crystals made up by larger molecules. Furthermore, we

find that the LF-mode scattering rates are distinctively responsive to strain, suggesting that strain engineering can effectively modulate bandlike charge transport and enhance the mobility.

In Chapter 3, we show that the so-called intermediate charge transport regime in organic crystals is characterized by the presence of large polarons. Traditionally, charge transport in organic crystals has long been categorized into two limiting regimes: band transport and charge hopping. While both limits are described by well established models, their intermediate regime remains less understood. A notable example of the intermediate regime is the electron mobility in naphthalene, which exhibits a bandlike power-law temperature dependence, while BTE fails to reproduce the correct dependence. Here we demonstrate that the CK approach can accurately predict carrier mobility in this intermediate regime. Our CK predictions of the electron mobility in naphthalene are within a factor of 1.5–2 of experiments between 100–300 K. Our analysis reveals the formation of a broad satellite peak in the electron spectral function induced by strongly-coupled intramolecular phonons, indicating large polaron effects and explaining the breakdown of BTE.

In Chapter 4, we examine the strong e -ph interactions and polaron effects in the parent (undoped) phase of cuprates, which are supported by ample experimental observations but are not yet fully understood. Our study focuses on the prototypical parent compound La_2CuO_4 (LCO), leveraging DFT+ U with the Hubbard-parameter U computed directly rather than fitted to experiments. For the first time in a parent cuprate, we predict a ground state with a band gap and Cu magnetic moment in near-exact agreement with experiments. Our computed e -ph coupling reveals two classes of longitudinal optical (LO) phonons coupling strongly with hole states in LCO, consistent in energy with experimental signatures in doped compounds. Additionally, we calculate the hole spectral functions using the cumulant approach. The results exhibit a significant broadening due to large-polaron effects and reproduce features observed ARPES. Our analysis finds a substantial portion of the strong coupling associated with apical O and Cu-O bond-bending vibrations, which are not well captured in the conventional models for cuprates. These results show that the universal strong e -ph coupling found experimentally in LCO is an intrinsic feature of the parent compound, and elucidates its microscopic origin.

Finally, Chapter 5 summarizes the main achievements of this thesis and discusses potential future research directions.

References

- [1] J. Ziman, *Electrons and phonons: The theory of transport phenomena in solids* (Oxford University Press, Oxford, 2001).
- [2] J. Park, J.-J. Zhou, Y. Luo, and M. Bernardi, *Phys. Rev. Lett.* **129**, 197201 (2022).
- [3] J. Noffsinger, E. Kioupakis, C. G. Van De Walle, S. G. Louie, and M. L. Cohen, *Phys. Rev. Lett.* **108**, 167402 (2012).
- [4] J. Zhou, H. D. Shin, K. Chen, B. Song, R. A. Duncan, Q. Xu, A. A. Maznev, K. A. Nelson, and G. Chen, *Nat. Commun.* **11**, 6040 (2020).
- [5] J. Bardeen, L. N. Cooper, and J. R. Schrieffer, *Phys. Rev.* **108**, 1175–1204 (1957).
- [6] M. L. Kulić, *Phys. Rep.* **338**, 1–264 (2000).
- [7] S. Horiuchi and Y. Tokura, *Nat. Mater.* **7**, 357–366 (2008).
- [8] J. S. Miller, *Mater. Today* **17**, 224–235 (2014).
- [9] D. Jérôme, *J. Supercond. Nov. Magn.* **25**, 633–655 (2012).
- [10] T. Q. Trung and N.-E. Lee, *Adv. Mater.* **29**, 1603167 (2017).
- [11] D. Ohayon and S. Inal, *Adv. Mater.* 2001439 (2020).
- [12] S. Muench, A. Wild, C. Friebe, B. Häupler, T. Janoschka, and U. S. Schubert, *Chem. Rev.* **116**, 9438–9484 (2016).
- [13] O. Ostroverkhova, *Chem. Rev.* **116**, 13279–13412 (2016).
- [14] O. Inganäs, *Adv. Mater.* **30**, 1800388 (2018).
- [15] V. A. Dediu, L. E. Hueso, I. Bergenti, and C. Taliani, *Nat. Mater.* **8**, 707–716 (2009).
- [16] S. Fratini, M. Nikolka, A. Salleo, G. Schweicher, and H. Sirringhaus, *Nat. Mater.* **19**, 491–502 (2020).
- [17] H. Oberhofer, K. Reuter, and J. Blumberger, *Chem. Rev.* **117**, 10319–10357 (2017).
- [18] C. Lu, W. Hu, Y. Tian, and T. Wu, *Appl. Phys. Rev.* **2**, 021304 (2015).
- [19] A. P. Ramirez, *J. Phys. Condens. Matter* **9**, 8171 (1997).
- [20] R. L. Greene, P. R. Mandal, N. R. Poniatowski, and T. Sarkar, *Annu. Rev. Condens. Matter Phys.* **11**, 213–229 (2020).
- [21] H. Miao, G. Fabbris, R. J. Koch, D. G. Mazzone, C. S. Nelson, R. Acevedo-Esteves, G. D. Gu, Y. Li, T. Yilimaz, K. Kaznatcheev, E. Vescovo, M. Oda, T. Kurosawa, N. Momono, T. Assefa, I. K. Robinson, E. S. Bozin, J. M. Tranquada, P. D. Johnson, and M. P. M. Dean, *npj Quantum Mater.* **6**, 31 (2021).

- [22] P. A. Lee, *Rep. Prog. Phys.* **71**, 012501 (2008).
- [23] B. Keimer, S. A. Kivelson, M. R. Norman, S. Uchida, and J. Zaanen, *Nature* **518**, 179–186 (2015).
- [24] O. Gunnarsson and O. Rösch, *J. Phys. Condens. Matter* **20**, 043201 (2008).
- [25] J. A. Sobota, Y. He, and Z.-X. Shen, *Rev. Mod. Phys.* **93**, 025006 (2021).
- [26] A. Lanzara, P. V. Bogdanov, X. J. Zhou, S. A. Kellar, D. L. Feng, E. D. Lu, T. Yoshida, H. Eisaki, A. Fujimori, K. Kishio, J.-I. Shimoyama, T. Noda, S. Uchida, Z. Hussain, and Z.-X. Shen, *Nature* **412**, 510–514 (2001).
- [27] G. D. Mahan, *Many-Particle Physics* (Springer US, New York, 2000).
- [28] J. H. Fetherolf, D. Golež, and T. C. Berkelbach, *Phys. Rev. X* **10**, 021062 (2020).
- [29] W. Li, J. Ren, and Z. Shuai, *Nat. Commun.* **12**, 4260 (2021).
- [30] M. Bernardi, *Eur. Phys. J. B* **89**, 239 (2016).
- [31] P. Hohenberg and W. Kohn, *Phys. Rev.* **136**, B864–B871 (1964).
- [32] W. Kohn and L. J. Sham, *Phys. Rev.* **140**, A1133–A1138 (1965).
- [33] S. Baroni, S. de Gironcoli, A. Dal Corso, and P. Giannozzi, *Rev. Mod. Phys.* **73**, 515–562 (2001).
- [34] J.-J. Zhou, J. Park, I.-T. Lu, I. Maliyov, X. Tong, and M. Bernardi, *Comput. Phys. Commun.* **264**, 107970 (2021).
- [35] W. Li, *Phys. Rev. B* **92**, 075405 (2015).
- [36] T.-H. Liu, J. Zhou, B. Liao, D. J. Singh, and G. Chen, *Phys. Rev. B* **95**, 075206 (2017).
- [37] J. Ma, A. S. Nissimagoudar, and W. Li, *Phys. Rev. B* **97**, 045201 (2018).
- [38] N.-E. Lee, J.-J. Zhou, L. A. Agapito, and M. Bernardi, *Phys. Rev. B* **97**, 115203 (2018).
- [39] J.-J. Zhou and M. Bernardi, *Phys. Rev. Res.* **1**, 033138 (2019).
- [40] G. Brunin, H. P. C. Miranda, M. Giantomassi, M. Royo, M. Stengel, M. J. Verstraete, X. Gonze, G.-M. Rignanese, and G. Hautier, *Phys. Rev. B* **102**, 094308 (2020).
- [41] V. A. Jhalani, J.-J. Zhou, J. Park, C. E. Dreyer, and M. Bernardi, *Phys. Rev. Lett.* **125**, 136602 (2020).
- [42] C. Zhang and Y. Liu, *Phys. Rev. B* **106**, 115423 (2022).
- [43] A. S. Mishchenko, N. Nagaosa, G. De Filippis, A. de Candia, and V. Cataudella, *Phys. Rev. Lett.* **114**, 146401 (2015).

- [44] L. D. Landau, *Sov. Phys. JETP* **3**, 920–925 (1957).
- [45] C. Jacoboni, C. Canali, G. Ottaviani, and A. Alberigi Quaranta, *Solid-State Electron.* **20**, 77–89 (1977).
- [46] D. L. Rode, *Phys. Rev. B* **2**, 1012–1024 (1970).
- [47] N. W. Ashcroft and N. D. Mermin, *Solid State Physics* (Holt-Saunders, 1976).
- [48] C. Franchini, M. Reticcioli, M. Setvin, and U. Diebold, *Nat. Rev. Mater.* **6**, 560–586 (2021).
- [49] O. Gunnarsson, V. Meden, and K. Schönhammer, *Phys. Rev. B* **50**, 10462–10473 (1994).
- [50] P. J. Robinson, I. S. Dunn, and D. R. Reichman, *Phys. Rev. B* **105**, 224304 (2022).
- [51] A. Mishchenko, N. Prokof'ev, A. Sakamoto, and B. Svistunov, *Phys. Rev. B* **62**, 6317–6336 (2000).
- [52] K. Miyata, D. Meggiolaro, M. T. Trinh, P. P. Joshi, E. Mosconi, S. C. Jones, F. De Angelis, and X.-Y. Zhu, *Sci. Adv.* **3**, e1701217 (2017).
- [53] H. P. R. Frederikse, W. R. Thurber, and W. R. Hosler, *Phys. Rev.* **134**, A442–A445 (1964).
- [54] S. Moser, L. Moreschini, J. Jaćimović, O. S. Barišić, H. Berger, A. Magrez, Y. J. Chang, K. S. Kim, A. Bostwick, E. Rotenberg, L. Forró, and M. Grioni, *Phys. Rev. Lett.* **110**, 196403 (2013).
- [55] A. Bosman and H. Van Daal, *Adv. Phys.* **19**, 1–117 (1970).
- [56] L. Torsi, A. Dodabalapur, L. J. Rothberg, A. W. P. Fung, and H. E. Katz, *Science* **272**, 1462–1464 (1996).
- [57] J. M. Robin, *Phys. Rev. B* **56**, 13634–13637 (1997).
- [58] T. Holstein, *Ann. Phys.* **8**, 343–389 (1959).
- [59] R. A. Marcus, *Rev. Mod. Phys.* **65**, 599–610 (1993).
- [60] P. Giannozzi, S. Baroni, N. Bonini, M. Calandra, R. Car, C. Cavazzoni, D. Ceresoli, G. L. Chiarotti, M. Cococcioni, I. Dabo, A. Dal Corso, S. de Gironcoli, S. Fabris, G. Fratesi, R. Gebauer, U. Gerstmann, C. Gougoussis, A. Kokalj, M. Lazzeri, L. Martin-Samos, N. Marzari, F. Mauri, R. Mazzarello, S. Paolini, A. Pasquarello, L. Paulatto, C. Sbraccia, S. Scandolo, G. Sclauzero, A. P. Seitsonen, A. Smogunov, P. Umari, and R. M. Wentzcovitch, *J. Phys. Condens. Matter* **21**, 395502 (2009).

- [61] P. Giannozzi, O. Andreussi, T. Brumme, O. Bunau, M. Buongiorno Nardelli, M. Calandra, R. Car, C. Cavazzoni, D. Ceresoli, M. Cococcioni, N. Colonna, I. Carnimeo, A. Dal Corso, S. de Gironcoli, P. Delugas, R. A. DiStasio, A. Ferretti, A. Floris, G. Fratesi, G. Fugallo, R. Gebauer, U. Gerstmann, F. Giustino, T. Gorni, J. Jia, M. Kawamura, H.-Y. Ko, A. Kokalj, E. Küçükbenli, M. Lazzeri, M. Marsili, N. Marzari, F. Mauri, N. L. Nguyen, H.-V. Nguyen, A. Otero-de-la-Roza, L. Paulatto, S. Poncé, D. Rocca, R. Sabatini, B. Santra, M. Schlipf, A. P. Seitsonen, A. Smogunov, I. Timrov, T. Thonhauser, P. Umari, N. Vast, X. Wu, and S. Baroni, *J. Phys. Condens. Matter* **29**, 465901 (2017).
- [62] L. Hedin, *Phys. Rev.* **139**, A796–A823 (1965).
- [63] A. Marini, C. Hogan, M. Grüning, and D. Varsano, *Comput. Phys. Commun.* **180**, 1392–1403 (2009).
- [64] B. Himmetoglu, A. Floris, S. De Gironcoli, and M. Cococcioni, *Int. J. Quantum Chem.* **114**, 14–49 (2014).
- [65] I. Timrov, N. Marzari, and M. Cococcioni, *Phys. Rev. B* **103**, 045141 (2021).
- [66] I. Timrov, N. Marzari, and M. Cococcioni, *Comput. Phys. Commun.* **279**, 108455 (2022).
- [67] A. Floris, I. Timrov, B. Himmetoglu, N. Marzari, S. de Gironcoli, and M. Cococcioni, *Phys. Rev. B* **101**, 064305 (2020).
- [68] L. Monacelli, R. Bianco, M. Cherubini, M. Calandra, I. Errea, and F. Mauri, *J. Phys. Condens. Matter* **33**, 363001 (2021).
- [69] N. Marzari, A. A. Mostofi, J. R. Yates, I. Souza, and D. Vanderbilt, *Rev. Mod. Phys.* **84**, 1419–1475 (2012).
- [70] A. A. Mostofi, J. R. Yates, Y.-S. Lee, I. Souza, D. Vanderbilt, and N. Marzari, *Comput. Phys. Commun.* **178**, 685–699 (2008).
- [71] G. Pizzi, D. Volja, B. Kozinsky, M. Fornari, and N. Marzari, *Comput. Phys. Commun.* **185**, 422–429 (2014).
- [72] S. M. Story, J. J. Kas, F. D. Vila, M. J. Verstraete, and J. J. Rehr, *Phys. Rev. B* **90**, 195135 (2014).
- [73] J. J. Kas, J. J. Rehr, and L. Reining, *Phys. Rev. B* **90**, 085112 (2014).
- [74] E. N. Economou, *Green's Functions In Quantum Physics*, Vol. 7, Springer Series in Solid-State Sciences (Springer Berlin, Heidelberg, 2006).
- [75] M. Schlipf and F. Giustino, *Phys. Rev. Lett.* **127**, 237601 (2021).

BANDLIKE CHARGE CARRIER MOBILITY IN ORGANIC CRYSTALS

This chapter is a slightly modified version of the manuscript: B. K. Chang and M. Bernardi, “Bandlike charge carrier mobility in organic crystals from first-principles calculations”, *submitted* (2024).

2.1 Introduction

The commonly low charge carrier mobility in organic molecular crystals (OMCs) is a bottleneck for bringing organic materials into real-world electronic applications. OMCs typically have a charge carrier mobility below $10 \text{ cm}^2\text{V}^{-1}\text{s}^{-1}$ [1, 2], which is significantly lower than the $\sim 10^3 \text{ cm}^2\text{V}^{-1}\text{s}^{-1}$ seen in traditional semiconductors like silicon and germanium. In addition, due to the complex electron-phonon (*e-ph*) interactions and crystal structures, OMCs host a wide range of charge transport mechanisms, including bandlike, hopping, and intermediate regimes [3–5], each exhibiting a different magnitude and temperature dependence of mobility. Even in the same OMC, electron and hole carriers in different crystallographic directions may exhibit various transport regimes [6].

Predicting the charge carrier mobility in OMCs is challenging yet critical to the development of high-performance organic electronics [7]. Typical modeling techniques [8, 9] start with a model *e-ph* Hamiltonian and, based on the transport regime, compute the mobility with suitable transport formalisms, such as the Boltzmann transport equation (BTE) [10], Kubo formula [11], transient localization [12], and hybrid formulations [13]. These methods have offered significant insights, such as identifying the roles of intra- and intermolecular phonons in *e-ph* dynamics [14] and exploring potential engineering approaches [15]. Nonetheless, calculations based on simplified models usually rely on fitting model parameters to experiments and do not include all phonon modes, which limit their predictability. In response to these limitations, first-principles (parameter-free) approaches that account for all phonon modes and *e-ph* couplings are emerging, and have shown promising accuracy and explanatory power in studies of charge transport in OMCs [6, 16–19].

Among the charge transport regimes in OMCs, the bandlike regime is pivotal for

achieving high charge carrier mobility [20–22]. Typically found in ultrapure OMCs, the bandlike charge carriers are characterized by mobilities with a magnitude near or greater than $1 \text{ cm}^2 \text{V}^{-1} \text{s}^{-1}$ at room temperature and with a power-law temperature dependence [20]. Their charge transport mechanism is governed by the scattering of delocalized electronic states [17, 18, 23, 24], similar to the charge transport mechanism in conventional inorganic semiconductors. However, while the charge carrier mobility in a wide range of simple inorganic materials can be accurately predicted using first-principles BTE approaches [25–28], similar calculations for OMCs remain scarce [6, 16], mainly due to the large unit cells (ranging from a few tens to a few hundred atoms) of OMCs that make computation challenging.

In this study, we apply first-principles *e*-ph and BTE calculations to investigate the bandlike charge transport in the crystals of benzene, anthracene, tetracene, pentacene, and biphenyl. Our computed charge carrier mobilities are within a factor of 2–3 of experimental averages and accurately reflect the power-law temperature dependence throughout 100–400 K, achieving the accuracy previously demonstrated on naphthalene [6]. Focusing on studying four of the computed OMCs, we discover that the bandlike mobilities are predominantly limited by the *e*-ph scattering from the low-frequency (LF) phonons below 150 cm^{-1} , despite the phonon spectra extending beyond 3000 cm^{-1} . These LF phonons, while inducing the highest *e*-ph scattering rates, exhibit significantly weaker coupling to charge carriers compared to the most strongly-coupled C=C bond-stretching modes at $1,500\text{--}1600 \text{ cm}^{-1}$. We develop a method to quantify the inter- and intramolecular characters of phonon modes in momentum space, and show that the LF phonons are primarily intermolecular vibrations with an increasing long-range intramolecular traits, such as backbone torsion and bending, as the size of molecule increases.

Finally, we examine the effects of strain on bandlike charge carriers. We show that moderate compressive strain induces modulations in the electronic structure and *e*-ph scattering rate that both contribute to the enhancement of mobility. Furthermore, the scattering rates of LF modes are particularly responsive to strain, more so than those of other modes, providing evidence of the effectiveness of strain engineering in OMCs—a research area that has attracted growing interest recently [29–32]. Taken together, this work offers a rigorous understanding of the microscopic details of bandlike transport mechanism and provides insights toward achieving high-mobility charge transport in OMCs.

2.2 Methodology

We compute the ground state electronic structure of benzene, anthracene, tetracene, pentacene, and biphenyl crystals, using plane-wave density functional theory (DFT) calculations with the QUANTUM ESPRESSO code [33, 34]. We use a kinetic energy cutoff of 90 Ry and employ the generalized gradient approximation [35] and norm-conserving pseudopotentials [36] from Pseudo Dojo [37]. The lattice parameters and initial atomic positions are adopted from experiments for each OMC, as detailed in the supplementary material (SM) in Sec. 2.5. The atomic positions are relaxed using DFT including the Grimme van der Waals correction [38, 39]. The WANNIER90 code [40] is employed to obtain Wannier functions and the corresponding transformation matrices, using the selected-columns-of-the-density-matrix method [41]. We obtain the lattice dynamics and e -ph perturbation potentials from density functional perturbation theory (DFPT) [42]. The momentum grids for DFT and DFPT used for each OMC are provided in the SM (Sec. 2.5). We note that quantum nuclear effects and finite-temperature effects, which are not directly addressed in the DFPT calculations, can contribute to lattice dynamics. These effects play a critical role in determining the thermal properties of organic crystals and can be captured using approaches such as the temperature-dependent effective potential method (TDEP) [43].

Using the PERTURBO code [44], we compute the e -ph interactions and the charge transport. The electron and phonon data are combined to form the e -ph coupling matrix elements [26, 44]

$$g_{mn\nu}(\mathbf{k}, \mathbf{q}) = \sqrt{\frac{\hbar}{2\omega_{\nu\mathbf{q}}}} \sum_{\kappa\alpha} \frac{\mathbf{e}_{\nu\mathbf{q}}^{\kappa\alpha}}{\sqrt{M_{\kappa}}} \langle m\mathbf{k} + \mathbf{q} | \partial_{\mathbf{q}\kappa\alpha} V | n\mathbf{k} \rangle, \quad (2.1)$$

which quantifies the probability amplitude for an electron Bloch state $\psi_{n\mathbf{k}}$, with band index n and crystal momentum \mathbf{k} , to scatter into a final state $\psi_{m\mathbf{k}+\mathbf{q}}$ by emitting or absorbing a phonon with mode index ν , wavevector \mathbf{q} , energy $\omega_{\nu\mathbf{q}}$, perturbation potential $\partial_{\mathbf{q}\kappa\alpha} V$, and displacement eigenvector $\mathbf{e}_{\nu\mathbf{q}}$ [26, 34, 44]. Here α is the Cartesian direction and M_{κ} is the mass of atom κ . The e -ph scattering rate for each electronic state is calculated using the interpolated matrix elements as [26, 44]

$$\Gamma_{n\mathbf{k}}(T) = \sum_{\nu} \Gamma_{n\mathbf{k}}^{(\nu)}(T), \quad (2.2)$$

where T is the temperature, and $\Gamma_{n\mathbf{k}}^{(\nu)}$ is the mode-resolved scattering rate:

$$\begin{aligned} \Gamma_{n\mathbf{k}}^{(\nu)}(T) = & \frac{2\pi}{\hbar} \sum_{m\mathbf{q}} |g_{mn\nu}(\mathbf{k}, \mathbf{q})|^2 \\ & \times [(N_{\nu\mathbf{q}} + 1 - f_{m\mathbf{k}+\mathbf{q}})\delta(\varepsilon_{n\mathbf{k}} - \varepsilon_{n\mathbf{k}+\mathbf{q}} - \omega_{\nu\mathbf{q}}) \\ & + (N_{\nu\mathbf{q}} + f_{m\mathbf{k}+\mathbf{q}})\delta(\varepsilon_{n\mathbf{k}} - \varepsilon_{n\mathbf{k}+\mathbf{q}} + \omega_{\nu\mathbf{q}})]. \end{aligned} \quad (2.3)$$

Here $\varepsilon_{n\mathbf{k}}$ is the electron band energy, and $f_{n\mathbf{k}}$ and $N_{\nu\mathbf{q}}$ are the electron Fermi-Dirac and phonon Bose-Einstein occupations in thermal equilibrium, respectively, that account for the temperature dependence of the scattering rate. The charge carrier mobility tensor is obtained within the BTE framework in the relaxation time approximation [26, 44]:

$$\mu_{\alpha\beta}(T) = \frac{e}{n_c} \int dE \left(-\frac{\partial f(E, T)}{\partial E} \right) \Sigma_{\alpha\beta}(E, T), \quad (2.4)$$

where α and β are Cartesian directions parallel to the crystal principal axes, e is the electronic charge, E the electron energy, f the electronic Fermi-Dirac distribution, and n_c is the carrier concentration fixed at 10^{17} – 10^{18} cm^{-3} , a typical value for both inorganic [44] and organic semiconductors [45]. $\Sigma_{\alpha\beta}$ is the transport distribution function (TDF) defined as

$$\Sigma_{\alpha\beta}(E, T) = \frac{2}{V_{\text{uc}}} \sum_{n\mathbf{k}} \tau_{n\mathbf{k}}(T) v_{n\mathbf{k}}^\alpha v_{n\mathbf{k}}^\beta \delta(E - \varepsilon_{n\mathbf{k}}), \quad (2.5)$$

where V_{uc} is the unit cell volume, $v_{n\mathbf{k}}$ are the electron band velocities, and $\tau_{n\mathbf{k}}(T) = \Gamma_{n\mathbf{k}}^{-1}(T)$ are the e -ph relaxation times. The mobility calculations use 10^5 – 10^6 randomly selected \mathbf{q} -points and a fine \mathbf{k} -grid of about 50^3 (see Sec. 2.5 for additional computational details).

2.3 Results

Charge carrier mobility

We validate the accuracy and applicability of the first-principles BTE approach by extensively comparing the computed mobilities to experiments. For an OMC, we label the mobility as $\mu_\alpha^{(q)}$, where q is the charge carrier type that is either e (electron) or h (hole), and α indicates the direction along which the mobility is computed or measured. α can be the crystal principal axis of a , b , or c^* , or avg indicating the mobility averaged over three spatial directions. Here we compare the calculations and the experimental measurements for six OMC charge carrier mobilities: benzene's $\mu_a^{(e)}$, naphthalene's $\mu_a^{(h)}$, anthracene's $\mu_{c^*}^{(h)}$, tetracene's $\mu_{c^*}^{(h)}$, pentacene's

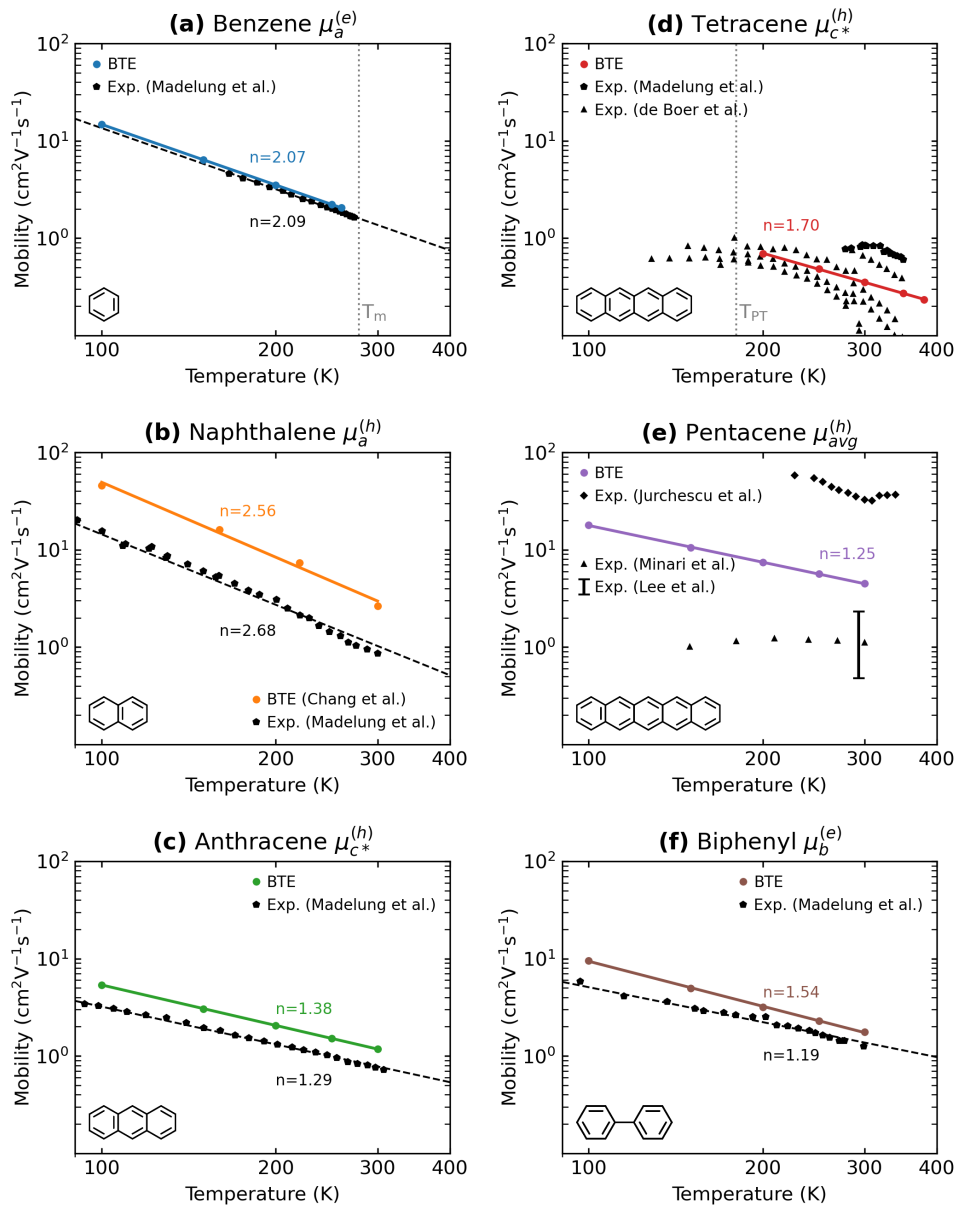


Figure 2.1: Charge carrier mobilities for (a) benzene’s electron in the a -direction, (b) naphthalene’s hole in the a -direction, (c) anthracene’s hole in the c^* -direction, (d) tetracene’s hole in the c^* -direction, (e) pentacene’s hole averaged over the three crystal principal directions, and (f) biphenyl’s electron in the b -direction. Data points represent BTE-calculated (colored) and experimental (black) mobilities. Solid and dashed lines indicate fits to the power law T^{-n} , with the exponent n noted for each. BTE data for naphthalene [6] are obtained with temperature-dependent lattice parameters and GW correction. Experimental data are adopted from Refs. [46–54]. The melting point of benzene ($T_m = 279$ K) and the phase-transition temperature of tetracene ($T_{PT} = 180$ K) [50] are indicated by vertical dashed lines.

$\mu_{avg}^{(h)}$, and biphenyl's $\mu_b^{(e)}$. These mobilities are chosen as examples due to that they have experimentally measured mobilities that span a wide temperature range between 100–400 K and exhibit the bandlike power-law temperature dependence, such that both the magnitude and the temperature dependence can be comprehensively compared to our calculations.

Figure 2.1(a), (b), (c), and (f) show the experimental and computed mobilities for benzene, naphthalene, anthracene, and biphenyl. Our calculations are highly accurate, in agreement with the experiments within a factor of 2–3 throughout the temperature range of 100–300 K. In particular, the computed mobilities for naphthalene are adopted from Ref. [6], in which the calculations for the other two directions show similar accuracy [6]. In the case of benzene, the calculations are almost in exact agreement with the experiments. The computed mobilities in all four cases are slightly above the experimental values, as expected for the case of phonon-limited mobility. The exponent n of the power-law temperature dependence T^{-n} is in excellent agreement with experiments for benzene, naphthalene, and anthracene, with a less than 7% error. For biphenyl, the computed exponent is slightly overestimated compared to the experiment, with a 29% error. This might be due the electron charge transport in biphenyl being close to the boundary between the bandlike and the intermediate regimes [6], where the mobility exhibits a weaker power-law temperature dependence.

The mobilities for tetracene are shown in Fig. 2.1(d). The experimental mobilities [49, 50] from multiple samples show a consistent decrease in mobility above the phase transition temperature at 180 K [50]. Although they do not strictly follow a power-law temperature dependence, photoconductivity experiments [55, 56] showed strong evidence of coherent bandlike transport in tetracene. As shown in Fig. 2.1(d), our computed mobilities are in great agreement with the experimental average within a factor of 2 throughout 200–400 K, exhibiting a power-law temperature dependence.

Pentacene has received major attention due to its potentially high charge carrier mobilities. As shown in Fig. 2.1(e), Jurchescu *et al.* [51] observed a hole mobility of around $35 \text{ cm}^2\text{V}^{-1}\text{s}^{-1}$ between 220–340 K. Additionally, due to the near-power-law temperature dependence, the hole mobility in pentacene is considered bandlike [51]. However, separate experiments by Minari *et al.* [52] and Lee *et al.* [53] have observed much lower mobilities of around $\sim 1 \text{ cm}^2\text{V}^{-1}\text{s}^{-1}$ between 150–300 K, also shown in Fig. 2.1(e). Here we compute the hole mobilities in pentacene and obtain results that

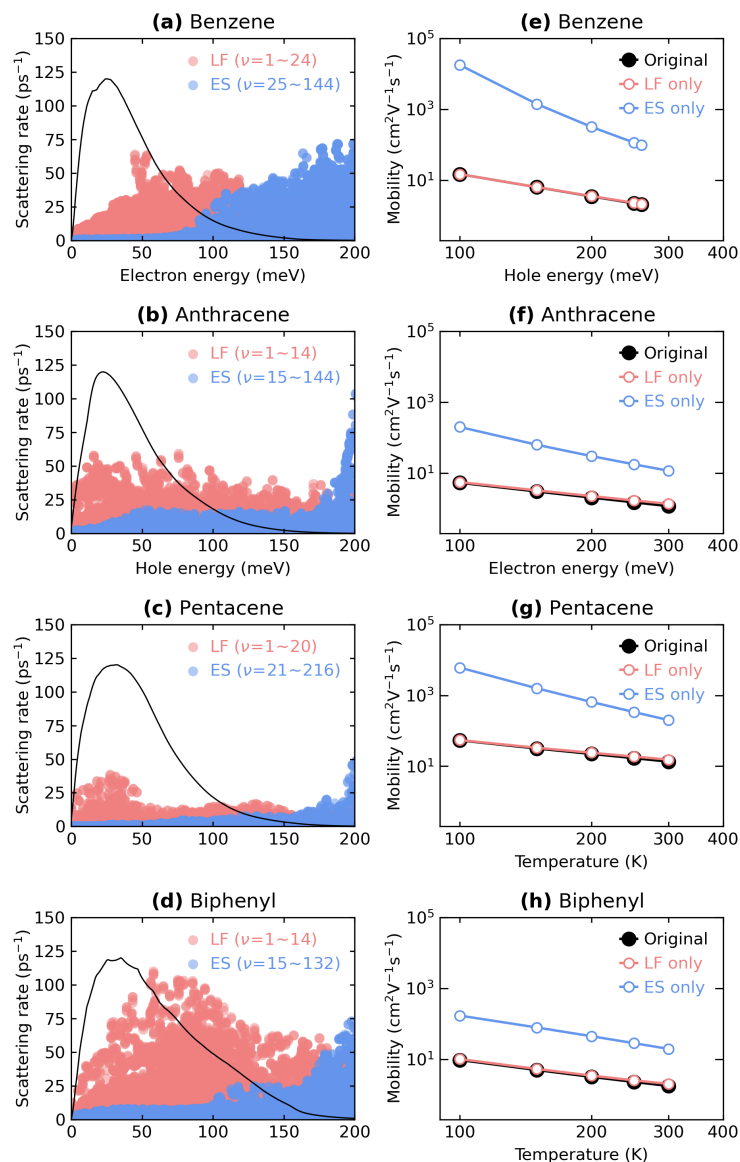


Figure 2.2: Scattering rates and their impact on mobility. The left column [(a)–(d)] displays the mode-resolved scattering rates for benzene’s electron, anthracene’s hole, pentacene’s hole, and biphenyl’s electron, respectively. The scattering rates are computed at 260 K for benzene and at room temperature for the others. Red represents the low-frequency (LF) modes, and blue denotes the extended-spectrum (ES) modes, each with their mode index (ν) range specified. Energy zero corresponds to the valence band maximum for holes and the conduction band minimum for electrons, increasing deeper into the bands. The black curves represent the transport distribution functions (TDFs, Eq. 2.5) for comparison. The right column [(e)–(h)] presents the mobility calculations, showing the original (black), LF-only (red), and ES-only mobilities (blue).

lie in the middle of the two experimental extremes, with a value of $\sim 5 \text{ cm}^2\text{V}^{-1}\text{s}^{-1}$ at room temperature [Fig. 2.1(e)]. Our results suggest that pentacene indeed exhibits a particularly high mobility compared to all other OMC systems studied in this work ($< 3 \text{ cm}^2\text{V}^{-1}\text{s}^{-1}$ at room temperature), but might not be as high as that reported by Jurchesc *et al.* [51]. As a brief summary, we have shown that first-principles BTE calculations are able to provide highly accurate predictions to the charge carrier mobilities in OMCs.

Electron-phonon scattering rate

Having confirmed the accurate prediction of charge carrier mobilities, we explore the characteristics of the bandlike transport mechanism. To concisely elucidate the relationship of molecular structure, *e*-ph interactions, and charge transport dynamics, the remainder of this chapter will focus on benzene's $\mu_a^{(e)}$, anthracene's $\mu_{c^*}^{(h)}$, pentacene's $\mu_{avg}^{(h)}$, and biphenyl's $\mu_b^{(e)}$, as shown in Fig. 2.1(a), (c), (e), and (f), respectively. Henceforth, these four crystals and charge carriers will be collectively referred to as “the systems”, and the $\mu_\alpha^{(q)}$ notation will be omitted in the discussions for brevity.

In OMCs, which usually consist of tens to hundreds of atoms per unit cell and therefore hundreds of phonon modes, understanding the impact of each mode on charge transport is crucial for developing efficient engineering strategies to enhance mobility. The mode-resolved *e*-ph scattering rate (Eq. 2.3) quantifies individual phonon modes' contributions to the overall scattering rate of an electronic state. For the band-edge electronic states in the systems, we find that phonons with lower frequencies generally contribute to higher *e*-ph scattering rates. To differentiate the phonons, we use the lowest-energy gap in the phonon spectra to divide the modes into two groups: those below the gap are termed low-frequency (LF) modes, and those above are termed extended-spectrum (ES) modes. This energy gap is consistently found between $100\text{--}150 \text{ cm}^{-1}$ across the systems. For context, the highest phonon mode frequency in these systems is around $3,100 \text{ cm}^{-1}$ (see SM in Sec. 2.5 for the complete phonon spectra of the systems).

Fig. 2.2(a)–(d) present the mode-resolved scattering rates (Eq. 2.3) as a function of charge carrier energy computed at or near room temperature for the systems, alongside their corresponding TDFs (Eq. 2.5). The TDFs indicate that the mobilities are mainly contributed by charge carriers within 150 meV from the band edges. In this energy range, the scattering rates from LF modes can be multiple times higher

than those from ES modes. Specifically, the highest LF-mode scattering rates are approximately 65, 60, 35, and 115 ps^{-1} , while the highest ES-mode scattering rates are around 50, 20, 10, and 25 ps^{-1} for benzene, anthracene, pentacene, and biphenyl, respectively. Notably, pentacene shows particularly low scattering rates for both LF and ES modes, consistent with its high mobility observed in experiments and in our calculations. For charge carriers over 150 meV away from the band edges, ES-mode scattering rates surpass LF mode's due to the energies of charge carrier becoming comparable to those of ES phonon modes, enabling scattering processes of ES-phonon emissions [16]. However, these carriers contribute minimally to mobility within the relevant temperature range, as indicated by the TDFs.

Comparing the LF- and ES-mode scattering rates with the TDFs qualitatively indicates that the LF modes play a greater role in limiting the charge carrier mobilities than the ES modes. However, quantifying their exact contributions to charge transport is not trivial, as mobilities are inversely related to the sum of scattering rates (Eqs. 2.2–2.5). Here we calculate partially-limited mobilities by considering the scattering rates of only the LF or the ES modes. The difference between the partially-limited mobilities and the original mobilities inversely quantifies the significance of the scattering processes in consideration. Specifically, a smaller difference signifies greater importance of these scattering processes in limiting charge transport. As shown in Fig. 2.2(e)–(h), the LF-only mobilities are nearly identical to the original mobilities, with the largest difference being 16% for anthracene at 300 K. In contrast, the ES-only mobilities are significantly higher than the original mobility, with the largest difference ranging from 900% for anthracene at 300 K to 120,000% for benzene at 100 K. These results show that LF-mode scattering processes predominantly limit the overall charge transport. Notably, the discrepancies between the ES-only and original mobilities are less pronounced at higher temperature. This trend is expected, since the ES phonon modes are significantly more populated at higher temperatures, thus contributing more to limiting mobility.

The mode-resolved analysis reveals that, at or near room temperature, bandlike charge carrier mobilities in OMCs are predominantly limited by the e -ph scattering from LF modes. Considering that the LF modes constitute phonons below 150 cm^{-1} in a spectrum extending beyond 3,000 cm^{-1} , our findings point to the potential of engineering strategies that target LF modes to tune the mobilities of bandlike charge carriers in OMCs.

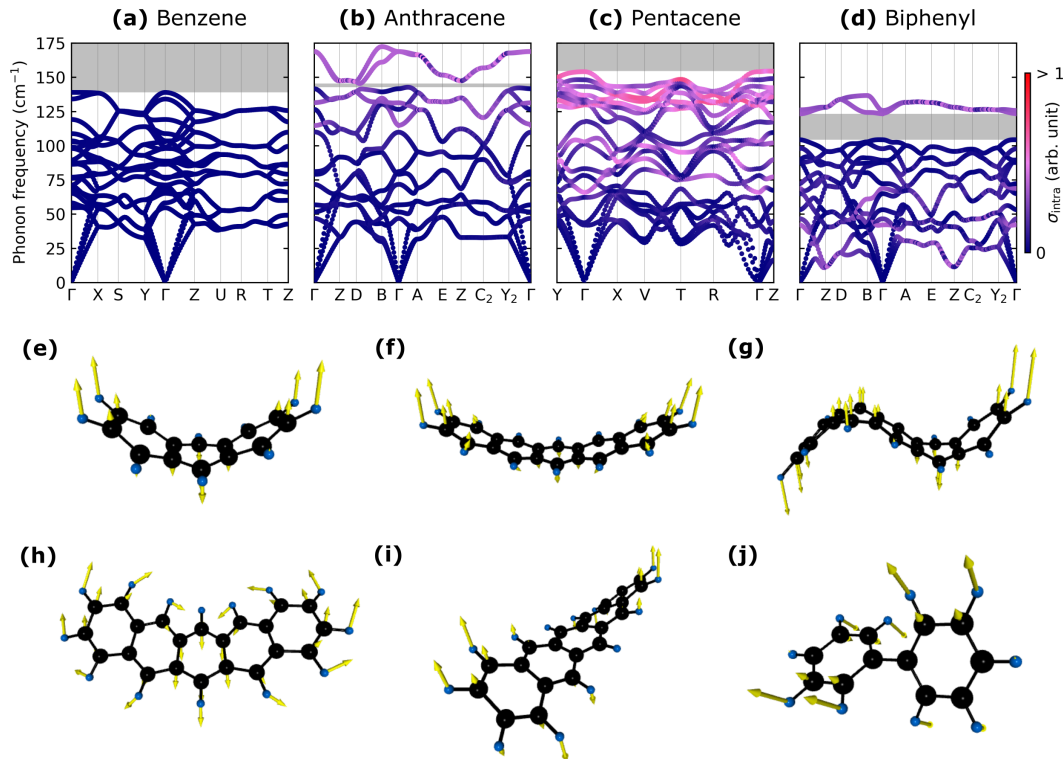


Figure 2.3: Low-frequency (LF) phonon modes in the systems. Panels (a)–(d) show the LF phonon dispersions for benzene, anthracene, pentacene, and biphenyl, respectively. The color gradient from blue to red indicates increasing intramolecular character (σ_{intra} , Eq. 2.6). Grey regions represent the energy gaps separating the LF modes from others. The high-symmetry points follow the definition in Ref. [57]. Panels (e)–(j) visualize the intramolecular motions in the LF modes: (e) anthracene’s out-of-plane bending, (f) pentacene’s out-of-plane bending, (g) pentacene’s out-of-plane double-bending, (h) pentacene’s in-plane bending, (i) pentacene’s torsioning, and (j) biphenyl’s torsioning. Carbon and hydrogen atoms are represented by black and blue spheres, respectively, with displacement vectors shown as yellow arrows.

Low-frequency phonon modes

Insights into vibrational patterns of phonons help inform the development of engineering techniques for OMCs [58]. Phonons in OMCs are typically categorized into two groups: 1) intermolecular modes, characterized by rigid-body movements of the molecules at lower frequencies, and 2) intramolecular modes, involving higher-frequency atomic vibrations that deform the molecules. These two types of phonons distinctly influence charge transport [14, 59], and their e -ph interactions are often described by specific models, such as Peierls- and Holstein-type e -ph Hamiltonians [14]. Although LF phonons are predominantly intermolecular, it is recognized that phonons can exhibit both inter- and intramolecular characteristics [58, 60],

resulting in a hybridization of molecular rigid-body movements and deformations. This goes beyond the description of simplified models, but can be captured in our first-principles calculations.

Here we present a method to quantify the intramolecular character of phonons in momentum space. In cheminformatics and bioinformatics, the minimal root-mean-square deviation (RMSD) of atomic positions is a well-known metric for measuring differences between molecule and protein structures [61]. This is computed by first aligning the centroids of two molecules to remove relative translational difference, then applying the Kabsch algorithm [62, 63] to obtain the optimal relative rotation of the molecules. Based on this metric, we define the intramolecular character σ_{intra} of a phonon (ν, \mathbf{q}) as the time-averaged minimal RMSD of atomic positions between the phonon-displaced structure of a molecule and its original structure. This is formally written as

$$\sigma_{\text{intra}}(\nu, \mathbf{q}) = \left\langle \sqrt{\min_{\mathcal{R}} \left[\frac{1}{A^2 \cdot N_{\text{apm}}} \sum_{\kappa \in \Phi} \|\mathcal{R}\tilde{\mathbf{r}}_{\kappa}(\nu, \mathbf{q}, t) - \mathbf{r}_{\kappa}\|^2 \right]} \right\rangle, \quad (2.6)$$

where Φ denotes a selected molecule in the OMC, N_{apm} is the number of atoms per molecule, \mathbf{r}_{κ} is the equilibrium position of atom κ in Φ , A is the vibration amplitude, and t is the time. \mathcal{R} is the 3D rotation operator, $\langle \cdot \rangle$ denotes the time average, and

$$\tilde{\mathbf{r}}_{\kappa}(\nu, \mathbf{q}, t) = \mathbf{r}_{\kappa} + \text{Re} \left[\frac{A}{M_{\kappa}} \mathbf{e}_{\nu\mathbf{q}}^{\kappa\alpha} e^{i(\mathbf{q}\cdot\mathbf{r}_{\kappa} - \omega_{\nu\mathbf{q}}t)} \right] - \frac{1}{N_{\text{apm}}} \sum_{\kappa' \in \Phi} \mathbf{r}_{\kappa'} \quad (2.7)$$

is the position of atom κ after Φ is displaced by the phonon (ν, \mathbf{q}) at time t and its centroid aligned. The Kabsch algorithm [62, 63] is employed for the minimization with respect to \mathcal{R} in Eq. 2.6. With these definitions, σ_{intra} quantifies the intramolecular character of a phonon by excluding its intermolecular components.

Fig. 2.3(a)–(d) display the LF-mode dispersions and intramolecular characters for the systems. The LF-modes in one-ring benzene [Fig. 2.3(a)] exhibit no intramolecular characters, a trait shared with two-ring naphthalene [16, 58], where the LF modes below the lowest-energy phonon gap are completely intermolecular. In three-ring anthracene [Fig. 2.3(b)], the LF modes above 125 cm^{-1} start to show intramolecular features associated with out-of-plane backbone bending, as depicted in Fig. 2.3(e). For five-ring pentacene [Fig. 2.3(c)], similar bending exists at 75 cm^{-1} , as illustrated in Fig. 2.3(f). Additionally, from 75 to 150 cm^{-1} , more intramolecular features emerge, including out-of-plane double-bending, in-plane bending, and backbone torsioning, as illustrated in Fig. 2.3(g)–(i), respectively. Nevertheless,

the LF modes in pentacene below 75 cm^{-1} remain purely intermolecular. Finally, biphenyl [Fig. 2.3(d)], unlike its acene counterpart naphthalene, exhibits intramolecular characters in the LF-phonons at low frequencies of $25\text{--}50 \text{ cm}^{-1}$. This is due to the C–C single bond linking the two rings that facilitate tortioning motion, as shown in Fig. 2.3(j). The complete phonon spectra overlaid with their intramolecular characters for the systems are provided in the SM (Sec. 2.5).

Our findings indicate that LF modes are predominantly intermolecular, with increasing long-range intramolecular characteristics as structural degrees of freedom increase. The LF intramolecular vibrations occur on a molecular scale, unlike the bond-scale intramolecular vibrations typically observed in infrared (IR) spectroscopy. For oligoacenes, the minimum chain length to permit in-plane backbone bending in LF modes appears to be two to three aromatic rings, as evidenced by anthracene (three rings) being the smallest acene showcasing out-of-plane bending and pentacene (five rings) demonstrating at most double bending. In-plane bending and backbone torsioning become available in the LF modes only with a minimal chain length of 4–5 rings. The presence of a phenyl group, or a C–C single bond linking two rings, readily introduces torsioning along the ring linkage at low frequencies. These analyses establish the relationship between structural and vibrational properties in OMCs and provide insights into designing engineering approaches.

Electron-phonon coupling

To investigate why LF modes contribute significantly to the e -ph scattering rates, we analyze the e -ph coupling using the coupling distribution function, akin to a density of states for e -ph interactions, defined as

$$\gamma_{\mathbf{k}}(\omega) = \sum_{\nu\mathbf{q}} |g_{\nu}(\mathbf{k}, \mathbf{q})|^2 \delta(\omega - \omega_{\nu\mathbf{q}}), \quad (2.8)$$

where

$$|g_{\nu}(\mathbf{k}, \mathbf{q})| = \sqrt{\sum_{mn} |g_{mn\nu}(\mathbf{k}, \mathbf{q})|^2 / N_b} \quad (2.9)$$

is the gauge-invariant e -ph coupling with N_b being the number of Wannier bands [44].

Figure 2.4 (a)–(d) present the e -ph coupling distribution functions calculated at the band edges for the systems. Peaks within these curves align with vibrational modes of specific functional groups. All systems feature a large energy gap between $1,700\text{--}3,000 \text{ cm}^{-1}$ and a weak coupling peak at $3,100 \text{ cm}^{-1}$ associated with C–H stretching modes. The region from $500\text{--}1,500 \text{ cm}^{-1}$ is characterized by a series of

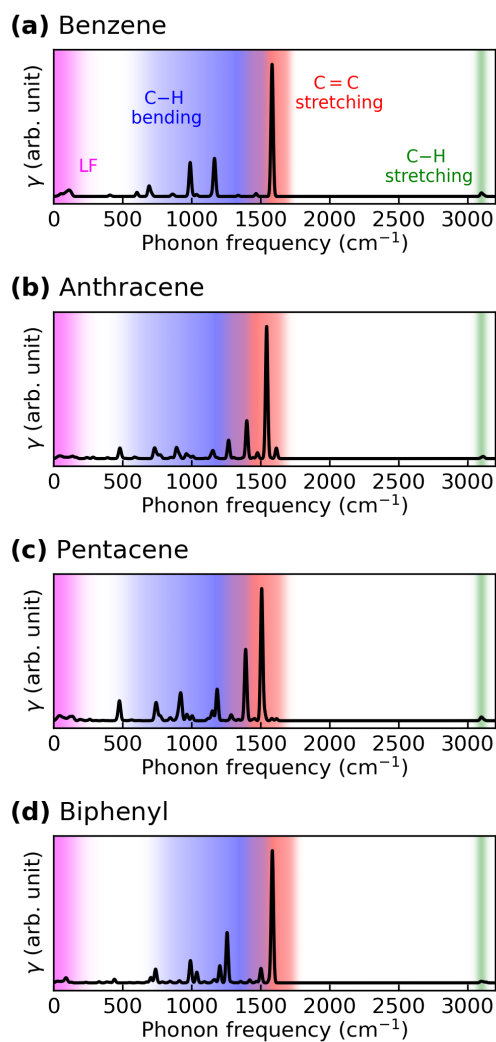


Figure 2.4: Electron-phonon (e -ph) coupling distribution function $\gamma_{\mathbf{k}}$ (Eq. 2.8) computed at the band edges for (a) benzene electrons, (b) anthracene hole, (c) pentacene holes, and (d) biphenyl electrons. The colors indicate different energy ranges of phonon modes: pink for low-frequency (LF) modes, blue for C–H bending, red for C=C stretching, and green for C–H stretching.

moderate coupling peaks, which mainly correspond to C–H bond bending modes. Notably, the strongest coupling peaks are at 1,500–1,700 cm^{-1} , attributed to C=C stretching. Contrary to expectations, the LF modes below 150 cm^{-1} , despite being the primary contributors to the e -ph scattering rates, show minimal coupling, even weaker than those of moderate strength.

Our results suggest that near room temperature, the pronounced e -ph scattering rates from LF modes for the bandlike charge carriers are not caused by strong e -ph coupling. Instead, they arise from the great scattering phase space, determined by the interplay of electronic band structure, phonon dispersion, and thermal populations of electrons and phonons (Eq. 2.2).

Strain effects

The application of strain engineering to enhance charge carrier mobilities in OMCs has been validated experimentally [29–32], yet the underlying mechanisms remain debated [15]. Here we study the strain effects on the bandlike charge transport by computing the mobilities under 2.5% homogeneous compressive strain, achieved by reducing the cell sizes. As shown in Fig. 2.5(a)–(d), compressive strain consistently improves mobilities across the 100 to 300 K temperature range by factors of 1.5 to 3, aligning with experimental findings that moderate compressive strain boosts mobilities in OMCs [29, 30, 32]. Furthermore, the strain can increase the mobility’s power-law temperature dependency, which is particularly pronounced in anthracene.

Within the BTE framework (Eqs. 2.4 and 2.5), at a fixed temperature and constant carrier concentration, strain influences mobility through modulations of e -ph relaxation times ($\tau_{n\mathbf{k}}$) and parameters determined solely by electronic structure (band velocities $v_{n\mathbf{k}}$ and energies $\varepsilon_{n\mathbf{k}}$). To disentangle the contributions from e -ph scattering and purely electronic factors, we compute “fictitious” mobilities using a combination of parameters from both strained and unstrained calculations. Let τ represent the set of e -ph relaxation times, ε the electronic structure, and $\hat{\cdot}$ their strained counterparts, we assess the e -ph scattering contribution with fictitious mobility $\varepsilon\hat{\tau}$, computed from unstrained electronic structures and strained relaxation times, and electronic contribution with fictitious mobility $\hat{\varepsilon}\tau$, computed from strained electronic structures and unstrained relaxation times. As shown in Fig. 2.5(a)–(d), these fictitious mobilities surpass the original mobility across all temperatures, indicating that both e -ph scattering and electronic modulations contribute to enhance mobility under the compressive strain. Additionally, $\varepsilon\hat{\tau}$ is comparable to [Fig. 2.5(a) and (c)] or

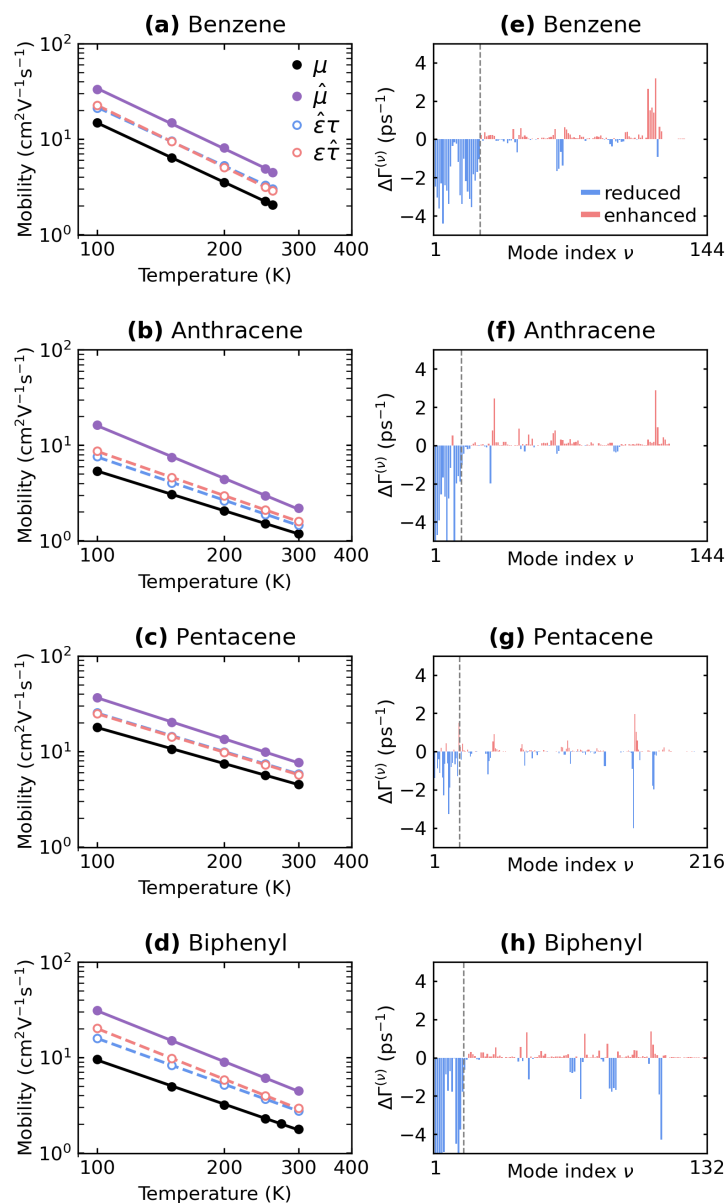


Figure 2.5: Impact of 2.5% homogeneous compressive strain on mobilities and electron-phonon (e -ph) scattering. The left column [(a)–(d)] displays computed mobilities for benzene, anthracene, pentacene, and biphenyl. Black markers represent original mobility μ , purple indicates mobility under strain ($\hat{\mu}$), blue denotes fictitious mobility computed from strained electronic structure and unstrained e -ph relaxation times ($\hat{\epsilon}\tau$), and red shows fictitious mobility calculated with strained e -ph relaxation times and unstrained electronic structure ($\epsilon\hat{\tau}$). The right column [(e)–(h)] illustrates changes in average mode-resolved e -ph scattering rates $[\Delta\Gamma^{(\nu)}]$ due to strain. Blue bars indicate a reduction, and red bars an enhancement in scattering rates. Vertical dashed lines separate the low-frequency (LF) phonon modes (left of the lines) from the extended spectrum (ES) modes (right of the lines).

slightly exceeds [Fig. 2.5(b) and (d)] than $\hat{\epsilon}\tau$ in all cases, implying that e -ph scattering plays a role as substantial as, or even greater than, electronic structure in the strain-induced mobility modulations.

We explore the mechanisms behind the observed mobility enhancements. The enhancement due to electronic structure can be ascribed to band stretching under compressive strain, which increases the electron band velocity. The strain-stretched band structures for the systems are available in the SM (Sec. 2.5). To understand the enhancement from e -ph scattering, we define the average mode-resolved scattering rates as $\Gamma^{(\nu)} = \sum_{n\mathbf{k}} \Gamma_{n\mathbf{k}}^{(\nu)}$, and investigate their response to strain, $\Delta\Gamma^{(\nu)}$. Fig. 2.5(e)–(h) present these calculations, highlighting a significant reduction in scattering rates for the LF modes by 1 to over 5 ps^{-1} , contrasting with the inconsistent and minimal changes in the ES-mode scattering rates. This can be understood by considering the forces governing the modes: LF phonons are mostly intermolecular and long-range intramolecular, which are regulated by weaker van der Waals forces. This makes LF phonons more susceptible to strains than ES phonons, which are mostly short-range intramolecular and are controlled by strong covalent bonds. Further analysis suggests that the decrease in LF-mode scattering rates due to the compressive strain is a result of reductions in both e -ph coupling and scattering phase space, as detailed in the SM (Sec. 2.5).

While compressive strain decreases LF-mode scattering rates and enhances charge carrier mobility, tensile strain is expected to have the opposite effect. This is confirmed by our calculations for anthracene under a 2.5% homogeneous tensile strain, which, as detailed in SM (Sec. 2.5), increases LF-mode scattering rates and decreases mobility. Our analysis assumes that a 2.5% homogeneous strain is moderate such that the charge transport remains in the bandlike regime. Too strong of a strain could cause severe deformation of electronic band structure and carrier trapping [64], which may alter the transport regime and require a different transport model for a more accurate description. Nonetheless, our findings support that strain engineering is an effective method to modulate bandlike charge carrier mobility in OMCs, due to the distinct sensitivity of LF phonons—which govern bandlike transport—to applied strain.

2.4 Conclusions

In summary, our first-principles BTE calculations, which incorporate all phonon modes on an equal footing, provide a comprehensive analysis of bandlike charge

transport in OMCs. Our computed charge carrier mobilities for multiple OMCs are in very good agreement with experiments between 100–400 K. We determined that low-frequency (LF) phonons, those below 150 cm^{-1} and characterized by mainly intermolecular and some long-range intramolecular vibrations, are the dominant contributors to the e -ph scattering that limits bandlike mobility. Additionally, we found that LF-phonon scattering rates are especially sensitive to strain, underscoring the potential of strain engineering to optimize charge transport in OMCs. Our study demonstrates the efficacy, predictability, and explanatory strength of first-principles BTE calculations. Future work includes extending these calculations to a broader range of OMCs, potentially in a high-throughput manner, and integrate the results with machine learning techniques [65] to expedite the discovery of design principles for high-performance organic electronics.

2.5 Supplementary materials

Computational details

	Benzene	Anthracene	Tetracene	Pentacene	Biphenyl
chem. formula	C_6H_6	$\text{C}_{14}\text{H}_{10}$	$\text{C}_{18}\text{H}_{12}$	$\text{C}_{22}\text{H}_{14}$	$\text{C}_{12}\text{H}_{10}$
space group	Pbca	$\text{P2}_1\text{a}$	$\text{P}\bar{1}$	$\text{P}\bar{1}$	$\text{P2}_1\text{a}$
#atom/cell	48	48	60	72	44
atomic pos.	[66]	[67]	[68]	[69]	[70]
lattice params.	[71] (103 K)	[67] (94 K)	[68]	[69]	[54]
studied carrier	e	h	h	h	e
k -grid (scf)	$3\times 2\times 3$	$2\times 4\times 2$	$2\times 4\times 2$	$2\times 2\times 2$	$2\times 4\times 2$
k -grid (nscf)	$3\times 2\times 3$	$4\times 4\times 4$	$4\times 4\times 4$	$4\times 4\times 4$	$4\times 4\times 4$
#wannier band	8	2	2	2	4
q -grid	$3\times 2\times 3$	$2\times 4\times 2$	$2\times 4\times 2$	$2\times 2\times 2$	$2\times 4\times 2$
k -grid (BTE)	50^3	60^3	60^3	50^3	50^3

Table 2.1: Crystallographic properties and numerical settings used in the calculations. scf and nscf refer to self-consistent calculations and non-self-consistent calculations, respectively.

Phonon dispersion and intramolecular characteristics

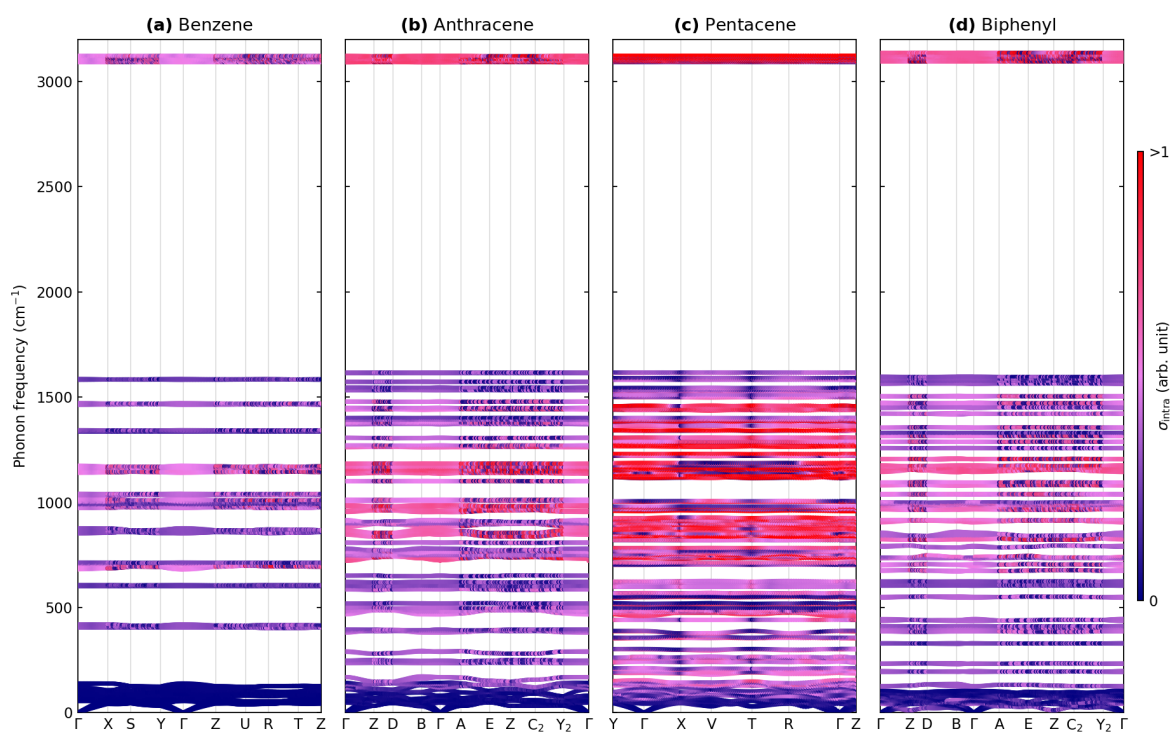


Figure 2.6: Phonon dispersions of (a) benzene, (b) anthracene, (c) pentacene, and (d) biphenyl. The color gradient from blue to red indicates increasing intramolecular character (σ_{intra} in Eq. 2.6).

Strained electronic structure and phonon dispersion

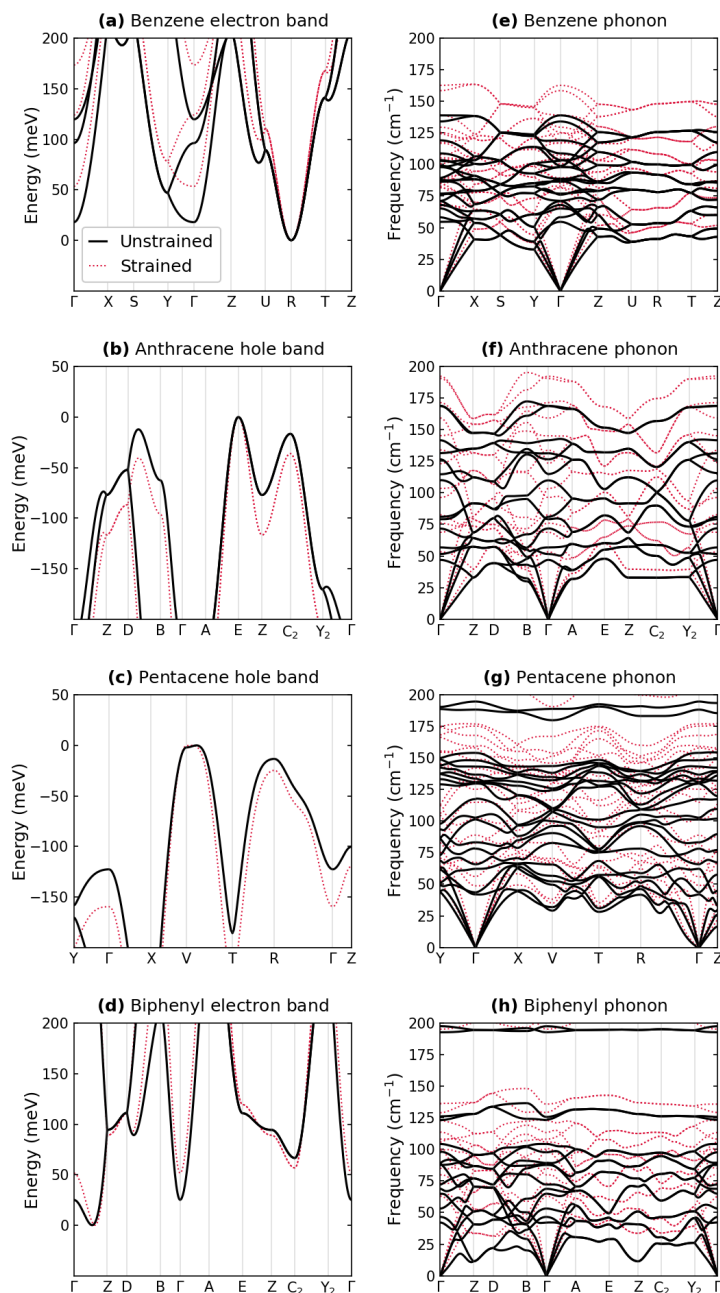


Figure 2.7: Left column: Electronic band structures of (a) benzene electron, (b) anthracene hole, (c) pentacene hole, and (d) biphenyl electron, with energy zero at the conduction band minimum for electrons and valence band maximum for holes. Right column: Phonon dispersions of (e) benzene, (f) anthracene, (g) pentacene, and (h) biphenyl. The black solid lines represent the original data, and the red dashed lines represent 2.5% compressively strained data.

Anthracene under tensile strain

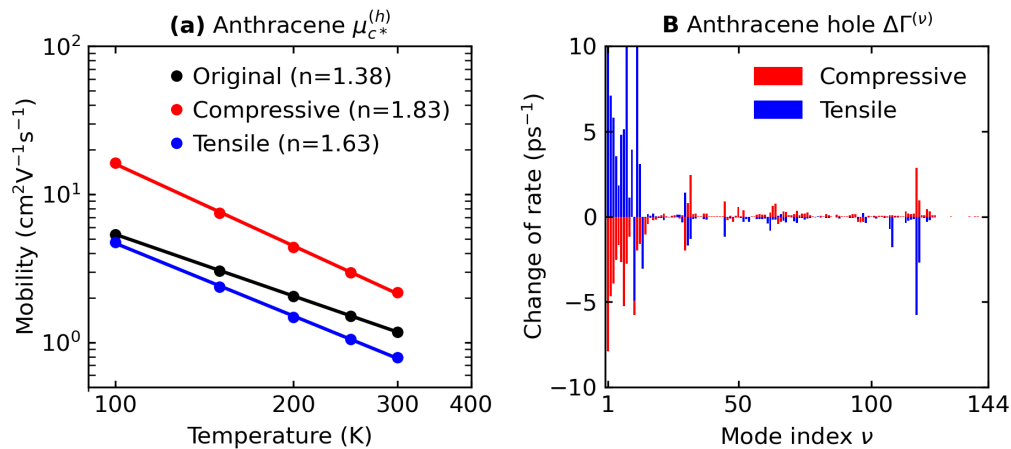


Figure 2.8: (a) Hole mobility of anthracene in the c^* -direction. Red: mobility under 2.5% compressive strain. Blue: mobility under 2.5% tensile strain. Black: original mobility. The exponent of the power-law temperature dependence T^{-n} is indicated for each mobility. (b) Change in the average mode-resolved electron-phonon scattering rates of anthracene due to 2.5% homogeneous compressive (red) and tensile (blue) strain.

Electron-phonon coupling and scattering phase space

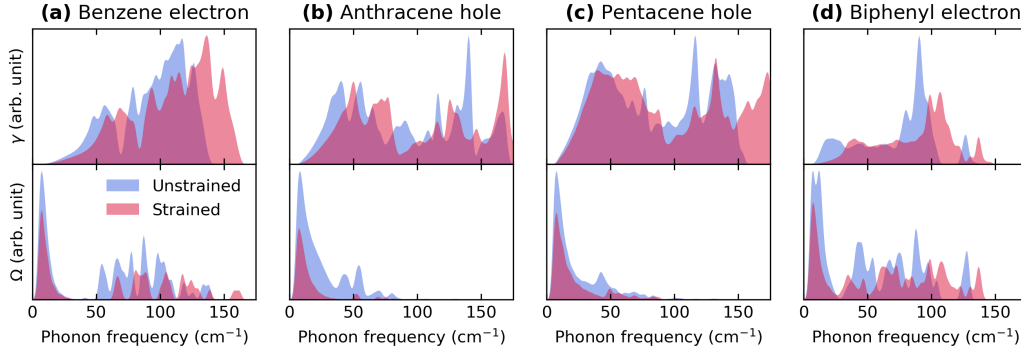


Figure 2.9: Distribution functions of electron-phonon coupling (γ , Eq. 2.8, upper panels) and scattering phase space (Ω , Eq. 2.12, lower panels) for the LE phonons at the electron band edge of (a) benzene electron, (b) anthracene hole, (c) pentacene hole, and (d) biphenyl electron. Blue and red fillings indicate the original and 2.5% compressively strained data, respectively.

We rewrite the e -ph scattering rate defined in Eqs. 2.2 and 2.3 as

$$\Gamma_{n\mathbf{k}}(T) = \frac{2\pi}{\hbar} \sum_{m\nu\mathbf{q}} |g_{m\nu\nu}(\mathbf{k}, \mathbf{q})|^2 \xi_{m\nu\nu}(\mathbf{k}, \mathbf{q}), \quad (2.10)$$

where we have defined the scattering phase space factor

$$\xi_{m\nu\nu}(\mathbf{k}, \mathbf{q}) = (N_{\nu\mathbf{q}} + 1 - f_{m\mathbf{k}+\mathbf{q}}) \delta(\varepsilon_{n\mathbf{k}} - \varepsilon_{n\mathbf{k}+\mathbf{q}} - \omega_{\nu\mathbf{q}}) + (N_{\nu\mathbf{q}} + f_{m\mathbf{k}+\mathbf{q}}) \delta(\varepsilon_{n\mathbf{k}} - \varepsilon_{n\mathbf{k}+\mathbf{q}} + \omega_{\nu\mathbf{q}}). \quad (2.11)$$

To isolate e -ph coupling's contribution to scattering rate, in Eq. 2.8 we have defined the coupling distribution function. Similarly, here we isolate the phase space contribution to scattering rate by defining the phase space distribution function that sums over the phase space factor:

$$\Omega_{n\mathbf{k}}(\omega) = \sum_{m\nu\mathbf{q}} \xi_{m\nu\nu}(\mathbf{k}, \mathbf{q}) \delta(\omega - \omega_{\nu\mathbf{q}}). \quad (2.12)$$

The calculated coupling and phase space distribution functions for the LF modes in the systems, both unstrained and under 2.5% homogeneous compressive strain, are shown in Fig. 2.9. Strain alters the distributions, shifting peaks along the phonon frequency axis due to the stretching of phonon dispersions shown in Fig. 2.7(e)–(h). Under the strain, benzene's coupling distribution peaks maintain their heights, whereas the highest coupling distribution peak is reduced for the other three systems. A reduction is observed in the highest peak (between phonon frequencies of 0 and 25

cm^{-1}) of phase space distribution for all systems under the strain. These indicate that the compressive strain generally reduces the scattering contributions from both e -ph coupling and phase space.

References

- [1] A. F. Paterson, S. Singh, K. J. Fallon, T. Hodsdon, Y. Han, B. C. Schroeder, H. Bronstein, M. Heeney, I. McCulloch, and T. D. Anthopoulos, *Adv. Mater.* **30**, 1801079 (2018).
- [2] S. Fratini, M. Nikolka, A. Salleo, G. Schweicher, and H. Sirringhaus, *Nat. Mater.* **19**, 491–502 (2020).
- [3] H. Oberhofer, K. Reuter, and J. Blumberger, *Chem. Rev.* **117**, 10319–10357 (2017).
- [4] W. Li, J. Ren, and Z. Shuai, *Nat. Commun.* **12**, 4260 (2021).
- [5] S. Giannini and J. Blumberger, *Acc. Chem. Res.* **55**, 819–830 (2022).
- [6] B. K. Chang, J.-J. Zhou, N.-E. Lee, and M. Bernardi, *npj Comput. Mater.* **8**, 63 (2022).
- [7] T. Nematiram, D. Padula, A. Landi, and A. Troisi, *Adv. Funct. Mater.* 2001906 (2020).
- [8] T. Nematiram and A. Troisi, *J. Chem. Phys.* **152**, 190902 (2020).
- [9] V. Coropceanu, J. Cornil, D. A. Da Silva Filho, Y. Olivier, R. Silbey, and J.-L. Brédas, *Chem. Rev.* **107**, 926–952 (2007).
- [10] J. Ziman, *Electrons and phonons: The theory of transport phenomena in solids* (Oxford University Press, Oxford, 2001).
- [11] G. D. Mahan, *Many-Particle Physics* (Springer US, New York, 2000).
- [12] S. Fratini, D. Mayou, and S. Ciuchi, *Adv. Funct. Mater.* **26**, 2292–2315 (2016).
- [13] S. Hutsch, M. Panhans, and F. Ortmann, *npj Comput. Mater.* **8**, 228 (2022).
- [14] J. H. Fetherolf, D. Golež, and T. C. Berkelbach, *Phys. Rev. X* **10**, 021062 (2020).
- [15] A. Landi, A. Peluso, and A. Troisi, *Adv. Mater.* 2008049 (2021).
- [16] N.-E. Lee, J.-J. Zhou, L. A. Agapito, and M. Bernardi, *Phys. Rev. B* **97**, 115203 (2018).
- [17] J. Xi, M. Long, L. Tang, D. Wang, and Z. Shuai, *Nanoscale* **4**, 4348 (2012).
- [18] F. Brown-Altwater, G. Antonius, T. Rangel, M. Giantomassi, C. Draxl, X. Gonze, S. G. Louie, and J. B. Neaton, *Phys. Rev. B* **101**, 165102 (2020).
- [19] G. Cohen, J. B. Haber, J. B. Neaton, D. Y. Qiu, and S. Refaely-Abramson, *arXiv:2305.04223* (2023).

- [20] C. Dimitrakopoulos and P. Malenfant, *Adv. Mater.* **14**, 99–117 (2002).
- [21] T. Sakanoue and H. Sirringhaus, *Nat. Mater.* **9**, 736–740 (2010).
- [22] D. Ji, T. Li, J. Liu, S. Amirjalayer, M. Zhong, Z.-Y. Zhang, X. Huang, Z. Wei, H. Dong, W. Hu, and H. Fuchs, *Nat. Commun.* **10**, 12 (2019).
- [23] Y. C. Cheng, R. J. Silbey, D. A. da Silva Filho, J. P. Calbert, J. Cornil, and J. L. Brédas, *J. Chem. Phys.* **118**, 3764–3774 (2003).
- [24] Z. J. Knepp, G. B. Masso, and L. A. Fredin, *J. Chem. Phys.* **158**, 064704 (2023).
- [25] T.-H. Liu, J. Zhou, B. Liao, D. J. Singh, and G. Chen, *Phys. Rev. B* **95**, 075206 (2017).
- [26] M. Bernardi, *Eur. Phys. J. B* **89**, 239 (2016).
- [27] W. Li, *Phys. Rev. B* **92**, 075405 (2015).
- [28] J. I. Mustafa, M. Bernardi, J. B. Neaton, and S. G. Louie, *Phys. Rev. B* **94**, 155105 (2016).
- [29] T. Kubo, R. Häusermann, J. Tsurumi, J. Soeda, Y. Okada, Y. Yamashita, N. Akamatsu, A. Shishido, C. Mitsui, T. Okamoto, S. Yanagisawa, H. Matsui, and J. Takeya, *Nat. Commun.* **7**, 11156 (2016).
- [30] H. H. Choi, H. T. Yi, J. Tsurumi, J. J. Kim, A. L. Briseno, S. Watanabe, J. Takeya, K. Cho, and V. Podzorov, *Adv. Sci.* **7**, 1901824 (2020).
- [31] Y. Wu, A. R. Chew, G. A. Rojas, G. Sini, G. Haugstad, A. Belianinov, S. V. Kalinin, H. Li, C. Risko, J.-L. Brédas, A. Salleo, and C. D. Frisbie, *Nat. Commun.* **7**, 10270 (2016).
- [32] B. Jun, C. H. Lee, and S. U. Lee, *J. Ind. Eng. Chem.* **107**, 137–144 (2022).
- [33] P. Giannozzi, S. Baroni, N. Bonini, M. Calandra, R. Car, C. Cavazzoni, D. Ceresoli, G. L. Chiarotti, M. Cococcioni, I. Dabo, A. Dal Corso, S. de Gironcoli, S. Fabris, G. Fratesi, R. Gebauer, U. Gerstmann, C. Gougoussis, A. Kokalj, M. Lazzeri, L. Martin-Samos, N. Marzari, F. Mauri, R. Mazzarello, S. Paolini, A. Pasquarello, L. Paulatto, C. Sbraccia, S. Scandolo, G. Sclauzero, A. P. Seitsonen, A. Smogunov, P. Umari, and R. M. Wentzcovitch, *J. Phys. Condens. Matter* **21**, 395502 (2009).
- [34] P. Giannozzi, O. Andreussi, T. Brumme, O. Bunau, M. Buongiorno Nardelli, M. Calandra, R. Car, C. Cavazzoni, D. Ceresoli, M. Cococcioni, N. Colonna, I. Carnimeo, A. Dal Corso, S. de Gironcoli, P. Delugas, R. A. DiStasio, A. Ferretti, A. Floris, G. Fratesi, G. Fugallo, R. Gebauer, U. Gerstmann, F. Giustino, T. Gorni, J. Jia, M. Kawamura, H.-Y. Ko, A. Kokalj, E. Küçükbenli, M. Lazzeri, M. Marsili, N. Marzari, F. Mauri, N. L. Nguyen, H.-V. Nguyen, A. Otero-de-la-Roza, L. Paulatto, S. Poncé, D. Rocca, R. Sabatini, B. Santra, M. Schlipf, A. P. Seitsonen, A. Smogunov, I. Timrov, T. Thonhauser, P. Umari, N. Vast, X. Wu, and S. Baroni, *J. Phys. Condens. Matter* **29**, 465901 (2017).

- [35] J. P. Perdew, K. Burke, and M. Ernzerhof, *Phys. Rev. Lett.* **77**, 3865–3868 (1996).
- [36] N. Troullier and J. L. Martins, *Phys. Rev. B* **43**, 1993–2006 (1991).
- [37] M. van Setten, M. Giantomassi, E. Bousquet, M. Verstraete, D. Hamann, X. Gonze, and G.-M. Rignanese, *Comput. Phys. Commun.* **226**, 39–54 (2018).
- [38] S. Grimme, *J. Comput. Chem.* **27**, 1787–1799 (2006).
- [39] V. Barone, M. Casarin, D. Forrer, M. Pavone, M. Sambri, and A. Vittadini, *J. Comput. Chem.* **30**, 934–939 (2009).
- [40] A. A. Mostofi, J. R. Yates, Y.-S. Lee, I. Souza, D. Vanderbilt, and N. Marzari, *Comput. Phys. Commun.* **178**, 685–699 (2008).
- [41] G. Pizzi, V. Vitale, R. Arita, S. Blügel, F. Freimuth, G. Géranton, M. Gibertini, D. Gresch, C. Johnson, T. Koretsune, J. Ibañez-Azpiroz, H. Lee, J.-M. Lihm, D. Marchand, A. Marrazzo, Y. Mokrousov, J. I. Mustafa, Y. Nohara, Y. Nomura, L. Paulatto, S. Poncé, T. Ponweiser, J. Qiao, F. Thöle, S. S. Tsirkin, M. Wierzbowska, N. Marzari, D. Vanderbilt, I. Souza, A. A. Mostofi, and J. R. Yates, *J. Phys. Condens. Matter* **32**, 165902 (2020).
- [42] S. Baroni, S. de Gironcoli, A. Dal Corso, and P. Giannozzi, *Rev. Mod. Phys.* **73**, 515–562 (2001).
- [43] N. Shulumba, O. Hellman, and A. J. Minnich, *Phys. Rev. Lett.* **119**, 185901 (2017).
- [44] J.-J. Zhou, J. Park, I.-T. Lu, I. Maliyov, X. Tong, and M. Bernardi, *Comput. Phys. Commun.* **264**, 107970 (2021).
- [45] M. Lehnhardt, S. Hamwi, M. Hopping, J. Reinker, T. Riedl, and W. Kowalsky, *Appl. Phys. Lett.* **96**, 193301 (2010).
- [46] O. Madelung, U. Rössler, and M. Schulz, eds., *Benzene, C₆H₆ charge carrier mobilities and generation processes: Datasheet from Landolt-Börnstein - Group III Condensed Matter · Volume 41E: "Ternary Compounds, Organic Semiconductors" in SpringerMaterials* (Springer-Verlag Berlin Heidelberg, 2000).
- [47] O. Madelung, U. Rössler, and M. Schulz, eds., *Naphthalene, C₁₀H₈ charge carrier mobilities: Datasheet from Landolt-Börnstein - Group III Condensed Matter · Volume 41E: "Ternary Compounds, Organic Semiconductors" in SpringerMaterials* (Springer-Verlag Berlin Heidelberg, 2000).
- [48] O. Madelung, U. Rössler, and M. Schulz, eds., *Anthracene, C₁₄H₁₀ charge carrier mobilities: Datasheet from Landolt-Börnstein - Group III Condensed Matter · Volume 41E: "Ternary Compounds, Organic Semiconductors" in SpringerMaterials* (Springer-Verlag Berlin Heidelberg, 2000).

- [49] O. Madelung, U. Rössler, and M. Schulz, eds., *Tetracene, C₁₈H₁₂ vibrons, polarization energies, hole mobilities, luminescence: Datasheet from Landolt-Börnstein - Group III Condensed Matter · Volume 41E: "Ternary Compounds, Organic Semiconductors" in SpringerMaterials* (Springer-Verlag Berlin Heidelberg, 2000).
- [50] R. W. I. de Boer, M. Jochemsen, T. M. Klapwijk, A. F. Morpurgo, J. Niemax, A. K. Tripathi, and J. Pflaum, *J. Appl. Phys.* **95**, 1196–1202 (2004).
- [51] O. D. Jurchescu, J. Baas, and T. T. M. Palstra, *Appl. Phys. Lett.* **84**, 3061–3063 (2004).
- [52] T. Minari, T. Nemoto, and S. Isoda, *J. Appl. Phys.* **99**, 034506 (2006).
- [53] J. Y. Lee, S. Roth, and Y. W. Park, *Appl. Phys. Lett.* **88**, 252106 (2006).
- [54] O. Madelung, U. Rössler, and M. Schulz, eds., *Biphenyl, C₁₂H₁₀ charge carrier mobilities: Datasheet from Landolt-Börnstein - Group III Condensed Matter · Volume 41E: "Ternary Compounds, Organic Semiconductors" in SpringerMaterials* (Springer-Verlag Berlin Heidelberg, 2000).
- [55] O. Ostroverkhova, D. G. Cooke, F. A. Hegmann, J. E. Anthony, V. Podzorov, M. E. Gershenson, O. D. Jurchescu, and T. T. M. Palstra, *Appl. Phys. Lett.* **88**, 162101 (2006).
- [56] D. Moses, C. Soci, X. Chi, and A. P. Ramirez, *Phys. Rev. Lett.* **97**, 067401 (2006).
- [57] W. Setyawan and S. Curtarolo, *Comput. Mater. Sci.* **49**, 299–312 (2010).
- [58] T. Kamencek and E. Zojer, *J. Mater. Chem. C* **10**, 2532–2543 (2022).
- [59] H. Tamura, M. Tsukada, H. Ishii, N. Kobayashi, and K. Hirose, *Phys. Rev. B* **86**, 035208 (2012).
- [60] F. Zhang, H.-W. Wang, K. Tominaga, and M. Hayashi, *Wiley Interdiscip. Rev. Comput. Mol. Sci.* **6**, 386–409 (2016).
- [61] E. A. Coutsiyas, C. Seok, and K. A. Dill, *J. Comput. Chem.* **25**, 1849–1857 (2004).
- [62] W. Kabsch, *Acta Crystallogr. A* **32**, 922–923 (1976).
- [63] W. Kabsch, *Acta Crystallogr. A* **34**, 827–828 (1978).
- [64] Y. Mei, P. J. Diemer, M. R. Niazi, R. K. Hallani, K. Jarolimek, C. S. Day, C. Risko, J. E. Anthony, A. Amassian, and O. D. Jurchescu, *Proc. Natl. Acad. Sci.* **114**, E6739–E6748 (2017).
- [65] C. Kunkel, J. T. Margraf, K. Chen, H. Oberhofer, and K. Reuter, *Nat. Commun.* **12**, 2422 (2021).
- [66] A. Katrusiak, M. Podsiadło, and A. Budzianowski, *Cryst. Growth Des.* **10**, 3461–3465 (2010).

- [67] C. P. Brock and J. D. Dunitz, *Acta Crystallogr. B* **46**, 795–806 (1990).
- [68] J. M. Robertson, V. C. Sinclair, and J. Trotter, *Acta Crystallogr.* **14**, 697–704 (1961).
- [69] C. C. Mattheus, A. B. Dros, J. Baas, A. Meetsma, J. L. d. Boer, and T. T. M. Palstra, *Acta Crystallogr. C* **57**, 939–941 (2001).
- [70] J. Trotter, *Acta Crystallogr.* **14**, 1135–1140 (1961).
- [71] E. G. Cox, D. W. J. Cruickshank, and J. A. S. Smith, *Proc. R. Soc. A: Math. Phys. Eng. Sci.* **247**, 1–21 (1958).

*Chapter 3*INTERMEDIATE POLARONIC CHARGE TRANSPORT
IN ORGANIC CRYSTALS

This chapter is a slightly modified version of the published article: B. K. Chang, J.-J. Zhou, N.-E. Lee, and M. Bernardi, “Intermediate polaronic charge transport in organic crystals from a many-body first-principles approach”, *npj Comput. Mater.* **8**, 63 (2022).

3.1 Introduction

Charge transport in organic molecular crystals (OMCs) is often classified into two limiting cases: the band transport and polaron hopping regimes, each entailing specific transport mechanisms [1]. In band transport, charge carriers are delocalized, the e -ph coupling is weak, and the mobility is correspondingly high ($> 10 \text{ cm}^2\text{V}^{-1}\text{s}^{-1}$) and characterized by a power-law decrease with temperature. Band transport in OMCs is usually governed by scattering of carriers with low-energy acoustic and intermolecular phonons, with the corresponding e -ph interactions often modeled by the Peierls Hamiltonian [2]. These weak e -ph interactions can be described with lowest-order perturbation theory, and the OMC mobility can be accurately predicted using the Boltzmann transport equation (BTE) [3, 4], including all phonon modes on the same footing.

In the polaron hopping regime, the charge carriers interact strongly with phonons, forming self-localized (small) polarons, which are often modeled with the Holstein Hamiltonian to describe intramolecular e -ph interactions [5]. The resulting charge transport is dominated by thermally activated polaron hopping and is often described with Marcus theory [6, 7]. The mobility in the polaron hopping regime is relatively small, usually below $0.1 \text{ cm}^2\text{V}^{-1}\text{s}^{-1}$, and is more challenging to predict from first principles.

Between these two limiting scenarios, OMCs also exhibit an *intermediate* transport regime, for which neither the band transport nor the polaron hopping pictures are fully adequate [1, 7]. In the intermediate regime, the mobility exhibits a bandlike power-law temperature dependence [7–9], yet polarons can be present and low mobility values ($< 1 \text{ cm}^2\text{V}^{-1}\text{s}^{-1}$) are common [1]. A signature of intermediate

transport is the violation of the Mott-Ioffe-Regel limit [10], whereby the carrier mean-free-paths become smaller than the intermolecular distance [7], making the BTE description inadequate.

Various approaches have been employed to study intermediate transport in OMCs; they typically employ a Holstein Hamiltonian or a (Peierls-type) dynamical disorder Hamiltonian, or a combination of both, and obtain the mobility via linear-response theory [11–14], diffusion simulation [15, 16], surface hopping method [17], or transient localization calculation [18, 19]. These methods are highly valuable for studies of OMCs, although they usually rely on simplifying assumptions such as including only specific phonon modes and e -ph interactions, or fitting model parameters to experiments. To date, first-principles approaches to predict charge transport in the intermediate regime with quantitative accuracy are scarce, especially within rigorous treatments based on many-body perturbation theory.

In this work, we develop rigorous calculations of the mobility in the intermediate charge transport regime in OMCs. Focusing on naphthalene crystal as a case study, we employ a finite-temperature cumulant approach [8] to capture the strong e -ph interactions and polaron effects of the intermediate regime, and employ Green-Kubo theory to compute the electron mobility. All phonon modes are included and treated on equal footing.

This cumulant plus Kubo (CK) approach is shown to predict the electron mobility in the intermediate regime with a high accuracy, within a factor of two of experiment between 100–300 K for crystallographic directions parallel to the naphthalene molecular planes. We additionally show the failure of the BTE to describe the mobility in the intermediate regime. Our analysis of the electronic spectral functions reveals the presence of a broad satellite next to the quasiparticle (QP) peak, explaining the breakdown of the BTE and the band transport picture. The broadening of the QP peak is mainly due to coupling with low-energy intermolecular phonons, while the polaron satellite peaks are due to strong coupling with intramolecular phonons. Therefore, the intermolecular modes are directly responsible for scattering the electrons and limiting the mobility, whereas the intramolecular modes limit the mobility indirectly, by transferring spectral weight from the QP peak to the polaron satellites. For charge transport normal to the molecular planes, we find that both the BTE and CK approaches cannot correctly predict the mobility, which experimentally is nearly temperature independent and governed by small-polaron hopping [20–22]. This finding restricts the applicability of the CK method to intermediate e -ph

coupling strengths.

Taken together, our work provides an accurate first-principles method to study polaron transport in OMCs, and unravels the interplay of low- and high-energy phonon modes in the intermediate regime. Our results provide a blueprint for studying charge transport in a wide range of organic crystals.

3.2 Results

Computational approach

We compute the ground state electronic structure of naphthalene crystal using plane-wave density functional theory (DFT) calculations with the QUANTUM ESPRESSO code [23, 24]. We employ the generalized gradient approximation [25] and norm-conserving pseudopotentials [26] from Pseudo Dojo [27]. The DFT band structure is refined using GW calculations (with the YAMBO code [28, 29]) to better capture dynamical screening effects. Maximally localized Wannier functions [30] are generated with the WANNIER90 code [31] following a procedure similar to Ref. [3]. We compute the e -ph interactions and charge transport separately at four temperatures (100, 160, 220, and 300 K), using different experimental lattice parameters at each temperature [32] and relaxing the atomic positions with DFT. We obtain the lattice dynamics and e -ph perturbation potentials from density functional perturbation theory (DFPT) [33], and compute the e -ph interactions with the PERTURBO code [34]. Additional numerical details are provided in the Methods section.

Using the computed e -ph interactions, we study charge transport in the BTE and CK frameworks with the PERTURBO code [34]. In the BTE, the mobility tensor $\mu_{\alpha\beta}$ is computed in the relaxation time approximation (RTA):

$$\mu_{\alpha\beta}(T) = \frac{2e}{n_c V_{\text{uc}}} \int dE \left(-\frac{\partial f(E, T)}{\partial E} \right) \sum_{n\mathbf{k}} \tau_{n\mathbf{k}}(T) v_{n\mathbf{k}}^\alpha v_{n\mathbf{k}}^\beta \delta(E - \varepsilon_{n\mathbf{k}}), \quad (3.1)$$

where α and β are Cartesian directions parallel to the crystal principal axes, T is the temperature, e the electronic charge, n_c the carrier concentration, V_{uc} the unit cell volume, f the electronic Fermi-Dirac distribution and E is the electron energy. Here and below, n is the band index and \mathbf{k} the crystal momentum of the electronic states. The BTE mobility depends on the electron band energies $\varepsilon_{n\mathbf{k}}$, the corresponding band velocities $v_{n\mathbf{k}}$, and the state-dependent e -ph relaxation times $\tau_{n\mathbf{k}}$ obtained within lowest-order perturbation theory [34, 35]. As a sanity check, we compute the mobility at 220 K by solving the full linearized BTE with an iterative

approach (ITA) [34, 36], and find that in naphthalene it gives results identical to the RTA, justifying our use of the RTA.

To properly treat strong e -ph interactions and include polaron effects in the mobility, we employ a finite-temperature cumulant approach in which the retarded electron Green's function $G_{n\mathbf{k}}^R$ is written using the exponential ansatz [8, 37–41]

$$G_{n\mathbf{k}}^R(t, T) = G_{n\mathbf{k}}^{R,0}(t) e^{C_{n\mathbf{k}}(t, T)}, \quad (3.2)$$

where $G_{n\mathbf{k}}^{R,0}$ is the non-interacting Green's function and $C_{n\mathbf{k}}$ is the cumulant function, obtained here at finite temperatures from the lowest-order e -ph self-energy (see Methods). The electron spectral function is obtained from the Green's function at each electron energy E using

$$A_{n\mathbf{k}}(E, T) = -\text{Im}G_{n\mathbf{k}}^R(E, T)/\pi. \quad (3.3)$$

In the CK method, the mobility tensor is computed directly from the spectral function using the linear-response Green-Kubo formula [8, 38, 42]:

$$\mu_{\alpha\beta}(T) = \frac{1}{n_c e} \int dE \Phi_{\alpha\beta}(E, T), \quad (3.4)$$

where the integrand is the transport distribution function (TDF). Under the approximation of neglecting vertex corrections, the TDF reads [42]

$$\Phi_{\alpha\beta}(E, T) = \frac{\pi \hbar e^2}{V_{\text{uc}}} \sum_{n\mathbf{k}} v_{n\mathbf{k}}^\alpha v_{n\mathbf{k}}^\beta |A_{n\mathbf{k}}(E, T)|^2 \left(-\frac{\partial f(E, T)}{\partial E} \right), \quad (3.5)$$

where $v_{n\mathbf{k}}$ are the unperturbed electron band velocities, the same as those used in Eq. (3.1) [42]. The CK mobility defined in Eq. (3.4) is obtained from the cumulant spectral function, therefore it takes into account the strong e -ph coupling and polaron effects. The CK calculations have been shown to provide results in close agreement with the BTE-RTA in the limit of weak e -ph interactions (see Ref. [8] for a calculation on GaAs).

Electron mobility

The crystal structure of naphthalene consists of molecular planes in the a and b crystallographic directions, stacked along the plane-normal c^* direction [Fig. 3.1(a)]. We first discuss charge transport in the molecular planes. For hole carriers, we have previously shown that such in-plane transport is bandlike and well described by

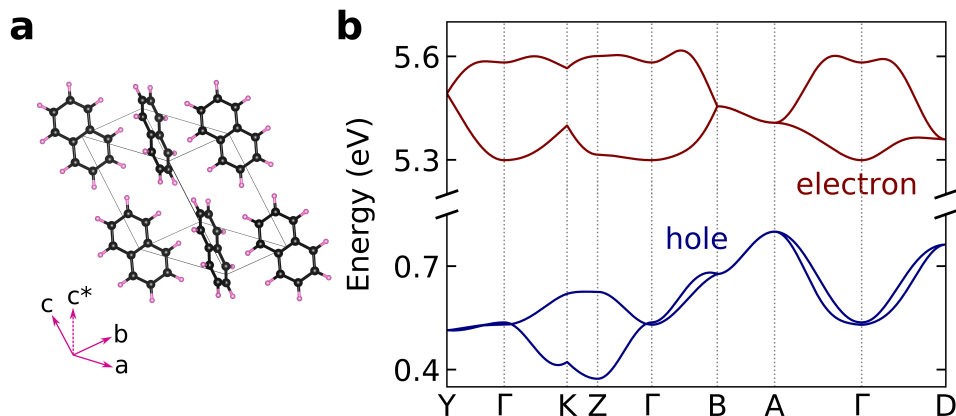


Figure 3.1: (a) Monoclinic crystal structure of naphthalene, with molecular a - b planes stacked in the plane-normal c^* direction. (b) Band structure of naphthalene, showing the two lowest-energy electron (LUMO and LUMO+1) and hole (HOMO and HOMO-1) bands.

the BTE [3]. In this work, we focus on the mobility of the *electron* carriers, which due to their flatter electronic bands with greater effective masses compared to holes [Fig. 3.1(b)] are expected to exhibit lower mobilities and a range of transport regimes. Only the electronic bands formed by the lowest unoccupied molecular orbital (LUMO) and the next-higher-energy orbital (LUMO+1) contribute to electron transport in the 100–300 K temperature range studied here, so we consider only these two bands in our mobility calculations.

Figure 3.2 shows the in-plane electron mobilities computed with the BTE and CK methods, and compares them with experimental data [20]. We fit each mobility curve with a T^{-n} power-law temperature trend and give the exponent n next to each curve. The results show that the BTE predicts a much stronger temperature dependence of the mobility than in experiment, with errors in the computed exponents for transport along the a and b crystallographic directions (mobilities μ_a and μ_b in Fig. 3.2, respectively) of over 100% for μ_a and 270% for μ_b relative to the exponent n obtained by fitting the experimental results. Due to this error, the BTE greatly overestimates the mobility at low temperatures – for example, μ_a at 100 K from the BTE is an order of magnitude greater than the experimental value.

These results are a strong evidence of the failure of the Boltzmann equation to describe electron transport in naphthalene; the physical origin of this failure is examined below. Note that the BTE failure is not a consequence of our use of the RTA, as the full solution of the BTE [34] gives results nearly identical to the RTA

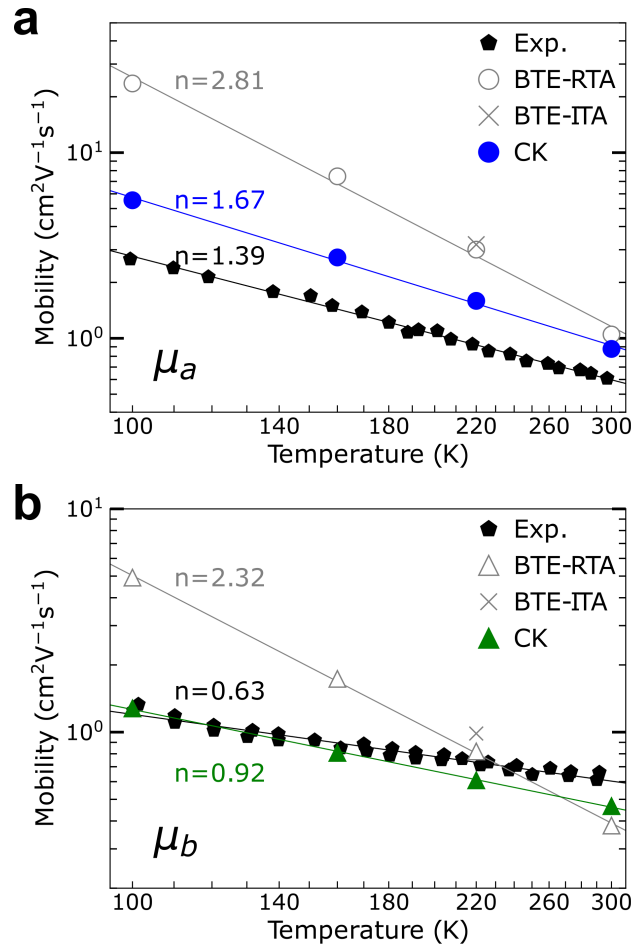


Figure 3.2: (a) Electron mobility in direction a . (b) Electron mobility in direction b . Results obtained from BTE and CK calculations are compared with experimental data from Ref. [20].

(see the ITA points at 220 K in Fig. 3.2). The fact that the mobility has a power-law temperature dependence but is not correctly predicted by the BTE is a hallmark of the intermediate transport regime [7, 9].

The CK calculations give significantly improved results (Fig. 3.2). The CK mobilities are within a factor of 2 of experiment for μ_a and 1.3 for μ_b in the entire 100–300 K temperature range. The error in the T^{-n} exponent is reduced to 20% for μ_a and 45% for μ_b relative to experiment, a five-fold improvement in accuracy over the BTE results. Achieving this level of accuracy for quantitative predictions of the mobility in OMCs has recently become possible in the band transport regime [3] but has so far remained challenging in the intermediate regime. As we discuss below, by combining the cumulant and Green-Kubo frameworks, our CK approach

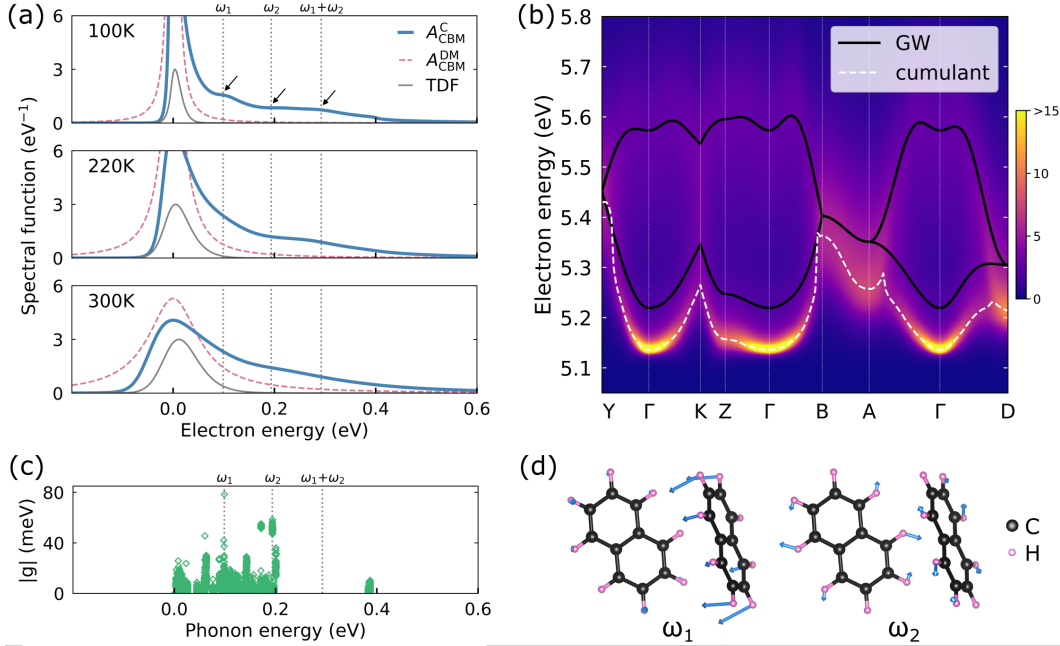


Figure 3.3: (a) Spectral functions computed at three temperatures for the CBM electronic state. Results from the cumulant approach ($A_{\text{CBM}}^{\text{C}}$) are compared to the Dyson-Migdal spectral function ($A_{\text{CBM}}^{\text{DM}}$). The QP peak is chosen as the zero of the energy axis for each spectral function. The transport distribution function (TDF) in arbitrary units is also shown at each temperature. (b) Electron spectral function for the LUMO and LUMO+1 bands along a high-symmetry path, computed at 100 K using the cumulant method. The solid line is the GW band structure and the dashed line shows the renormalized cumulant band structure obtained by connecting the QP peaks of the spectral functions. (c) Gauge-invariant e -ph coupling strength as a function of phonon energy. The energies ω_1 and ω_2 of the two phonon modes with strongest e -ph coupling are shown with vertical dashed lines. (d) Atomic displacements for the two intramolecular modes with the strongest e -ph coupling.

can capture key polaron effects in the intermediate regime such as higher-order e -ph coupling and spectral weight transfer, resulting in improved mobility predictions.

Electron spectral function

The electron spectral function is central to understanding polaron effects [8] and intermediate charge transport. The spectral function can be viewed as the density of states of a single electronic state, and it integrates to one over energy due to a well-known sum rule [38]. In Fig. 3.3(a), we show the spectral function at three temperatures, using results obtained with our cumulant method for the electronic state at the conduction band minimum (CBM) [Γ point in Fig. 3.1(b)]. At 100 K, next to the main QP peak we find a broad spectral feature associated with the

combined excitation of an electron QP plus one or two phonons. This broad satellite combines contributions from multiple satellite peaks, as shown by the arrows in Fig. 3.3(a), and is a signature of polaron formation [8]. At higher temperatures, the QP and satellite peaks broaden and ultimately merge into a continuum at 300 K. The coexistence of a well-formed QP peak and broad satellites shows that large-polaron effects, characteristic of e -ph interactions with intermediate strength, are a key characteristic of the intermediate transport regime.

The cumulant spectral functions for multiple electronic states in the LUMO and LUMO+1 bands can be combined to obtain a polaron band structure renormalized by the e -ph interactions. Figure 3.3(b) compares the band structures at 100 K computed with the GW method and with our cumulant calculations that use the GW band structure as input. The cumulant band structure, obtained by connecting the QP peaks of the cumulant spectral functions at neighboring \mathbf{k} -points, captures polaron effects such as QP mass and weight renormalization.

At 100 K, where the QP peaks are well-defined, we calculate the renormalized effective masses from the cumulant band structure, and find a moderate effective mass enhancement of 15–35% compared to the effective masses in the GW band structure in the in-plane directions. This shows that the cumulant approach can capture the bandwidth-narrowing due to strong e -ph interactions and polaron effects in OMCs [43].

The physical origin of the polaron satellite in Fig. 3.3(a) is of key importance. In the prototypical case of a polar inorganic material with strong e -ph coupling with longitudinal optical (LO) phonons, the satellite peaks are located at the LO-mode energy ω_{LO} (and its multiples) relative to the QP peak [8, 44]. Here, due to the presence of a large number of phonon modes in OMCs (108 in naphthalene), the satellites merge into a broad spectral feature resembling a long tail of the QP peak, with contributions from various phonon modes. To explain the origin of this broad satellite, in Fig. 3.3(c) we analyze the e -ph coupling strength for an electronic state near the CBM, as quantified by the absolute value of the gauge-invariant e -ph coupling, $|g|$ (see Methods).

In naphthalene, the 12 lowest-energy phonon modes are intermolecular, and the remaining 96 modes are intramolecular vibrations [3]. In Fig. 3.3(a), the mode with the strongest e -ph coupling, an intramolecular phonon with energy $\omega_1 \approx 0.1$ eV, generates a satellite peak in the spectral function at energy ω_1 relative to the QP peak. The intramolecular phonon with the second strongest e -ph coupling, with

energy $\omega_2 \approx 0.2$ eV, gives a second contribution to the broad satellite, followed by a plateau at higher energy. Finally, the inflection point in the spectral function at energy $\omega_1 + \omega_2$ is due to higher-order e -ph coupling from the two modes with energies ω_1 and ω_2 .

The atomic displacements associated with these two intramolecular modes are shown in Fig. 3.3(d). Both modes involve vibrations of the hydrogen atoms, in one case in the carbon ring plane and in the other case normal to the carbon rings. Our analysis demonstrates that these intramolecular phonons are responsible for the formation of polarons in naphthalene. This strong coupling with intramolecular phonons and the associated satellite peak in the spectral function are consistent with recent results from the Holstein-Peierls model [13].

Interestingly, lowest-order theory is wholly inadequate to describe this polaronic regime with intermediate e -ph coupling strength. To show this point, we compute the Dyson-Migdal (DM) spectral function [see Eq. (3.11)], which is obtained from the lowest-order e -ph self-energy and therefore does not include polaron effects. From the comparison of the cumulant and DM spectral functions in Fig. 3.3(a) it is clear that the DM spectral functions have a Lorentzian shape and lack any satellite structure. As a result, the subtle interplay between inter- and intramolecular phonons in the QP and satellite peaks cannot be captured in lowest-order theory. As we discuss below, this is the origin of the failure of the BTE to describe transport in the intermediate regime.

Failure of the Boltzmann equation

It is important to understand the microscopic origin of the failure of the BTE, and the success of the CK method, to describe transport in the intermediate regime. In the Green-Kubo framework, the mobility is given by an integral over electron energies [see Eq. (3.4)], which in principle combines contributions from all features of the spectral function. To quantify the contributions of the QP and satellite peaks to charge transport, we analyze the mobility integrand, the TDF in Eq. (3.5), and plot it together with the spectral functions in Fig. 3.3(a). We find that the TDF decays rapidly outside the QP peak, within an energy ω_1 of the QP peak at low temperature and ω_2 at 300 K. Therefore any spectral function feature with energy greater than ω_2 does not overlap with the TDF and cannot contribute to charge transport between 100–300 K. In this temperature range, although the mobility is mainly governed by the QP peak, polaron effects still contribute in important ways.

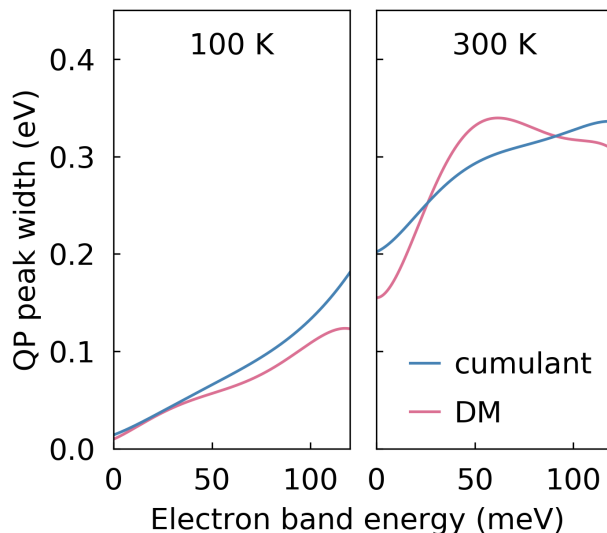


Figure 3.4: Full width at half maximum of the QP peak shown at two temperatures for both the cumulant and DM spectral functions. The energy zero is set to the conduction band minimum.

First, due to higher-order e -ph coupling with both inter- and intramolecular phonons, the linewidth of the QP peak in the cumulant spectral function is different than in the DM spectral function from lowest-order theory (see Fig. 3.4), whose linewidth is the scattering rate entering the BTE mobility calculation. This QP linewidth discrepancy is temperature and energy dependent (Fig. 3.4), which explains why the BTE cannot correctly predict the value and temperature dependence of the mobility in the intermediate regime, corroborating our results in Fig. 3.2. Second, the broad satellite in the cumulant spectral function limits the carrier mobility indirectly, by transferring spectral weight away from the QP peak (recall that the spectral function integrates to one over energy). The satellite peak at ω_1 contributes directly to transport only above ~ 200 K, where the QP peak broadens, merging with the satellite and overlapping with the TDF.

The picture that emerges is that electron transport in the naphthalene molecular planes is mainly governed by the scattering of QPs with renormalized weight, which couple directly (via the main QP peak) with low-energy intermolecular phonons and indirectly (via weight transfer to the satellites) with higher-energy intramolecular phonons. The latter can also contribute directly to charge transport as the temperatures increases above 200 K. The ability of our CK approach to address these subtle e -ph interactions enables accurate predictions of the mobility and its temperature dependence in the intermediate regime, where the BTE with lowest-order e -ph

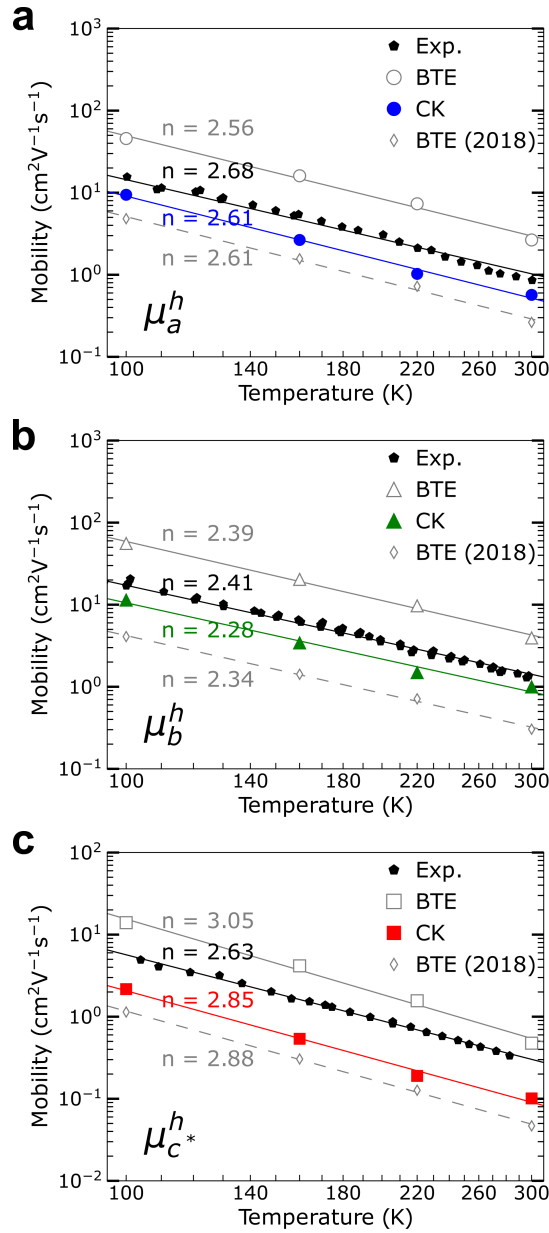


Figure 3.5: Hole carrier mobilities in naphthalene (μ^h) shown for the three crystallographic directions a , b , and c^* , computed both with the BTE in the relaxation time approximation (gray solid line) and with the CK approach (blue, green, and red). The computational settings are the same as in the electron mobility calculations. The BTE results presented in Ref. [3], which were obtained using a previous implementation of e -ph interactions with less accurate Wigner-Seitz cell summations, are shown as dashed lines for comparison. The exponent n from a T^{-n} power-law fit of the temperature dependence is given next to each curve. The experimental data (black) are from Ref. [20].

coupling fails to capture these essential polaron effects.

Comparison with hole mobilities

Finally, we present mobility results for hole carriers in naphthalene to contrast their behavior with electron carriers. We compute the hole mobility in naphthalene between 100–300 K using the CK approach, and compare the results to BTE calculations and experiments (see Fig. 3.5). The BTE calculations are a refinement of those we presented in Ref. [3], obtained here using a more accurate Wigner-Seitz cell summation procedure, as implemented in PERTURBO and described in detail in Ref. [34]. The revised BTE mobilities follow an identical temperature trend as in our previous results in Ref. [3], but their value is now greater than experiment, a physically meaningful trend for phonon-limited mobilities.

For hole carriers, both the BTE and CK methods give accurate predictions of the hole mobility, within a factor of 2–3 of experiment at all temperatures. The temperature dependence is nearly identical for the CK and the BTE mobilities, as shown by fitting the mobility curves with a T^{-n} power-law and giving the exponent n next to each curve in Fig. 3.5. These findings demonstrate that the band transport picture of the BTE, which is inadequate for electron carriers, is sufficient to describe transport for hole carriers due to their more dispersive bands (see Fig. 3.1) and overall weaker e -ph coupling (see Fig. 3.7 of supplementary material in Sec. 3.5).

3.3 Discussion

In naphthalene, measurements of the mobility in the direction normal to the molecular planes (c^* direction in Fig. 3.1) point to a transport regime different from the in-plane directions. In experiments, the mobility along c^* is lower than $1 \text{ cm}^2 \text{ V}^{-1} \text{ s}^{-1}$ and is nearly temperature independent between 100–300 K [20–22]. These trends suggest that charge transport normal to the molecular planes may occur in the small-polaron hopping regime, where the carriers are strongly localized and the e -ph interaction is so strong that a diagram-resummation technique such as the cumulant method is not expected to give accurate results.

We calculate the plane-normal mobility using both the BTE and CK methods, and compare the results with experiments in Fig. 3.6. The computed mobility decreases with temperature in both the CK and BTE approaches, deviating substantially from the nearly temperature independent mobility found in experiment. It is encouraging that the CK mobility agrees well with experiment at 100 K and its temperature dependence is weaker than in the BTE; fitting the temperature dependence with a

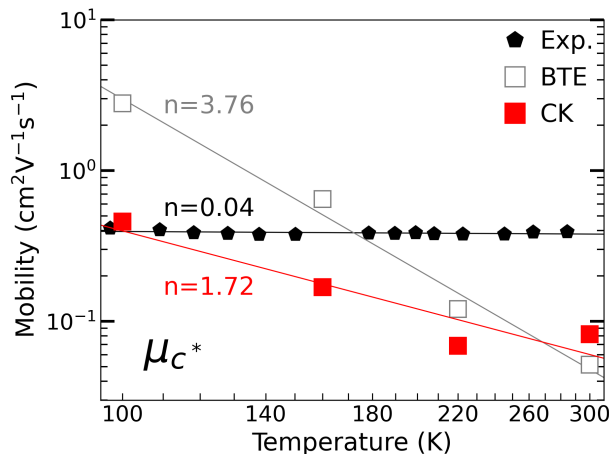


Figure 3.6: Electron mobility in the plane-normal direction in naphthalene. The plot compares CK and BTE calculations with experimental data from Ref. [20].

T^{-n} power law gives an exponent $n = 1.72$ in the CK and $n = 3.78$ in the BTE method, versus $n = 0.04$ in experiment. However, although the CK provides a significant improvement over the BTE, it is clear that neither method can accurately describe charge transport normal to the molecular planes.

The electron bands in the GW band structure are nearly flat in the plane-normal c^* -direction [Γ -Z direction in Fig. 3.3(b)], with large effective masses of order $15 m_e$ for the GW calculation done on the 100 K structure, and greater at higher temperatures. Combined with the absence of a power-law temperature trend in the experimental mobility, this relatively flat band suggests that electrons are nearly localized to a single molecular plane and that transport in the plane-normal direction occurs via small-polaron hopping. The failure of the CK approach in this regime highlights the need for predictive first-principles approaches to study charge transport in the small-polaron hopping regime in OMCs.

In summary, we studied the electron mobility in naphthalene crystal as a paradigmatic case of intermediate charge transport in OMCs. Combining a finite-temperature cumulant method and Green-Kubo transport calculations, we demonstrated accurate predictions of the electron mobility and its temperature dependence in the intermediate regime. Our results reveal a subtle interplay between inter- and intramolecular phonons: the low-energy intermolecular phonons determine the broadening of the QP peak, while the intramolecular phonons are responsible for forming polarons and the associated satellite peaks. Both types of phonons contribute to limit the mobility. The broad satellite removes spectral weight from the QP peak, modifying

the mobility and its temperature dependence. By capturing these subtle polaron effects, our CK approach addresses the shortcomings of the BTE for modeling the intermediate transport regime. We also highlighted the limitations of the CK approach to describe polaron-hopping between molecular planes. Taken together, our work advances microscopic understanding of the intermediate transport regime and paves the way for accurate first-principles calculations of the carrier mobility in OMCs.

3.4 Methods

First-principles calculations

We carry out first-principles density functional theory (DFT) calculations of the ground state and electronic structure of naphthalene using the QUANTUM ESPRESSO code [23, 24]. Thermal expansion of the lattice is taken into account by employing lattice constants [32] taken from experiments at four different temperatures of 100, 160, 220, and 300 K. All calculations are carried out separately at these four temperatures. The initial atomic positions are also taken from experiment [45, 46]. We use a kinetic energy cutoff of 90 Ry together with $2 \times 4 \times 2$ and $4 \times 4 \times 4$ \mathbf{k} -point grids for self-consistent and non-self-consistent calculations, respectively. The Grimme van der Waals correction [47, 48] is included during structural relaxation of the atomic positions. To improve the description of dynamical electronic correlations, we correct the DFT electronic band structure with G_0W_0 calculations, which include 500 bands in the polarization function and a cutoff of 10 Ry in the dielectric screening using the YAMBO code [29]. The WANNIER90 code [31] is employed to obtain Wannier functions and the corresponding transformation matrices, using the selected-columns-of-the-density-matrix method [49]. The lattice dynamics and e -ph perturbation potential are computed with density functional perturbation theory (DFPT) [33] calculations on a $2 \times 4 \times 2$ \mathbf{q} -point grid (here and below, \mathbf{q} is the phonon wavevector). Using our PERTURBO code [34], the electron and phonon data are combined to form the e -ph coupling matrix elements [34]:

$$g_{m\nu}(\mathbf{k}, \mathbf{q}) = \sqrt{\frac{\hbar}{2\omega_{\nu\mathbf{q}}}} \sum_{\kappa\alpha} \frac{\mathbf{e}_{\nu\mathbf{q}}^{\kappa\alpha}}{\sqrt{M_\kappa}} \langle m\mathbf{k} + \mathbf{q} | \partial_{\mathbf{q}\kappa\alpha} V | n\mathbf{k} \rangle, \quad (3.6)$$

where $|n\mathbf{k}\rangle$ are electronic Bloch states, $\omega_{\nu\mathbf{q}}$ are phonon energies, $\partial_{\mathbf{q}\kappa\alpha} V$ are e -ph perturbation potentials, $\mathbf{e}_{\nu\mathbf{q}}^{\kappa\alpha}$ are phonon displacement vectors, and M_κ is the mass of atom κ . The absolute value of the gauge-invariant e -ph coupling strength shown in Fig. 3.3(b) is computed for each phonon mode ν and phonon wavevector \mathbf{q} as [34]

$$|g_\nu(\mathbf{k}=0, \mathbf{q})| = \sqrt{\sum_{mn} |g_{mn\nu}(\mathbf{k}=0, \mathbf{q})|^2 / N_b}, \quad (3.7)$$

f where N_b is the number of selected bands. The mobility calculations use a fine \mathbf{k} -grid of $60 \times 60 \times 60$ for the BTE and $30 \times 30 \times 30$ for the CK method. Both methods use between 10^5 – 10^6 randomly selected \mathbf{q} -points.

Electron-phonon scattering rate

The relaxation time $\tau_{n\mathbf{k}}$ used in the BTE is computed as the inverse of the scattering rate, defined as [35]

$$\begin{aligned} \Gamma_{n\mathbf{k}}(T) = & \frac{2\pi}{\hbar} \sum_{m\nu\mathbf{q}} |g_{nm\nu}(\mathbf{k}, \mathbf{q})|^2 \\ & \times [(N_{\nu\mathbf{q}} + 1 - f_{m\mathbf{k}+\mathbf{q}})\delta(\varepsilon_{n\mathbf{k}} - \varepsilon_{n\mathbf{k}+\mathbf{q}} - \omega_{\nu\mathbf{q}}) \\ & + (N_{\nu\mathbf{q}} + f_{m\mathbf{k}+\mathbf{q}})\delta(\varepsilon_{n\mathbf{k}} - \varepsilon_{n\mathbf{k}+\mathbf{q}} + \omega_{\nu\mathbf{q}})], \end{aligned} \quad (3.8)$$

where $f_{n\mathbf{k}}$ and $N_{\nu\mathbf{q}}$ are electron Fermi-Dirac and phonon Bose-Einstein occupations in thermal equilibrium, respectively.

Cumulant method

The cumulant ansatz assumes that the retarded electron Green's function in the time domain takes the exponential form in Eq. (3.2), where the cumulant function $C_{n\mathbf{k}}$ is defined as [8, 37]

$$C_{n\mathbf{k}}(t, T) = \int_{-\infty}^{\infty} dE \frac{|\text{Im}\Sigma_{n\mathbf{k}}(E + \varepsilon_{n\mathbf{k}}, T)|}{\pi E^2} (e^{-iEt} + iEt - 1). \quad (3.9)$$

Here, $\varepsilon_{n\mathbf{k}}$ is the electron band energy, E the electron energy, and $\Sigma_{n\mathbf{k}}$ is the lowest-order (Fan-Migdal) e -ph self-energy [38]:

$$\Sigma_{n\mathbf{k}}(E, T) = \sum_{m\nu\mathbf{q}} |g_{mn\nu}(\mathbf{k}, \mathbf{q})|^2 \left[\frac{N_{\nu\mathbf{q}} + f_{m\mathbf{k}+\mathbf{q}}}{E - \varepsilon_{m\mathbf{k}+\mathbf{q}} + \omega_{\nu\mathbf{q}} + i\eta} + \frac{N_{\nu\mathbf{q}} + 1 + f_{m\mathbf{k}+\mathbf{q}}}{E - \varepsilon_{m\mathbf{k}+\mathbf{q}} - \omega_{\nu\mathbf{q}} + i\eta} \right], \quad (3.10)$$

whose temperature dependence is due to the occupation factors $N_{\nu\mathbf{q}}$ and $f_{n\mathbf{k}}$. Our cumulant Green's function includes e -ph Feynman diagrams of all orders: it sums over all the improper diagrams in which, at order n , the Fan-Migdal e -ph self-energy is repeated n times and weighted by a $1/n!$ factor [38]. After Fourier-transforming the retarded Green's function in Eq. (3.2) to the energy domain, we obtain the electron spectral function using Eq. (3.3). We compute $\text{Im}\Sigma_{n\mathbf{k}}(E)$ off-shell, using a fine energy E grid, and $\text{Re}\Sigma_{n\mathbf{k}}$ on-shell at the band energy $\varepsilon_{n\mathbf{k}}$, and use them as input to obtain the spectral function $A_{n\mathbf{k}}$ [8] as a function of electron energy E .

Dyson-Migdal spectral function

The Dyson-Migdal (DM) spectral function is given by

$$A_{n\mathbf{k}}^{\text{DM}}(E, T) = \frac{-\text{Im}\Sigma_{n\mathbf{k}}(T)}{[E - \varepsilon_{n\mathbf{k}} - \text{Re}\Sigma_{n\mathbf{k}}(T)]^2 + [\text{Im}\Sigma_{n\mathbf{k}}(T)]^2}, \quad (3.11)$$

where $\Sigma_{n\mathbf{k}}(T)$ is the lowest-order e -ph self-energy [Eq. (3.10)] computed on-shell at the band energy $\varepsilon_{n\mathbf{k}}$. The DM spectral function has a Lorentzian shape as a function of energy, with a linewidth of $2 \text{Im}\Sigma_{n\mathbf{k}}(T)$ which is proportional to the e -ph scattering rate in Eq. (3.8), $\Gamma_{n\mathbf{k}}(T) = 2 \text{Im}\Sigma_{n\mathbf{k}}(T)/\hbar$ [35].

3.5 Supplementary material

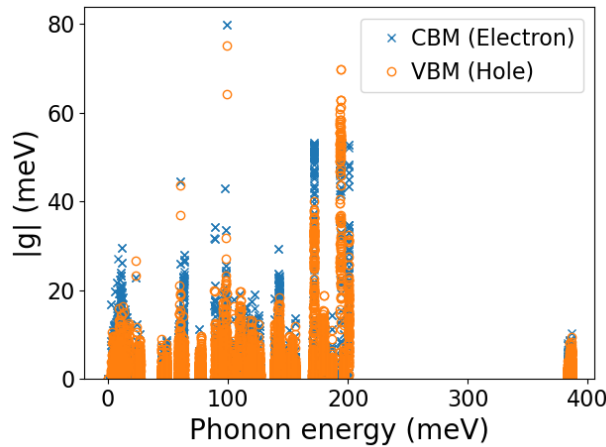


Figure 3.7: Comparison of the e -ph coupling strength, quantified by the absolute values of the e -ph matrix elements, $|g|$, for the valence band maximum (VBM) hole state and the conduction band minimum (CBM) electron state. The electrons exhibit an overall stronger coupling with phonons with energies between 0–200 meV, which, combined with the greater electron effective mass [see Fig. 3.1(b)], leads to a polaronic transport regime and the failure of the bandlike picture for electron carriers.

References

- [1] H. Oberhofer, K. Reuter, and J. Blumberger, *Chem. Rev.* **117**, 10319–10357 (2017).
- [2] W. P. Su, J. R. Schrieffer, and A. J. Heeger, *Phys. Rev. Lett.* **42**, 1698–1701 (1979).
- [3] N.-E. Lee, J.-J. Zhou, L. A. Agapito, and M. Bernardi, *Phys. Rev. B* **97**, 115203 (2018).
- [4] F. Brown-Altvater, G. Antonius, T. Rangel, M. Giantomassi, C. Draxl, X. Gonze, S. G. Louie, and J. B. Neaton, *Phys. Rev. B* **101**, 165102 (2020).

- [5] T. Holstein, *Ann. Phys.* **8**, 343–389 (1959).
- [6] R. A. Marcus, *Annu. Rev. Phys. Chem.* **15**, 155–196 (1964).
- [7] S. Fratini, D. Mayou, and S. Ciuchi, *Adv. Funct. Mater.* **26**, 2292–2315 (2016).
- [8] J.-J. Zhou and M. Bernardi, *Phys. Rev. Res.* **1**, 033138 (2019).
- [9] A. S. Mishchenko, N. Nagaosa, G. De Filippis, A. de Candia, and V. Cataudella, *Phys. Rev. Lett.* **114**, 146401 (2015).
- [10] N. E. Hussey, K. Takenaka, and H. Takagi, *Philos. Mag.* **84**, 2847–2864 (2004).
- [11] F. Ortmann, F. Bechstedt, and K. Hannewald, *Phys. Rev. B* **79**, 235206 (2009).
- [12] F. Ortmann, F. Bechstedt, and K. Hannewald, *New J. Phys.* **12**, 023011 (2010).
- [13] J. H. Fetherolf, D. Golež, and T. C. Berkelbach, *Phys. Rev. X* **10**, 021062 (2020).
- [14] L. J. Wang, Q. Peng, Q. K. Li, and Z. Shuai, *J. Chem. Phys.* **127**, 044506 (2007).
- [15] A. Troisi and G. Orlandi, *Phys. Rev. Lett.* **96**, 086601 (2006).
- [16] L. Wang, Q. Li, Z. Shuai, L. Chen, and Q. Shi, *Phys. Chem. Chem. Phys.* **12**, 3309 (2010).
- [17] L. Wang and D. Beljonne, *J. Phys. Chem. Lett.* **4**, 1888–1894 (2013).
- [18] S. Ciuchi, S. Fratini, and D. Mayou, *Phys. Rev. B* **83**, 081202 (2011).
- [19] T. Nematiram, S. Ciuchi, X. Xie, S. Fratini, and A. Troisi, *J. Phys. Chem. C* **123**, 6989–6997 (2019).
- [20] O. Madelung, U. Rössler, and M. Schulz, eds., *Naphthalene, C₁₀H₈ charge carrier mobilities: Datasheet from Landolt-Börnstein - Group III Condensed Matter · Volume 41E: “Ternary Compounds, Organic Semiconductors” in SpringerMaterials* (Springer-Verlag Berlin Heidelberg, 2000).
- [21] L. B. Schein and A. R. McGhie, *Phys. Rev. B* **20**, 1631–1639 (1979).
- [22] L. B. Schein, C. B. Duke, and A. R. McGhie, *Phys. Rev. Lett.* **40**, 197–200 (1978).
- [23] P. Giannozzi, S. Baroni, N. Bonini, M. Calandra, R. Car, C. Cavazzoni, D. Ceresoli, G. L. Chiarotti, M. Cococcioni, I. Dabo, A. Dal Corso, S. de Gironcoli, S. Fabris, G. Fratesi, R. Gebauer, U. Gerstmann, C. Gougoussis, A. Kokalj, M. Lazzeri, L. Martin-Samos, N. Marzari, F. Mauri, R. Mazzarello, S. Paolini, A. Pasquarello, L. Paulatto, C. Sbraccia, S. Scandolo, G. Sclauzero, A. P. Seitsonen, A. Smogunov, P. Umari, and R. M. Wentzcovitch, *J. Phys. Condens. Matter* **21**, 395502 (2009).

- [24] P. Giannozzi, O. Andreussi, T. Brumme, O. Bunau, M. Buongiorno Nardelli, M. Calandra, R. Car, C. Cavazzoni, D. Ceresoli, M. Cococcioni, N. Colonna, I. Carnimeo, A. Dal Corso, S. de Gironcoli, P. Delugas, R. A. DiStasio, A. Ferretti, A. Floris, G. Fratesi, G. Fugallo, R. Gebauer, U. Gerstmann, F. Giustino, T. Gorni, J. Jia, M. Kawamura, H.-Y. Ko, A. Kokalj, E. Küçükbenli, M. Lazzeri, M. Marsili, N. Marzari, F. Mauri, N. L. Nguyen, H.-V. Nguyen, A. Otero-de-la-Roza, L. Paulatto, S. Poncé, D. Rocca, R. Sabatini, B. Santra, M. Schlipf, A. P. Seitsonen, A. Smogunov, I. Timrov, T. Thonhauser, P. Umari, N. Vast, X. Wu, and S. Baroni, *J. Phys. Condens. Matter* **29**, 465901 (2017).
- [25] J. P. Perdew, K. Burke, and M. Ernzerhof, *Phys. Rev. Lett.* **77**, 3865–3868 (1996).
- [26] N. Troullier and J. L. Martins, *Phys. Rev. B* **43**, 1993–2006 (1991).
- [27] M. van Setten, M. Giantomassi, E. Bousquet, M. Verstraete, D. Hamann, X. Gonze, and G.-M. Rignanese, *Comput. Phys. Commun.* **226**, 39–54 (2018).
- [28] L. Hedin, *Phys. Rev.* **139**, A796–A823 (1965).
- [29] A. Marini, C. Hogan, M. Grüning, and D. Varsano, *Comput. Phys. Commun.* **180**, 1392–1403 (2009).
- [30] N. Marzari, A. A. Mostofi, J. R. Yates, I. Souza, and D. Vanderbilt, *Rev. Mod. Phys.* **84**, 1419–1475 (2012).
- [31] A. A. Mostofi, J. R. Yates, Y.-S. Lee, I. Souza, D. Vanderbilt, and N. Marzari, *Comput. Phys. Commun.* **178**, 685–699 (2008).
- [32] C. P. Brock and J. D. Dunitz, *Acta. Crystallogr. B* **38**, 2218–2228 (1982).
- [33] S. Baroni, S. de Gironcoli, A. Dal Corso, and P. Giannozzi, *Rev. Mod. Phys.* **73**, 515–562 (2001).
- [34] J.-J. Zhou, J. Park, I.-T. Lu, I. Maliyov, X. Tong, and M. Bernardi, *Comput. Phys. Commun.* **264**, 107970 (2021).
- [35] M. Bernardi, *Eur. Phys. J. B* **89**, 239 (2016).
- [36] W. Li, *Phys. Rev. B* **92**, 075405 (2015).
- [37] J. J. Kas, J. J. Rehr, and L. Reining, *Phys. Rev. B* **90**, 085112 (2014).
- [38] G. D. Mahan, *Many-Particle Physics* (Springer US, New York, 2000).
- [39] F. Aryasetiawan and O. Gunnarsson, *Rep. Prog. Phys.* **61**, 237–312 (1998).
- [40] S. M. Story, J. J. Kas, F. D. Vila, M. J. Verstraete, and J. J. Rehr, *Phys. Rev. B* **90**, 195135 (2014).
- [41] J. P. Nery, P. B. Allen, G. Antonius, L. Reining, A. Miglio, and X. Gonze, *Phys. Rev. B* **97**, 115145 (2018).
- [42] E. N. Economou, *Green's Functions In Quantum Physics*, Vol. 7, Springer Series in Solid-State Sciences (Springer Berlin, Heidelberg, 2006).

- [43] K. Hannewald, V. M. Stojanović, J. M. T. Schellekens, P. A. Bobbert, G. Kresse, and J. Hafner, *Phys. Rev. B* **69**, 075211 (2004).
- [44] J.-J. Zhou, J. Park, I. Timrov, A. Floris, M. Cococcioni, N. Marzari, and M. Bernardi, *Phys. Rev. Lett.* **127**, 126404 (2021).
- [45] S. Gražulis, D. Chateigner, R. T. Downs, A. F. T. Yokochi, M. Quirós, L. Lutterotti, E. Manakova, J. Butkus, P. Moeck, and A. Le Bail, *J. Appl. Crystallogr.* **42**, 726–729 (2009).
- [46] S. Gražulis, A. Daškevič, A. Merkys, D. Chateigner, L. Lutterotti, M. Quirós, N. R. Serebryanaya, P. Moeck, R. T. Downs, and A. Le Bail, *Nucleic Acids Res.* **40**, D420–D427 (2012).
- [47] S. Grimme, *J. Comput. Chem.* **27**, 1787–1799 (2006).
- [48] V. Barone, M. Casarin, D. Forrer, M. Pavone, M. Sambri, and A. Vittadini, *J. Comput. Chem.* **30**, 934–939 (2009).
- [49] G. Pizzi, V. Vitale, R. Arita, S. Blügel, F. Freimuth, G. Géranton, M. Gibertini, D. Gresch, C. Johnson, T. Koretsune, J. Ibañez-Azpiroz, H. Lee, J.-M. Lihm, D. Marchand, A. Marrazzo, Y. Mokrousov, J. I. Mustafa, Y. Nohara, Y. Nomura, L. Paulatto, S. Poncé, T. Ponweiser, J. Qiao, F. Thöle, S. S. Tsirkin, M. Wierzbowska, N. Marzari, D. Vanderbilt, I. Souza, A. A. Mostofi, and J. R. Yates, *J. Phys. Condens. Matter* **32**, 165902 (2020).

*Chapter 4***ELECTRON-PHONON INTERACTIONS AND POLARONS
IN THE PARENT CUPRATE La_2CuO_4**

This chapter is a slightly modified version of the preprint: B. K. Chang, I. Timrov, J. Park, J.-J. Zhou, N. Marzari, and M. Bernardi, “First-principles electron-phonon interactions and polarons in the parent cuprate La_2CuO_4 ”, [arXiv:2401.11322](https://arxiv.org/abs/2401.11322), under review in *Phys. Rev. Lett.*

4.1 Introduction

Angle-resolved photoemission spectroscopy (ARPES) has provided ample evidence for broad spectral functions in several cuprate compounds [1–5]. This spectral broadening has been associated with strong electron-phonon (e -ph) interactions and polaronic behavior in doped and undoped cuprates [2, 3, 5]. Existing models can account phenomenologically for the observed spectral broadening [1, 2, 6]. Yet developing a deeper understanding based on rigorous theory and quantitative calculations has been difficult, mainly due to the strong electron correlations governing cuprate physics [7, 8].

In parent (undoped) cuprate compounds, the strong Coulomb repulsion of localized Cu $3d$ electrons induces an antiferromagnetic (AFM) Mott insulating ground state [9, 10] which can be described qualitatively using Hubbard-like or t - J models [11, 12]. These Hamiltonians can also be combined with model e -ph interactions to predict the broadening of electron spectral functions [3, 13–17]. However, key microscopic quantities needed for a realistic description of e -ph coupling in most high-temperature superconductors remain unknown, including the strength of the e -ph interactions, their dependence on electron and phonon momenta, their effects on electron spectral functions, and which atomic vibrations dominate the coupling. Owing to recent progress, first-principles calculations are able to characterize e -ph interactions and electron spectral functions also in correlated metals and insulators [18–20]. For cuprates, such quantitative studies have so far focused on metallic (doped) compounds relying on the local-density approximation (LDA) [21–23], which cannot correctly describe the Mott insulating ground state of parent cuprates. Recent work has studied parent cuprates using improved functionals [24–27] or Hubbard-corrected density functional theory (DFT+ U) [28–30] to obtain reliable

ground state and phonon spectra [30, 31]. Even within these improved schemes, e -ph interactions in parent cuprates remain unexplored.

In this chapter, we show fully *ab initio* calculations of e -ph interactions and electron spectral functions in a prototypical parent cuprate, La_2CuO_4 (LCO). We employ a combination of advanced first-principles techniques, including linear-response DFT+ U and recently developed treatments of anharmonic phonons [32], strong e -ph interactions, and polarons [33, 34]. Starting from an accurate ground state, we show that e -ph interactions in LCO are governed by two families of longitudinal optical (LO) phonons with strong Fröhlich-type coupling. These LO modes consist of stretching and bending of Cu-O bonds and vibration of apical O atoms. The computed valence band spectral functions exhibit significant peak broadening and renormalization, as well as pronounced phonon sidebands. These features are governed by the strongly-coupled LO phonons, with a smaller contribution from lower-energy polar modes. Our results provide a quantitative evidence for strong e -ph interactions and polarons in parent cuprates mediated by multiple optical phonons, thus deepening our microscopic understanding of cuprate physics beyond analytical models.

4.2 Results

We compute the ground state of LCO in the low-temperature orthorhombic phase [35–37] using collinear spin-polarized DFT+ U calculations in a plane-wave basis with the QUANTUM ESPRESSO package [38, 39]. The Hubbard- U parameter for the Cu $3d$ states is calculated (rather than fitted) self-consistently with the relaxed crystal structure [40–42], thus removing any tunable parameter in our calculations. We employ the SSCHA method [32] to compute effective harmonic phonon dispersions at 150 K, a temperature where LCO is in its antiferromagnetic (AFM) state [37, 43]. The e -ph perturbation potentials, obtained on a coarse irreducible \mathbf{q} -point grid with DFPT+ U [39, 44], include both the Kohn-Sham and Hubbard perturbation terms [18]. We use the PERTURBO code [45] to compute the e -ph matrix elements [18, 45], $g_{mn\nu}^\sigma(\mathbf{k}, \mathbf{q})$, and interpolate them using Wannier functions from WANNIER90 [46]. (These matrix elements represent the probability amplitude for an electron in a Bloch state $\psi_{n\mathbf{k}}^\sigma$, with band index n , spin σ , and crystal momentum \mathbf{k} , to scatter into state $\psi_{m\mathbf{k}+\mathbf{q}}^\sigma$ by emitting or absorbing a phonon with mode index ν and wave-vector \mathbf{q} [39, 45, 47].) The electron spectral functions are computed at finite temperature with a cumulant approach described in Ref. [34]. This method can capture strong e -ph interactions and polaron effects, such as the broadening and weight

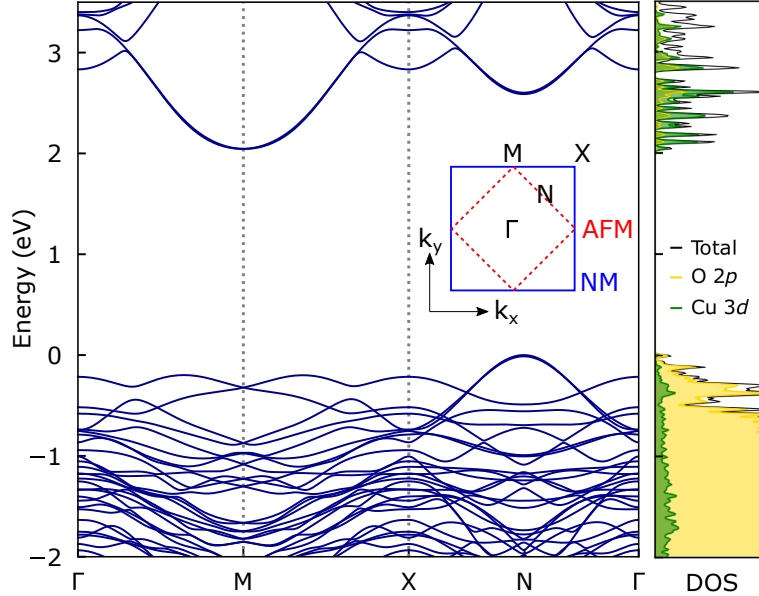


Figure 4.1: Band structure of LCO in its AFM phase computed with DFT+ U . The inset shows the in-plane Brillouin zone of the nonmagnetic (NM, blue) and antiferromagnetic (AFM, red) phases, with high-symmetry points Γ , M , N , and X labeled. The right panel gives the total density of states (DOS) and its contributions from O $2p$ and Cu $3d$ atomic states. The energy zero is set to the top of valence band.

renormalization of the quasiparticle peak and the emergence of phonon sidebands, as we have shown in recent studies on oxides [18, 34] and organic crystals [48]. Additional computational details are provided in the supplementary material (SM) in Sec. 4.4.

Figure 4.1 shows the band structure of LCO computed with DFT+ U . The valence band dispersion near the gap resembles conventional t - J model results for insulating cuprates [49, 50], with the valence band maximum (VBM) at the nodal point N [$\mathbf{k} = (\frac{\pi}{2}, \frac{\pi}{2})$] and additional lower-energy valleys near the antinodal point M [$\mathbf{k} = (\pi, 0)$]. The computed band gap is $E_g = 2.04$ eV and the Cu magnetic moment is $\mu_{\text{Cu}} = 0.62\mu_B$, in excellent agreement with the respective experimental values, $E_g^{\text{exp}} = 2.0$ eV [51, 52] and $\mu_{\text{Cu}}^{\text{exp}} = 0.60$ – $0.64\mu_B$ [36, 53] (see additional discussion in the SM in Sec. 4.4).

Starting from this accurate ground state, we compute the phonon dispersions (inclusive of anharmonic effects) and map out the mode-resolved strength of the e -ph interactions in Fig. 4.2(a). The experimental frequency of a Cu-O bond-stretching LO

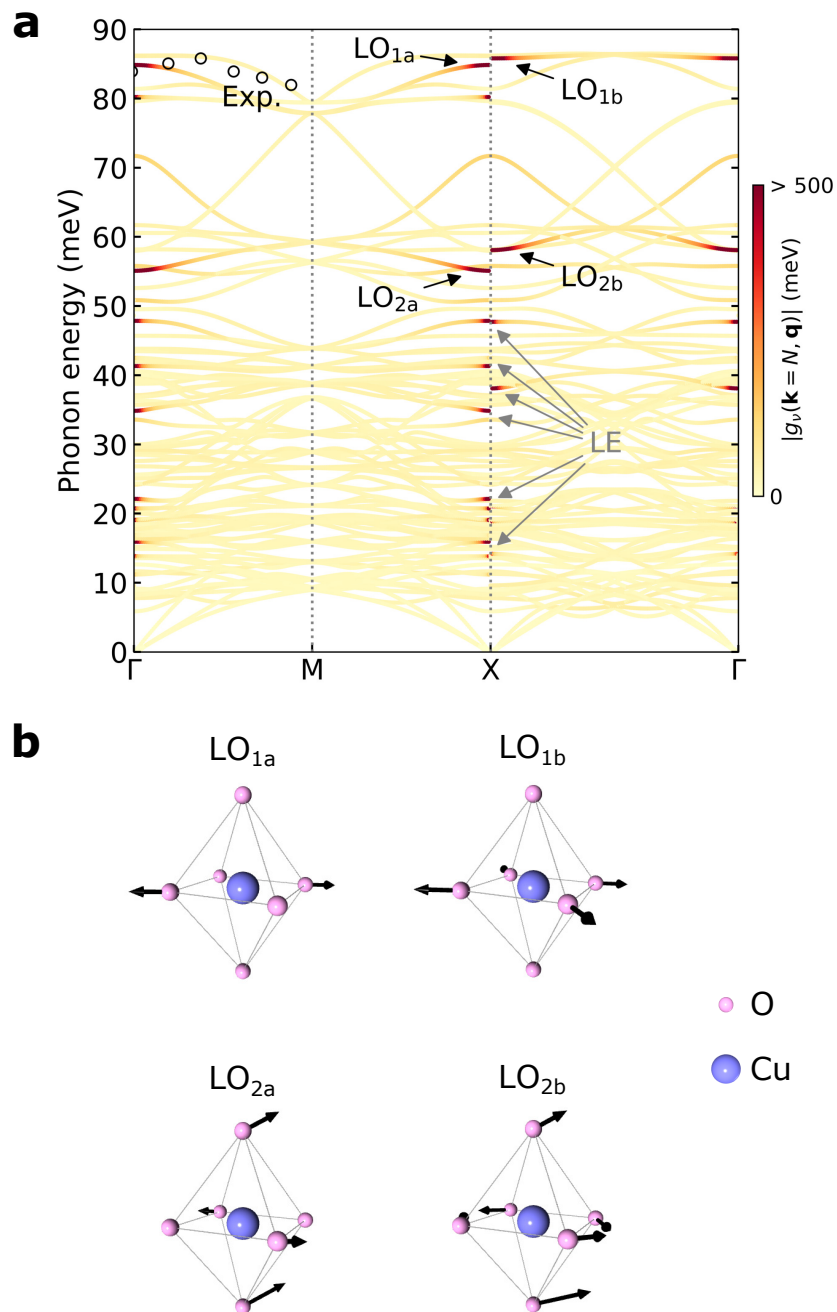


Figure 4.2: (a) Calculated phonon dispersion overlaid with the e -ph coupling strength $|g_\nu(\mathbf{k}, \mathbf{q})|$ computed at the nodal point $\mathbf{k} = N$. Experimental LO-mode energies are given for comparison with hollow circles [54]. The four most strongly-coupled LO modes (LO_{1a,b} and LO_{2a,b}) are indicated with black arrows, and lower-energy (LE) strongly-coupled modes with gray arrows. (b) Atomic displacements for the four strongly-coupled LO modes, with blue and pink spheres representing Cu and O atoms, respectively.

mode, measured by neutron scattering [54] and given for comparison in Fig. 4.2(a), is in very good agreement with our calculations. As the high-symmetry X -point in the nonmagnetic (NM) phase is equivalent to the zone center (Γ point) of the AFM phase, we find multiple discontinuities in the phonon dispersion near X due to LO–TO splitting combined with orthorhombic ab -anisotropy, similar to the behavior observed in orthorhombic $\text{YBa}_2\text{Cu}_3\text{O}_{6+x}$ [55, 56]. We highlight the importance of temperature and anharmonic effects included in our SSCHA calculation; conversely, zero-temperature DFPT+ U phonons exhibit unphysical dynamical instabilities (see the SM in Sec. 4.4).

Figure 4.2(a) also shows the e -ph coupling strength for each phonon mode [45], $|g_\nu(\mathbf{k}, \mathbf{q})|$, computed at the electron nodal point $\mathbf{k} = N$. We identify two groups of LO phonons with strong Fröhlich-type coupling [57], named here LO_1 and LO_2 , with respective energies $\omega_1 \approx 85$ meV and $\omega_2 \approx 55$ meV. We further distinguish between strongly coupled modes at opposite sides of the AFM zone center (X point), labeling them with indices a and b respectively. At small wave-vector ($\Delta q \approx 0.015 \text{ \AA}^{-1}$) near X , these LO modes exhibit large e -ph coupling strengths, with values $|g_2| \approx 5.5$ eV for the $\text{LO}_{2a,b}$ and $|g_1| \approx 3.9$ eV for the $\text{LO}_{1a,b}$ phonons. These long-wavelength modes govern the e -ph physics in LCO as their e -ph coupling strengths are orders of magnitude greater than the Brillouin-zone average value (44 meV). Such coupling strengths exceed those in strongly correlated metals (highest $|g| \approx 100$ meV in Sr_2RuO_4) [20], and have the same order of magnitude as the Fröhlich coupling strengths in insulating oxides with polaron effects, including CoO and SrTiO_3 [18, 34, 58].

Notably, the energies of the LO_1 and LO_2 modes coincide with those of strongly-coupled phonons observed experimentally in several *doped* cuprates, as evidenced by a universal kink in their quasiparticle (QP) band dispersion found in ARPES measurements [59–61]. So far, these features have not been observed experimentally in undoped cuprates due to their broader ARPES spectra [4]. Our results show quantitatively that strong e -ph interactions are already present at these energies in the parent cuprate LCO.

The four strongly-coupled LO modes are associated with O-atom vibrations, as shown in Fig. 4.2(b). The LO_{1a} and LO_{1b} modes correspond to vibrations in the CuO_2 plane consisting of oxygen breathing motions. These Cu-O bond-stretching modes have been shown to couple strongly with holes in neutron scattering measurements [62] and are linked to Cu-O charge transfer [55] and formation of charge-

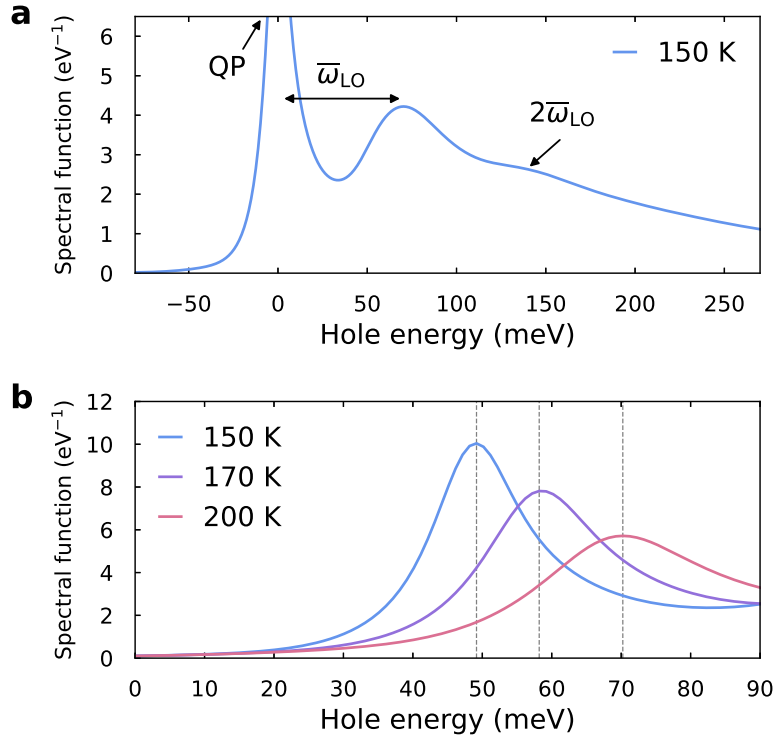


Figure 4.3: (a) Spectral function of the VBM hole state in LCO computed at 150 K. The satellite peak is centered at $\bar{\omega}_{LO}$, the average of the LO_1 and LO_2 phonon energies. A second overtone feature at $2\bar{\omega}_{LO}$ is also shown. The energy zero is set to the QP peak energy. (b) Temperature-dependent spectral function of the VBM state computed at three temperatures, with the QP peak energies shown with dashed lines. The spectral functions are aligned at their energy onsets.

ordered phases [56]. The LO_{2a} and LO_{2b} modes, on the other hand, involve both in-plane Cu-O bond-bending, with O atoms moving normal to the Cu-O bonds [56], and motion of the apical O atoms outside the CuO_2 planes [63]. The ~ 55 meV energy of the $LO_{2a,b}$ modes is consistent with bond-bending modes measured in the doped LCO compound $La_{2-x}Sr_xCuO_4$ (LSCO) [62].

We find additional lower-energy (LE) modes, with energies between 15–50 meV, whose e -ph coupling strengths are significant ($|g| \approx 1\text{--}2$ eV at Δq from X) but weaker than those of the $LO_{1,2}$ modes. These strongly-coupled LE modes consist mainly of Cu-O bond-bending and apical O vibrations, with modes at lower energies associated with higher-amplitude oscillations of Cu and La atoms. Importantly, while Cu-O bond-stretching modes have received the most attention in the cuprates, our results show that bond-bending and apical oxygen motions possess the strongest e -ph coupling and govern e -ph physics in LCO.

The spectral functions exhibit clear signatures of strong e -ph coupling. Figure 4.3(a) illustrates this result for the valence band maximum (VBM) hole state. The e -ph interactions broaden the QP peak and significantly decrease its spectral weight to $Z=0.25$. In addition, we find a satellite peak at hole energy $\bar{\omega}_{LO} \approx 70$ meV accompanied by a less pronounced overtone at $2\bar{\omega}_{LO} \approx 140$ meV relative to the QP peak¹. These phonon sidebands form as a result of strong e -ph coupling with the LO₁ and LO₂ modes, whose average energy equals the satellite energy $\bar{\omega}_{LO} \approx 70$ meV. Other phonons with appreciable e -ph coupling, such as the LE modes, can also redistribute spectral weight and modify the spectral function. Yet due to their lower energy and weaker e -ph coupling, their satellites carry less weight and merge into a broad incoherent background.

Our spectral function calculations can be viewed as a quantitative version of the Franck-Condon broadening (FCB) model, which describes the spectral functions in (un)doped cuprates as a superposition of multiple incoherent peaks [1, 2, 6]. The QP-peak broadening and renormalization in our calculations is consistent with both experimental results and the FCB model. Yet our computed spectral functions exhibit well-defined QP peaks, which are typically missing in experiments on undoped cuprates [1, 2]. We attribute this discrepancy to the small QP weight ($Z = 0.25$), as predicted here, which makes the QP peak easily washed out in real samples by defect- and magnon-induced broadening not considered in this work [64–66]. One difference with the FCB model is that the phonon sidebands decay rapidly with hole energy in our calculations, similar to previous results for large polarons in oxides [18, 34], and are not visible beyond the second overtone at $2\bar{\omega}_{LO}$. In contrast, the FCB model predicts a series of intense satellites.

Our calculations can also explain an anomalous shift with temperature of the spectral function peak [1]. A model proposed by Kim *et al.* [1] predicts that the peak energy E_p of the spectral function shifts with temperature according to $\Delta E_p \approx \pi k_B \Delta T$, where k_B is the Boltzmann constant. This formula provides only a crude estimate—for example, the measured temperature dependence is twice greater than predicted by this model in undoped Sr₂CuO₂Cl₂ and Ca₂CuO₂Cl₂ between 100–400 K. In contrast, our calculations on LCO can predict with a high accuracy the temperature dependence of the peak observed experimentally. Figure 4.3(b) shows the computed

¹Our results are given in terms of hole energies, which correspond to negative electron energies relative to the QP peak. Note also that phonon satellites appear at electron energies lower than the QP peak for p -doped materials, as we assume here; the sign of the satellite energy would be reversed in the n -doped case [34].

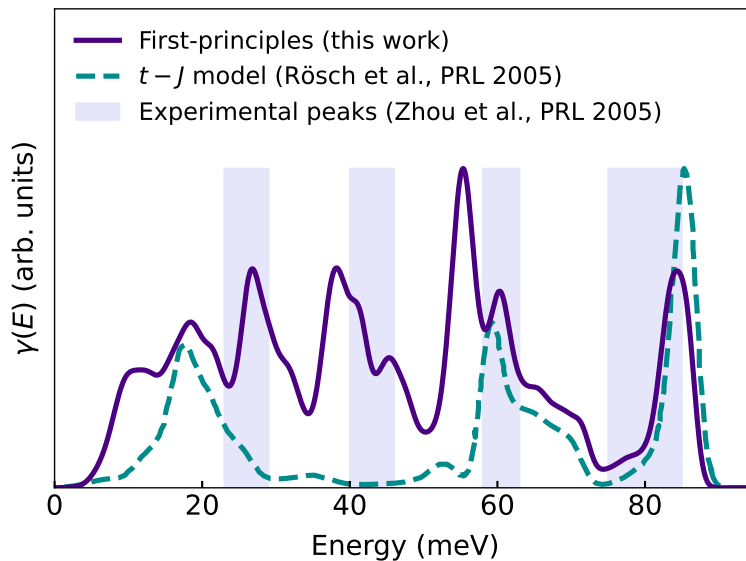


Figure 4.4: Electron-phonon coupling distribution function, $\gamma(E)$, computed using Eq. (4.1) (solid curve). For comparison, we show $t-J$ model results from Ref. [3] (dashed curve) and the range of the experimental self-energy peaks in LSCO from Ref. [67] (shaded regions). The distribution curves are normalized to the same maximum height.

spectral functions of the VBM hole state at three temperatures between 150–200 K. For an initial temperature of 150 K, increasing the temperature to 170 K and 200 K gives, respectively, a peak shift of 5 and 13 meV when using the simple model, versus 9 and 21 meV in our calculation, which corresponds to a ~ 0.45 meV/K peak shift. Our computed values are twice greater than the model and are in very good agreement with the ~ 0.5 meV/K peak shift extracted from ARPES experiments on undoped cuprates [1].

Conventional analysis of e -ph interactions in cuprates focuses on the e -ph coupling distribution function [3], which combines contributions to e -ph coupling from all phonons (with energies $\hbar\omega_{\nu\mathbf{q}}$) at a given energy E :

$$\gamma(E) = \sum_{\nu\mathbf{q}} |g_{\nu}(\mathbf{k}, \mathbf{q})|^2 \delta(E - \hbar\omega_{\nu\mathbf{q}}). \quad (4.1)$$

This quantity has been computed using a $t-J$ model [3] to interpret the measured electron self-energy in underdoped LSCO [67]. This model calculation gives a distribution function that captures the experimental self-energy peaks at 25, 60, and 80 meV (see Fig. 4.4). However, the peak observed in experiments at ~ 40 meV

is absent in the model calculations. Previous work attributed this missing peak to surface effects or distortions due to doping in real samples [3].

We compute the e -ph coupling distribution function for the nodal point $\mathbf{k} = N$ in our first-principles settings. As shown in Fig. 4.4, our computed distribution function agrees with t - J model results above 60 meV and brings the position of the 25-meV peak closer to experiments [67]. Importantly, our calculations recover the missing peak at 40 meV, which is due to e -ph interactions with LE modes associated with bond-bending and apical O vibrations. This demonstrates that the 40-meV feature observed in LSCO [67] is already present in the undoped parent phase and is not a consequence of doping. The 40-meV feature is absent in the t - J model because it considers only the Cu $d_{x^2-y^2}$ and O $p_{x,y}$ orbitals [11, 13], so e -ph interactions from Cu-O bond-bending and apical O vibrations are not properly described. Our results suggest that an accurate effective model of e -ph physics in cuprates would need to take into account additional electronic orbitals and phonon modes.

4.3 Discussion

In summary, we study e -ph interactions in the parent cuprate LCO using state-of-the-art first-principles calculations. We show that strong e -ph interactions are an intrinsic feature of the undoped phase and are mediated by two classes of LO phonons with Fröhlich coupling, both consisting of Cu-O bond-bending, bond-stretching and apical O-atom vibrations, with smaller contributions from LE polar modes. Capturing this physics allows us to explain key features of the valence band spectral functions, including their significant broadening and QP weight renormalization, the presence of phonon sidebands with a broad incoherent background, and the origin of a 40 meV peak in the energy distribution functions not accounted for by existing models. As many parent high-temperature superconductors are ionic insulators, we believe that strong Fröhlich-type e -ph coupling may be a general feature of parent phases, and plan to investigate this point in broader classes of superconductors in the future.

4.4 Supplementary material

Computational details

We use Hubbard-corrected density functional theory (DFT+ U) to compute the electronic ground state of La_2CuO_4 (LCO) with a 14-atom antiferromagnetic (AFM) primitive unit cell in the low-temperature orthorhombic phase (space group $Cmca$) [35–37, 43, 68]. Our calculations employ the PBEsol exchange-correlation functional [69] and ultrasoft pseudopotentials [70] from the GBRV library [71], together with kinetic energy cutoffs of 65 Ry and 520 Ry for the wave functions and charge density, respectively, and a $4 \times 4 \times 4$ \mathbf{k} -point grid. Atomic orbitals are used as the basis for the Hubbard manifold.

We calculate the Hubbard- U parameter and the relaxed crystal structure from first principles in a self-consistent way [40]. Starting from $U=0$ and a given initial crystal structure, we use a density functional perturbation theory (DFPT) approach [42], as implemented in the HP code [41], to compute the Hubbard- U parameter on a $4 \times 4 \times 4$ \mathbf{q} -point grid. We then use DFT+ U with the newly computed U value to relax the cell and obtain a new crystal structure, which in turn we use to recalculate U . We repeat this process until convergence, where the Hubbard- U parameter and crystal structure stop changing appreciably. The final self-consistent Hubbard-parameter for the Cu $3d$ states is $U_{\text{sc}} = 10.00$ eV and the fully relaxed lattice parameters are $a = 5.524$ Å, $b = 5.335$ Å, and $c = 12.891$ Å.

The electron-phonon (e -ph) perturbation potential is obtained with Hubbard-corrected density functional perturbation theory (DFPT+ U) [39, 44] on a coarse irreducible $2 \times 2 \times 2$ \mathbf{q} -point grid. We compute the phonon dispersion using the stochastic self-consistent harmonic approximation (SSCHA) [32] with an ensemble of 750 configurations, each consisting of a $2 \times 2 \times 2$ supercell with random atomic displacements. The interatomic forces and total energy of each configuration are evaluated using DFT+ U .

Following standard convention from the literature [50, 72], the calculated band structure and phonon dispersion of the AFM primitive cell are folded to the Brillouin zone of the nonmagnetic (NM) conventional unit cell. Therefore, the Brillouin zone labeling in the main text and below refers to the NM conventional unit cell.

Band gap and magnetic moment as a function of Hubbard- U parameter

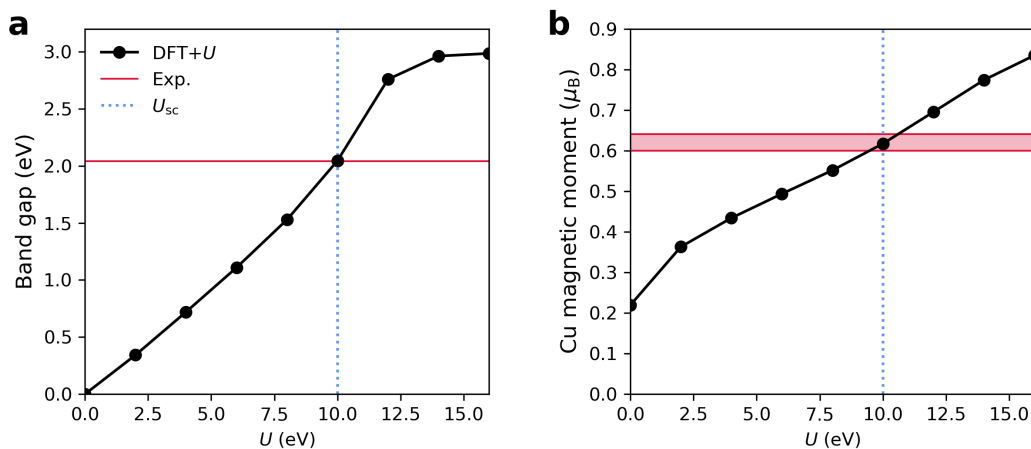


Figure 4.5: (a) Electronic band gap and (b) Cu magnetic moment (in Bohr magneton units) computed using collinear spin-polarized DFT+ U with different Hubbard U values. The experimental band gap [51, 52] and Cu magnetic moment [36, 53] are shown with red horizontal lines in the respective plots (for the magnetic moment, the shaded region corresponds to a range of values found in the literature). The Hubbard- U value determined self-consistently (U_{sc}) and used for all calculations in the main text is indicated with a blue dashed line in each panel.

Phonon dispersions from DFPT+ U and SSCHA

Figure 4.6(a) below compares phonon dispersions computed with DFPT+ U and with the SSCHA method employed together with DFT+ U . The dispersions from the two methods are in close agreement at energies greater than 15 meV, but differ significantly at lower energy due to the presence of soft phonons. Inelastic neutron scattering (INS) experiments [73–75] have shown that La_2CuO_4 and $\text{La}_{2-x}\text{Sr}_x\text{CuO}_4$ possess soft phonons associated with tilting and rotation of the CuO_6 octahedra.

Accordingly, we find two branches of soft phonons [labeled S_1 and S_2 in Fig. 4.6(a)], which are not described correctly in zero-temperature DFPT+ U calculations. These modes are visualized in Fig. 4.6(b): the soft phonon S_2 is a well-known CuO_6 -octahedron tilting mode responsible for the orthorhombic-to-tetragonal phase transition [73, 74], while the S_1 phonon is a Cu shear mode discussed less often in literature.

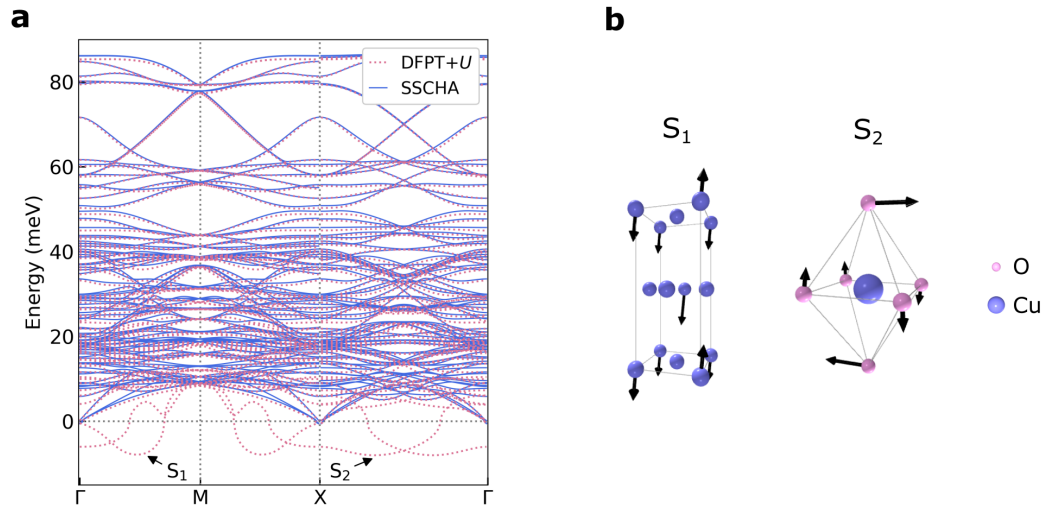


Figure 4.6: (a) Phonon dispersion of La_2CuO_4 in the low-temperature orthorhombic phase. The plot compares DFPT+ U (pink dotted curves) and SSCHA calculations (blue solid curves). The two soft modes are indicated with arrows in the DFPT+ U dispersion. (b) Visualization of the two soft phonons, with arrows representing atomic displacements. Mode S_1 is shown in the Cu-sublattice of the conventional unit cell, and mode S_2 in a CuO_6 octahedron. Pink and blue spheres represent O and Cu atoms, respectively.

References

- [1] C. Kim, F. Ronning, A. Damascelli, D. L. Feng, Z.-X. Shen, B. O. Wells, Y. J. Kim, R. J. Birgeneau, M. A. Kastner, L. L. Miller, H. Eisaki, and S. Uchida, *Phys. Rev. B* **65**, 174516 (2002).
- [2] K. M. Shen, F. Ronning, D. H. Lu, W. S. Lee, N. J. C. Ingle, W. Meevasana, F. Baumberger, A. Damascelli, N. P. Armitage, L. L. Miller, Y. Kohsaka, M. Azuma, M. Takano, H. Takagi, and Z.-X. Shen, *Phys. Rev. Lett.* **93**, 267002 (2004).
- [3] O. Rösch, O. Gunnarsson, X. J. Zhou, T. Yoshida, T. Sasagawa, A. Fujimori, Z. Hussain, Z.-X. Shen, and S. Uchida, *Phys. Rev. Lett.* **95**, 227002 (2005).
- [4] F. Ronning, K. M. Shen, N. P. Armitage, A. Damascelli, D. H. Lu, Z.-X. Shen, L. L. Miller, and C. Kim, *Phys. Rev. B* **71**, 094518 (2005).
- [5] K. M. Shen, F. Ronning, W. Meevasana, D. H. Lu, N. J. C. Ingle, F. Baumberger, W. S. Lee, L. L. Miller, Y. Kohsaka, M. Azuma, M. Takano, H. Takagi, and Z.-X. Shen, *Phys. Rev. B* **75**, 075115 (2007).
- [6] G. A. Sawatzky, *Nature* **342**, 480–481 (1989).
- [7] O. Gunnarsson and O. Rösch, *J. Phys. Condens. Matter* **20**, 043201 (2008).

- [8] B. Keimer, S. A. Kivelson, M. R. Norman, S. Uchida, and J. Zaanen, *Nature* **518**, 179–186 (2015).
- [9] P. A. Lee, N. Nagaosa, and X.-G. Wen, *Rev. Mod. Phys.* **78**, 17–85 (2006).
- [10] A. Damascelli, Z. Hussain, and Z.-X. Shen, *Rev. Mod. Phys.* **75**, 473–541 (2003).
- [11] F. C. Zhang and T. M. Rice, *Phys. Rev. B* **37**, 3759–3761 (1988).
- [12] M. T. Schmid, J.-B. Morée, R. Kaneko, Y. Yamaji, and M. Imada, *Phys. Rev. X* **13**, 041036 (2023).
- [13] O. Rösch and O. Gunnarsson, *Phys. Rev. Lett.* **92**, 146403 (2004).
- [14] A. S. Mishchenko and N. Nagaosa, *Phys. Rev. Lett.* **93**, 036402 (2004).
- [15] O. Rösch and O. Gunnarsson, *Eur. Phys. J. B* **43**, 11–18 (2005).
- [16] I. A. Makarov, E. I. Shneyder, P. A. Kozlov, and S. G. Ovchinnikov, *Phys. Rev. B* **92**, 155143 (2015).
- [17] E. I. Shneyder, S. V. Nikolaev, M. V. Zotova, R. A. Kaldin, and S. G. Ovchinnikov, *Phys. Rev. B* **101**, 235114 (2020).
- [18] J.-J. Zhou, J. Park, I. Timrov, A. Floris, M. Cococcioni, N. Marzari, and M. Bernardi, *Phys. Rev. Lett.* **127**, 126404 (2021).
- [19] Z. Li, M. Wu, Y.-H. Chan, and S. G. Louie, *Phys. Rev. Lett.* **126**, 146401 (2021).
- [20] D. J. Abramovitch, J.-J. Zhou, J. Mravlje, A. Georges, and M. Bernardi, *Phys. Rev. Mater.* **7**, 093801 (2023).
- [21] S. Y. Savrasov and O. K. Andersen, *Phys. Rev. Lett.* **77**, 4430–4433 (1996).
- [22] R. Heid, K.-P. Bohnen, R. Zeyher, and D. Manske, *Phys. Rev. Lett.* **100**, 137001 (2008).
- [23] F. Giustino, M. L. Cohen, and S. G. Louie, *Nature* **452**, 975–978 (2008).
- [24] K. Pokharel, C. Lane, J. W. Furness, R. Zhang, J. Ning, B. Barbiellini, R. S. Markiewicz, Y. Zhang, A. Bansil, and J. Sun, *npj Comput. Mater.* **8**, 31 (2022).
- [25] J. W. Furness, Y. Zhang, C. Lane, I. G. Buda, B. Barbiellini, R. S. Markiewicz, A. Bansil, and J. Sun, *Commun. Phys.* **1**, 11 (2018).
- [26] C. Lane, J. W. Furness, I. G. Buda, Y. Zhang, R. S. Markiewicz, B. Barbiellini, J. Sun, and A. Bansil, *Phys. Rev. B* **98**, 125140 (2018).
- [27] J. Ning, C. Lane, Y. Zhang, M. Matzelle, B. Singh, B. Barbiellini, R. S. Markiewicz, A. Bansil, and J. Sun, *Phys. Rev. B* **107**, 045126 (2023).
- [28] P. Wei and Z. Qing Qi, *Phys. Rev. B* **49**, 12159–12164 (1994).

- [29] V. I. Anisimov, M. A. Korotin, J. Zaanen, and O. K. Andersen, *Phys. Rev. Lett.* **68**, 345–348 (1992).
- [30] T. C. Sterling and D. Reznik, *Phys. Rev. B* **104**, 134311 (2021).
- [31] P. Zhang, S. G. Louie, and M. L. Cohen, *Phys. Rev. Lett.* **98**, 067005 (2007).
- [32] L. Monacelli, R. Bianco, M. Cherubini, M. Calandra, I. Errea, and F. Mauri, *J. Phys. Condens. Matter* **33**, 363001 (2021).
- [33] J.-J. Zhou and M. Bernardi, *Phys. Rev. B* **94**, 201201 (2016).
- [34] J.-J. Zhou and M. Bernardi, *Phys. Rev. Res.* **1**, 033138 (2019).
- [35] M. Reehuis, C. Ulrich, K. Prokeš, A. Gozar, G. Blumberg, S. Komiya, Y. Ando, P. Pattison, and B. Keimer, *Phys. Rev. B* **73**, 144513 (2006).
- [36] J. M. Tranquada, “Neutron Scattering Studies of Antiferromagnetic Correlations in Cuprates”, in *Handbook of High-Temperature Superconductivity* (Springer-Verlag New York, 2007), pp. 257–298.
- [37] Y. Yamaguchi, H. Yamauchi, M. Ohashi, H. Yamamoto, N. Shimoda, M. Kikuchi, and Y. Syono, *Jpn. J. Appl. Phys.* **26**, L447–L448 (1987).
- [38] P. Giannozzi, S. Baroni, N. Bonini, M. Calandra, R. Car, C. Cavazzoni, D. Ceresoli, G. L. Chiarotti, M. Cococcioni, I. Dabo, A. Dal Corso, S. de Gironcoli, S. Fabris, G. Fratesi, R. Gebauer, U. Gerstmann, C. Gougoussis, A. Kokalj, M. Lazzeri, L. Martin-Samos, N. Marzari, F. Mauri, R. Mazzarello, S. Paolini, A. Pasquarello, L. Paulatto, C. Sbraccia, S. Scandolo, G. Sclauzero, A. P. Seitsonen, A. Smogunov, P. Umari, and R. M. Wentzcovitch, *J. Phys. Condens. Matter* **21**, 395502 (2009).
- [39] P. Giannozzi, O. Andreussi, T. Brumme, O. Bunau, M. Buongiorno Nardelli, M. Calandra, R. Car, C. Cavazzoni, D. Ceresoli, M. Cococcioni, N. Colonna, I. Carnimeo, A. Dal Corso, S. de Gironcoli, P. Delugas, R. A. DiStasio, A. Ferretti, A. Floris, G. Fratesi, G. Fugallo, R. Gebauer, U. Gerstmann, F. Giustino, T. Gorni, J. Jia, M. Kawamura, H.-Y. Ko, A. Kokalj, E. Küçükbenli, M. Lazzeri, M. Marsili, N. Marzari, F. Mauri, N. L. Nguyen, H.-V. Nguyen, A. Otero-de-la-Roza, L. Paulatto, S. Poncé, D. Rocca, R. Sabatini, B. Santra, M. Schlipf, A. P. Seitsonen, A. Smogunov, I. Timrov, T. Thonhauser, P. Umari, N. Vast, X. Wu, and S. Baroni, *J. Phys. Condens. Matter* **29**, 465901 (2017).
- [40] I. Timrov, N. Marzari, and M. Cococcioni, *Phys. Rev. B* **103**, 045141 (2021).
- [41] I. Timrov, N. Marzari, and M. Cococcioni, *Comput. Phys. Commun.* **279**, 108455 (2022).
- [42] I. Timrov, N. Marzari, and M. Cococcioni, *Phys. Rev. B* **98**, 085127 (2018).
- [43] B. Keimer, A. Aharony, A. Auerbach, R. J. Birgeneau, A. Cassanho, Y. Endoh, R. W. Erwin, M. A. Kastner, and G. Shirane, *Phys. Rev. B* **45**, 7430–7435 (1992).

- [44] A. Floris, I. Timrov, B. Himmetoglu, N. Marzari, S. de Gironcoli, and M. Cococcioni, *Phys. Rev. B* **101**, 064305 (2020).
- [45] J.-J. Zhou, J. Park, I.-T. Lu, I. Maliyov, X. Tong, and M. Bernardi, *Comput. Phys. Commun.* **264**, 107970 (2021).
- [46] A. A. Mostofi, J. R. Yates, Y.-S. Lee, I. Souza, D. Vanderbilt, and N. Marzari, *Comput. Phys. Commun.* **178**, 685–699 (2008).
- [47] M. Bernardi, *Eur. Phys. J. B* **89**, 239 (2016).
- [48] B. K. Chang, J.-J. Zhou, N.-E. Lee, and M. Bernardi, *npj Comput. Mater.* **8**, 63 (2022).
- [49] B. O. Wells, Z. -X. Shen, A. Matsuura, D. M. King, M. A. Kastner, M. Greven, and R. J. Birgeneau, *Phys. Rev. Lett.* **74**, 964–967 (1995).
- [50] J. A. Sobota, Y. He, and Z.-X. Shen, *Rev. Mod. Phys.* **93**, 025006 (2021).
- [51] T. Thio, R. J. Birgeneau, A. Cassanho, and M. A. Kastner, *Phys. Rev. B* **42**, 10800–10803 (1990).
- [52] J. M. Ginder, M. G. Roe, Y. Song, R. P. McCall, J. R. Gaines, E. Ehrenfreund, and A. J. Epstein, *Phys. Rev. B* **37**, 7506–7509 (1988).
- [53] T. A. Kaplan and S. D. Mahanti, *J. Appl. Phys* **69**, 5382–5384 (1991).
- [54] S. R. Park, T. Fukuda, A. Hamann, D. Lamago, L. Pintschovius, M. Fujita, K. Yamada, and D. Reznik, *Phys. Rev. B* **89**, 020506 (2014).
- [55] F. Stercel, T. Egami, H. A. Mook, M. Yethiraj, J.-H. Chung, M. Arai, C. Frost, and F. Dogan, *Phys. Rev. B* **77**, 014502 (2008).
- [56] L. Pintschovius, W. Reichardt, M. Kläser, T. Wolf, and H. v. Löhneysen, *Phys. Rev. Lett.* **89**, 037001 (2002).
- [57] H. Fröhlich, *Adv. Phys.* **3**, 325–361 (1954).
- [58] J. J. Zhou, O. Hellman, and M. Bernardi, *Phys. Rev. Lett.* **121**, 226603 (2018).
- [59] A. Lanzara, P. V. Bogdanov, X. J. Zhou, S. A. Kellar, D. L. Feng, E. D. Lu, T. Yoshida, H. Eisaki, A. Fujimori, K. Kishio, J.-I. Shimoyama, T. Noda, S. Uchida, Z. Hussain, and Z.-X. Shen, *Nature* **412**, 510–514 (2001).
- [60] P. D. Johnson, T. Valla, A. V. Fedorov, Z. Yusof, B. O. Wells, Q. Li, A. R. Moodenbaugh, G. D. Gu, N. Koshizuka, C. Kendziora, S. Jian, and D. G. Hinks, *Phys. Rev. Lett.* **87**, 177007 (2001).
- [61] X. J. Zhou, T. Yoshida, A. Lanzara, P. V. Bogdanov, S. A. Kellar, K. M. Shen, W. L. Yang, F. Ronning, T. Sasagawa, T. Kakeshita, T. Noda, H. Eisaki, S. Uchida, C. T. Lin, F. Zhou, J. W. Xiong, W. X. Ti, Z. X. Zhao, A. Fujimori, Z. Hussain, and Z.-X. Shen, *Nature* **423**, 398–398 (2003).
- [62] R. J. McQueeney, Y. Petrov, T. Egami, M. Yethiraj, G. Shirane, and Y. Endoh, *Phys. Rev. Lett.* **82**, 628–631 (1999).

- [63] A. Bianconi, N. L. Saini, A. Lanzara, M. Missori, T. Rossetti, H. Oyanagi, H. Yamaguchi, K. Oka, and T. Ito, *Phys. Rev. Lett.* **76**, 3412–3415 (1996).
- [64] A. Bohrdt, E. Demler, F. Pollmann, M. Knap, and F. Grusdt, *Phys. Rev. B* **102**, 035139 (2020).
- [65] D. Betto, R. Fumagalli, L. Martinelli, M. Rossi, R. Piombo, K. Yoshimi, D. Di Castro, E. Di Gennaro, A. Sambri, D. Bonn, G. A. Sawatzky, L. Braicovich, N. B. Brookes, J. Lorenzana, and G. Ghiringhelli, *Phys. Rev. B* **103**, L140409 (2021).
- [66] I. J. Hamad, L. O. Manuel, and A. A. Aligia, *Phys. Rev. B* **103**, 144510 (2021).
- [67] X. J. Zhou, J. Shi, T. Yoshida, T. Cuk, W. L. Yang, V. Brouet, J. Nakamura, N. Mannella, S. Komiyama, Y. Ando, F. Zhou, W. X. Ti, J. W. Xiong, Z. X. Zhao, T. Sasagawa, T. Kakeshita, H. Eisaki, S. Uchida, A. Fujimori, Z. Zhang, E. W. Plummer, R. B. Laughlin, Z. Hussain, and Z.-X. Shen, *Phys. Rev. Lett.* **95**, 117001 (2005).
- [68] S.-W. Cheong, J. Thompson, and Z. Fisk, *Physica C Supercond.* **158**, 109–126 (1989).
- [69] J. P. Perdew, A. Ruzsinszky, G. I. Csonka, O. A. Vydrov, G. E. Scuseria, L. A. Constantin, X. Zhou, and K. Burke, *Phys. Rev. Lett.* **100**, 136406 (2008).
- [70] D. Vanderbilt, *Phys. Rev. B* **41**, 7892–7895 (1990).
- [71] K. F. Garrity, J. W. Bennett, K. M. Rabe, and D. Vanderbilt, *Comput. Mater. Sci.* **81**, 446–452 (2014).
- [72] M. Hücker, M. v. Zimmermann, G. D. Gu, Z. J. Xu, J. S. Wen, G. Xu, H. J. Kang, A. Zheludev, and J. M. Tranquada, *Phys. Rev. B* **83**, 104506 (2011).
- [73] R. J. Birgeneau, C. Y. Chen, D. R. Gabbe, H. P. Jenssen, M. A. Kastner, C. J. Peters, P. J. Picone, T. Thio, T. R. Thurston, H. L. Tuller, J. D. Axe, P. Böni, and G. Shirane, *Phys. Rev. Lett.* **59**, 1329–1332 (1987).
- [74] P. Böni, J. D. Axe, G. Shirane, R. J. Birgeneau, D. R. Gabbe, H. P. Jenssen, M. A. Kastner, C. J. Peters, P. J. Picone, and T. R. Thurston, *Phys. Rev. B* **38**, 185–194 (1988).
- [75] A. Sapkota, T. C. Sterling, P. M. Lozano, Y. Li, H. Cao, V. O. Garlea, D. Reznik, Q. Li, I. A. Zaliznyak, G. D. Gu, and J. M. Tranquada, *Phys. Rev. B* **104**, 014304 (2021).

SUMMARY AND FUTURE DIRECTIONS

In summary, this thesis shows detailed quantitative studies of electron-phonon (e -ph) interactions in organic crystals and cuprates, pushing the boundaries of first-principles calculations and advancing the knowledge of charge transport, polarons, and high-temperature superconductivity, thus offering new insights toward high-performance and novel electronic technologies.

Organic crystals

In Chapter 2, we carry out in-depth studies of the high-mobility charge transport in organic crystals. We conduct Boltzmann transport equation (BTE) calculations for the bandlike charge carrier mobilities in benzene, anthracene, tetracene, pentacene, and biphenyl, with pentacene (72 atoms per unit cell) setting the record of the largest system ever analyzed using first-principles e -ph calculations. The accuracy of our calculations are verified by comprehensive comparisons with experimental results. Our findings show that the bandlike mobilities are regulated predominantly by the e -ph scattering from phonons with frequencies below 150 cm^{-1} . This frequency range constitutes less than 5% of the entire phonon spectrum frequency range, which exceeds $3,000\text{ cm}^{-1}$. These low-frequency phonons, predominantly intermolecular in nature, are distinctively sensitive to strains. Our results highlight the potential of phonon mode-targeting engineering methods for enhancing the performance of high-mobility organic electronics. Additionally, our work marks a significant step towards efficient and ultra-large-scale first-principles e -ph calculations.

In Chapter 3, we study polaronic charge transport in organic crystals, with a focus on examining electron mobilities in naphthalene. We show that the mobility is polaronic, as evidenced by the breakdown of the BTE and the presence of satellites and a long tail in electron spectral functions. These spectral features, captured by cumulant calculations, are induced by strong e -ph coupling of intramolecular phonon modes, which involve hydrogen atoms vibrating both within and out of the molecular planes. Accordingly, we employ the Kubo formula to compute charge transport. Our computed in-plane electron mobilities show very good agreement with experimental measurements, and exhibit highly accurate power-law temperature dependencies. Furthermore, we demonstrate that our cumulant-Kubo (CK)

formalism achieves similar prediction accuracy to the BTE for the bandlike transport regime, as illustrated using the hole mobilities in naphthalene. Our work presents a generally applicable approach for accurately predicting polaron transport in molecular crystals and is a first step towards *ab initio* identification of charge transport regimes in organic semiconductors.

Our work on organic crystals opens several promising research directions. The first involves developing first-principles methods to model charge transport in the hopping regime, which remains unexplored in this thesis. This regime is characterized by thermally activated transport of self-trapped (small) polarons. Advancements in calculating small polaron energies and wave functions, as reported in recent studies [1–3], can facilitate this exploration. The second direction is to expand current calculations to additional organic crystals. For instance, some technologically important crystals like TIPS-pentacene (100 atoms per unit cell) [4] were previously challenging to compute due to their large size, but are now potentially within reach. Moreover, investigating molecules with diverse functional groups and stacking patterns will further our understanding of the relationship between crystal structure and charge transport properties, expediting the design of novel engineering approaches. The third path is related to data-driven studies, which have received increasing interest in both inorganic and organic materials research [5, 6]. Given the demonstrated efficiency and accuracy of first-principles *e*-ph and transport calculations in Chapters 2 and 3, we can pursue high-throughput investigations and create datasets to train machine learning models, enabling extensive discovery of organic crystals with desirable properties. In summary, the research directions proposed here will significantly advance materials science and chemical physics, contributing to the ultimate goal of accelerating the discovery of new materials and the realization of next-generation electronic technologies.

Cuprate superconductors

In Chapter 4, we present the first quantitative calculations of *e*-ph interactions in a parent-compound cuprate, using the prototypical case of La_2CuO_4 (LCO) as an example. We find strong Fröhlich interactions between holes and phonons associated with oxygen vibrations, and show that the strong coupling leads to significant broadening in the hole spectral functions. Our findings provide explanations for several phenomena observed in photoemission experiments. These include the dispersion kink in doped cuprates and the polaronic spectral broadening and peak shift in the parent phases. Our calculations also capture a feature in experimental self-energy

that cannot be described by existing models. We show that this feature is due primarily to O vibrations out of the Cu-O bond axis. Since conventional models are typically constructed upon the Cu-O bonds using Cu $d_{x^2-y^2}$ and O $p_{x,y}$ orbitals, our results underscore the importance of incorporating additional orbitals into effective models for a more comprehensive description of experimental findings. Taken together, this work presents compelling evidence that the universal strong e -ph coupling found experimentally in lanthanum cuprates is an intrinsic feature of the parent compound, and provides a broadly applicable computational workflow for accurate studies of e -ph interactions in a wide range of strongly-correlated transition metal oxides (TMOs).

Our study points to multiple important research directions. The first is the orbital-resolved analysis of e -ph coupling. Since our work has shown that atomic orbitals not addressed in existing models (e.g. Cu d_{xy} , d_{xz} , d_{yz} , d_{z^2} and O p_z) can significantly contribute to phenomena observed in experiments, quantifying and comparing e -ph coupling strengths of individual atomic orbitals will provide critical insights into the limits of existing models and how to improve them. This can be achieved by investigating the orbital projections of the electron Bloch states in our calculations. The second research path is to extend current calculations to other important cuprate high-temperature superconductors, such as $\text{YBa}_2\text{Cu}_3\text{O}_7$ (YBCO) [7] and $\text{Bi}_2\text{Sr}_2\text{CaCu}_2\text{O}_8$ (Bi-2212) [8, 9]. This will allow a deeper understanding of the universal properties of cuprate materials, which helps identifying common patterns across materials for high-temperature superconductivity. The third direction is to apply our computational workflow to other families of TMOs, including manganese oxides (manganites), nickel oxides (nickelates), vanadium oxides (vanadates), and titanium oxides (titanates). Understanding e -ph interactions in these strongly-correlated materials will greatly facilitate the use of complex correlated oxides for energy and computing applications [10, 11]. Moving forward, these extensions of our work in Chapter 4 will continue to advance our fundamental understanding of correlated materials and their potential for novel technologies.

References

- [1] N.-E. Lee, H.-Y. Chen, J.-J. Zhou, and M. Bernardi, *Phys. Rev. Mater.* **5**, 063805 (2021).
- [2] Y. Luo, B. K. Chang, and M. Bernardi, *Phys. Rev. B* **105**, 155132 (2022).
- [3] W. H. Sio, C. Verdi, S. Ponc e, and F. Giustino, *Phys. Rev. Lett.* **122**, 246403 (2019).

- [4] G. Giri, S. Park, M. Vosgueritchian, M. M. Shulaker, and Z. Bao, *Adv. Mater.* **26**, 487–493 (2014).
- [5] A. Merchant, S. Batzner, S. S. Schoenholz, M. Aykol, G. Cheon, and E. D. Cubuk, *Nature* **624**, 80–85 (2023).
- [6] C. Kunkel, J. T. Margraf, K. Chen, H. Oberhofer, and K. Reuter, *Nat. Commun.* **12**, 2422 (2021).
- [7] M. K. Wu, J. R. Ashburn, C. J. Torng, P. H. Hor, R. L. Meng, L. Gao, Z. J. Huang, Y. Q. Wang, and C. W. Chu, *Phys. Rev. Lett.* **58**, 908–910 (1987).
- [8] H. Maeda, Y. Tanaka, M. Fukutomi, and T. Asano, *Jpn. J. Appl. Phys.* **27**, L209 (1988).
- [9] Y. Yu, L. Ma, P. Cai, R. Zhong, C. Ye, J. Shen, G. D. Gu, X. H. Chen, and Y. Zhang, *Nature* **575**, 156–163 (2019).
- [10] J. Ngai, F. Walker, and C. Ahn, *Annu. Rev. Mater. Sci.* **44**, 1–17 (2014).
- [11] A. Sawa, *Mater. Today* **11**, 28–36 (2008).